Title	Effects of Weak Rock Zones and Stone Wall on Mining-induced Deformation of Rock Slope at Mt. Buko
Author(s)	張, 誠; Zhang, Cheng
Degree Grantor	北海道大学
Degree Name	博士(工学)
Dissertation Number	甲第16357号
Issue Date	2025-03-25
DOI	https://doi.org/10.14943/doctoral.k16357
Doc URL	https://hdl.handle.net/2115/95094
Type	doctoral thesis
File Information	Cheng_Zhang.pdf

Effects of Weak Rock Zones and Stone Wall on Mining-induced Deformation of Rock Slope at Mt. Buko

Dissertation for the Degree of Doctor of Engineering

Cheng Zhang

Division of Sustainable Resources Engineering

Graduate School of Engineering

Hokkaido University, Japan

January 2025

Effects of Weak Rock Zones and Stone Wall on Mining-induced Deformation of Rock Slope at Mt. Buko
(武甲山の残壁の掘削変位に与える弱層の影響と盛石の効果)

By

Cheng Zhang

A dissertation submitted in partial fulfillment of the requirements for the Degree of Doctor of Engineering

Division of Sustainable Resources Engineering

Graduate School of Engineering

Hokkaido University

Japan

January 2025

Declaration

I, Cheng Zhang, declare that this dissertation titled " Effects of Weak Rock Zones and Stone Wall on Mining-induced Deformation of Rock Slope at Mt. Buko" is an original report of my study and was carried out entirely under the supervision of Professor Jun-ichi Kodama. It was written by me and references have been duly provided on all supporting literature and resources. I also declare that this dissertation has not been submitted previously, either in whole or part, for application of any degree.

Acknowledgements

As I look back, this marks my sixth year in Japan. Time flies, and in the blink of an eye, half of my youth has quietly passed. Amid this silent passage of time, I now prepare to bring my student years to a close. To me, the acknowledgments section of my doctoral dissertation, though considered the most effortless part, feels more like a farewell letter to my youth.

During these six years of studying in Japan, I have grown from a university graduate full of aspirations for the future into a soon-to-be member of society. Like a character in a video game, I have continuously leveled up, battled challenges, and collected "equipment" and experience. When faced with mistakes and failures, I have wielded my "weapons" time and again, bravely confronting challenges I had never encountered before. Some say that a doctoral degree represents an accumulation of knowledge, but for me, it is a refinement of logical thinking. Some say that student life is lighthearted and enjoyable, yet for me, this journey has been a rich accumulation of life experiences. These six years—filled with joy and tears, reluctance and happiness, meetings and farewells—have come together like the snowy seasons of Sapporo: heavy and profound, yet quietly melting away with each spring day.

First and foremost, I would like to express my heartfelt gratitude to my parents. No matter where or when, you have always stood firmly by my side, dedicating your all to me. Your unwavering support is the strongest foundation of my life.

Next, I must extend my deepest thanks to my supervisor, Professor Junichi Kodama. To have a mentor is a fortune, but to have a friend in a mentor is a greater blessing. Over the years, you have selflessly imparted your knowledge, time, and connections to me. Even more precious is the fatherly care you have shown, teaching me not only the depth of academic pursuits but also the philosophy and wisdom of life itself.

Additionally, I want to express my gratitude to the Rock Mechanics Laboratory and the GDI Laboratory at Hokkaido University for supporting my research and life. I am particularly thankful to Professors Sainoki, Fujii, and Fukuda for their guidance throughout my academic journey. I am also deeply grateful to the friends who accompanied me during my time at Hokkaido University. You have been like desserts in daily life and festive lights on special occasions, adding warmth and color to my days in a foreign land.

Lastly, I want to thank my girlfriend. They say that accompanying a boy through his growth

demands staking one's youth. In these years, you have been like the warm sun of spring, the gentle breeze of summer, the crimson leaves of autumn, and the radiant sunlight of winter, illuminating the solitude deep within my heart. Life burns brighter because of you. "As in life and death we are destined to be together; holding your hand, I wish to grow old with you." May this love and companionship become our vow for a lifetime together.

To everyone who has accompanied me on this journey, I offer my heartfelt thanks. May we continue to walk the road ahead together.

Abstract

Unexplained rock slope deformation has been observed at the limestone quarry of Mt. Buko in Saitama Prefecture, Japan, since the automated polar system (APS) was introduced in the quarry. The rock slope in the western part shows significant and continuous deformation although little deformation has been observed in the eastern part. To restrain this continuous deformation, the construction of a stone wall was initiated on the west side. Ensuring the safety of the rock slope requires not only understanding the deformation mechanism but also evaluating the stone wall's effectiveness, which remains an urgent issue.

Vertical and inclined weak rock zones were found through the quarry. The vertical one is developed in limestone deposit, and the inclined one is distributed along the geological boundary between bedrock and the cover rock, which is unexcavated limestone layer for the protection of the base rock against weathering. Understanding the impacts of these weak rock zones is expected to be key to clarifying the mechanism of rock slope deformation, as the connectivity of the two weak rock zones on the west side differs from that on the east side.

Based on the aforementioned background, this study analyzed the deformation characteristics of the rock slope at Mt. Buko, focusing on the relationships among geological structures, excavation states, and field measurement data. Numerical models incorporating the quarry's geological features were developed to estimate mining-induced deformation of the rock slope, aiming to better understand deformation mechanisms. Both the constructed and planning stone walls at the quarry were also numerically modeled to evaluate their mechanical impacts and estimate their optimal dimensions. Furthermore, the effects of the dip angle and connectivity of the weak rock zones were investigated in detail for providing a generalized understanding of their influence. The effects of the stone wall height, width and construction timing were also examined. The specific contents of each chapter are as follows:

Chapter 1 systematically describes the background, objectives, novelty, and importance of this study, along with a literature review of related research.

Chapter 2 outlines the deformation issues, geological structures, mining history, and monitoring systems at Mt. Buko. The relationships between the characteristics of the rock slope deformation, the connectivity of the weak rock zones, and excavation progression were analyzed. The results show that rock slope displacement on the west side accelerates as the vertical weak

rock zone (VZ) appears on the rock slope surface with the lowering of the excavation face. This finding emphasizes the importance of accurately modeling geological structures and excavation progress in analyzing deformation mechanisms.

Chapter 3 presents numerical simulations of mining-induced deformation of the rock slope at Mt. Buko, with results that quantitatively align with field measurements. The models indicate the followings. A reduction in normal stress due to excavation leads to progressive failure along the geological boundary. Then, sliding force induced by the boundary failure applies to the VZ behind it. As the VZ appears on the rock slope surface, resistance against the sliding force decreases. Sliding movement stops as the excavation progresses, eventually reaching equilibrium. Thus, the observed continuous deformation is effectively explained by the proposed mechanism.

Chapter 4 evaluates the effectiveness of stone walls at Mt. Buko by numerical simulation, highlighting its role in restraining slip deformation. The results reveal that the weight of the stone wall significantly influences the restraint of slip deformation. The mechanism of stone wall for restraining slip deformation is considered as not only increasing the bending stiffness of the area in front of the VZ, but also provides the press effect by self-weight, increasing the height of the stone wall helps to further stabilize the slope. Additionally, optimal dimensions for the stone wall were recommended for future construction.

Chapter 5 numerically analyzes several effects of weak rock zone and stone walls by simplifying the geometry of rock slope and weak rock zones. It is found that no slip displacement is seen in models with single weak rock zone regardless of its dip direction. Slip displacement of a cover rock only occurs when two weak rock zones are connected. The slip displacement tends to decrease with increase of the thickness of cover rock. It is also found that earlier construction of a stone wall, up to higher elevations, provides the maximum deformation control. However, a critical value was found in stone wall height. No sliding can be seen at the critical height or more. These findings provide valuable insights for addressing similar issues in open-pit mines.

Chapter 6 summarizes the main conclusions and recommendations of this study. A more in-depth analysis of the stone walls is necessary, as the effect of contact stiffness between the stone wall and the slope remain unclear. The lack of consideration for pore water pressure effects and three-dimensional factors are key limitations that could significantly impact slope stability.

Contents

List of Figures

List of Tables

1. Introduction

1.1 Background and objectives

Rock slope stability assessment is increasingly critical in rock engineering, especially in large-scale open-pit mining (Read and Stacey, 2009). As mining progresses each year, slope height usually increases, forming large rock slopes that may remain post-mining. Such slopes pose unavoidable landslide and have instability risks, endangering workers, damaging property, disrupting operations, and incurring restoration costs (Rose et al., 2007; Assefa et al., 2017), which can lead to economic losses. In recent years, severe instability observed in the rock slopes at Las Cruces, Spain (López et al., 2020) and Alxa Left Banner, China (An et al., 2023) caused extensive equipment damage and causing several casualties among mine workers. Hence, analysis of slope stability and design of countermeasures are essential for safe, efficient mining while minimizing landslide risks.

Monitoring of rock slope deformation has been the main method for stability assessment of rock slopes in open-pit mines (Amagu et al., 2022; Kodama et al., 2009) because the instability of rock slopes is often preceded by continuous deformations. For example, the cumulative displacements of the rock slopes at Las Cruces, and Alxa Left Banner mentipned above reached 7 cm and 14 cm before final failure, respectively.

Continuous deformation has been observed at Mt. Buko which is an open-cut limestone quarry, in Saitama Prefecture, Japan. The rock slope has experienced extensive deformation since monitoring of the surface displacement commenced in 1998 (Zhang et al., 2024). Interestingly, the rock slope deformation strongly depends on the section, even though excavation has almost uniformly progressed. The west section of the rock slope has shown substantial deformation as mining continued, while little deformation has been observed on the east section. Over the past 25 years, the surface displacement exceeding 4 cm were recorded in 2007 (Yamatomi et al., 2016), totaling around 35 cm. For restraining the significant continuous deformation on the west side, construction of a stone wall on the west section was commenced in 2013 (Yamaguchi et al., 2016).

Unique geological structure characterized by vertical and inclined weak rock zones is considered to cause the aforementioned displacement. Rock slope displacement on the west side accelerates as the vertical weak rock zone (VZ) appears on the rock slope surface with the lowering of the excavation face. Understanding the impacts of these weak rock zones is expected to be key to clarifying the mechanism of rock slope deformation, as the connectivity of the two weak rock zones on the west side differs from that on the east side.

Given the above background, objectives of this study are set as the following.

The first objective is to find the relationship among the mining-induced deformation, the mining state, and the weak rock zones by analyzing the measurement results. As previously described, the observed deformation is likely linked to the distribution of weak rock zones and mining activities.

The second one is to clarify the mechanisms behind the long-term deformation observed at Mt. Buko, particularly the effects of weak rock zones within the slope, and to identify the primary causes of deformation due to the existing knowledge is insufficient to fully explain the deformation.

The third one is to evaluate the effectiveness and optimal design of the stone wall countermeasure implemented at Mt. Buko. This countermeasure was introduced to restrain slip deformation and enhance slope stability. However, its effectiveness and the mechanism by which it controls slip deformation remain unclear.

The final one is to generalize and extend the knowledge about the effects of weak rock zone and stone wall obtained from the model of Mt. Buko by simplifying the geometry of a rock slope and weak rock zones. We investigate more thoroughly the effects of the weak rock zones on mining-induced deformation of a rock slope varying the dip direction, connectivity and thickness of a cover rock. Effects of stonewall are also investigated by changing the width, height and construction timing to get a general recommendation.

1.2 Literature review

Many researchers have focused on analysis of the deformation and stability of rock slope ((Hoek and Bray, 1981; Goodman, 1989; Kaneko et al., 1997; Willie and Mah, 2004; Kodama et al., 2009). However, assessment of rock slope deformation and stability still poses a major challenge to rock engineering projects worldwide, especially of large-scale open-pit mines as it requires to consider the effects of mining, geological structure, lithology, and geotechnical properties of the rock mass comprehensively. In this study, as described in Section 1.1, the primary objective is to clarify the deformation mechanisms of rock slope with weak rock zones and evaluate the effectiveness of stone wall countermeasure in controlling deformation of the rock slope at Mt. Buko. To establish the context of this research, this section reviews the stability assessment and cause of deformation of rock slope, effects of excavation and geological structure, and countermeasures on rock slopes. Previous studies on monitoring of the rock slope behaviors at Mt. Buko are also reviewed.

1.2.1 Stability assessment of rock slope

In open-pit mines, excavation can often cause both elastic and inelastic deformation in cut rock slopes (Kaneko et al., 1997; Kodama et al., 2009). For this reason, separating measured deformation into elastic and inelastic components is essential for accurate stability assessments. By calculating the elastic deformation of rock slopes, inelastic deformation can be inferred by comparing the measured data with the analyzed elastic deformation.

Given these considerations, field measurements and continuous monitoring of rock slope deformation are regarded as crucial methods for assessing slope stability in most open-pit mines (Rose and Hungr, 2007), predicting potential failures, and designing effective countermeasures. So far, the research of slope stability has been progressed more than 300 years, and the techniques have been developed which include a range of simple evaluation, planar failure, limit state criteria, limit equilibrium analysis (Bishop, 1955; Yamaguchi and Shimotani, 1986; Duncan et al., 1996; Ataei and Bodaghabadi, 2008; Stead et al., 2006), numerical methods (Jing and Hudson, 2002; Jing, 2003; Eberhardt et al., 2004; Kodama et al., 2009; Barla, 2016), hybrid and high-order approaches which are implemented in two-dimensional and three-dimensional space (Mohammad et al., 2021).

In recent years, with the advancement of computer computing power and the iterative update of graphics cards, computer-based numerical simulation methods are increasingly used in the analysis of slope problems. The engineers found that for certain types of complex geotechnical problems, finite element method (FEM) offer real remuneration over limit equilibrium methods (Griffiths and Lane., 1999; Kainthola et al., 2011). Common deformation problems can be calculated by unitizing the slope and analyzing the specific deformation values caused by excavation, rainfall and other factors (Amagu et al., 2021). In addition, discrete element method (DEM), which allows the particles to move with each other, to separate, to rotate, to consider the forces between the particles, is also widely used today (Cundall P.A. et al., 1979). This method has performed very well in solving rock fall or collapse problems (Wang and Fulvio., 2010; Shen et al., 2019).

In Japan, various tools such as the Automated Polar System (APS) (Study Committee on Slope Stability and Environmental Preservation in Chichibu Area, 1996), tiltmeters (Sugawara, 2000), Global Positioning System (GPS) (Shimizu et al., 1997; Sugawara, 2000; Matsuda et al., 2003), and extensometers (Noguchi and Okada, 1999; Nakamura et al., 2003) have been applied to measure rock slope displacement. Obara et al. (2000) and Kodama et al. (2009) recommend integrating field measurements with elastic analysis for rock slope stability assessment, as inelastic deformation can be derived from comparing measured results with estimated elastic deformation once elastic deformation is calculated.

Based on these studies, considering that the monitoring data at Mt. Buko spans less than 25 years and that previous numerical simulations have not successfully captured deformation behavior, this study investigates the long-term deformation of rock slopes at Mt. Buko using field displacement measurements and numerical analysis.

1.2.2 Causes of deformation and failure of rock slope

The deformation and failure of rock slopes are governed by a complex triggering factors such as geological, hydrological, and anthropogenic factors, each contributing to instability through distinct mechanisms (Read and Stacey, 2009; Gao et al., 2017; Kolapo et al., 2022).

Geological structures, such as faults, fractures, and weak rock zones, introduce inherent discontinuities within the rock mass, significantly lowering its cohesive strength and predisposing it to deformation under varying stress conditions (Azarfar et al., 2019; Kaczmarek et al., 2019; Li et al., 2019; Wang et al., 2019; Lemaire et al., 2020; Vick et al., 2020; Xie et al., 2020). Zhang et al. (2024) analyzed a rock slope failure caused by brittle rock behavior and pre-existing discontinuities, which occurred in multiple phases with a total volume of 30,000 m^3, emphasizing the influence of inherent geological features on instability. Zhu et al. (2021) investigated a slope failure triggered by excavation activities and revealed that faults and fractures were major contributors to the instability, further exacerbated by human intervention.

Hydrological factors, such as rainfall infiltration and fluctuations in groundwater levels, play a significant role in slope instability by increasing pore water pressure and reducing shear strength along discontinuities, which can ultimately destabilize slopes (Fujiita, 1997; Sugiyama et al., 1995; Ishikawa et al., 2015; Sharifzadeh and Javadi, 2017; Ayalew et al., 2004; Cai and Ugai, 2004). Rainfall-induced slope failures are closely linked to groundwater table variations and elevated pore water pressure, which reduce the shear strength of the rock mass and can trigger landslides (Yeh et al., 2015; Sharifzadeh et al., 2002). Cai and Ugai (2004) specifically noted that rainfall infiltration raises groundwater levels and increases pore water pressure, further weakening the rock mass and significantly contributing to the occurrence of landslides and slope failures.

Anthropogenic activities, particularly excavation and blasting in mining operations, impose additional mechanical disturbances, redistributing stresses and steepening slopes, thus accelerating progressive instability (He et al., 2008; Kodama et al., 2013, Kaneko et al., 1996, Obara et al., 2000). Hustrulid et al. (2000) argued that instability of rock slopes is largely caused by mining activities such as rock drilling, blasting, and the use of heavy machines. Dou et al. (2022) found that the repeated failure of high cutting slopes was primarily caused by the combined effects of excavation-induced stress redistribution and rainfall infiltration, with numerical simulations highlighting the importance of managing these factors to enhance slope stability.

Thermal effects, such as freeze-thaw cycles, induce expansion and contraction in the rock matrix, intensifying internal stresses and exacerbating deformation over time (Luo et al., 2015; Kodama et al., 2019; Gang et al., 2024; Liu et al., 2024). Liu et al. (2024) reveals that freeze–thaw cycles, rainfall infiltration, and fracture propagation significantly impact the stability of frozen rock slopes by dynamically reducing the safety factor over time, highlighting the importance of a time-varying evaluation method based on thermo-hydro-mechanical (THM) coupling theory. Yang et al. (2024) concludes that freeze–thaw cycles and creep characteristics significantly degrade the mechanical properties of rock masses, reducing slope stability over time and underscoring the importance of incorporating these factors into slope design and stability assessments.

Seismic activity amplifies these risks by inducing dynamic loading and shaking, which can trigger rapid displacement and disrupt already weakened structures. Moreover, repeated seismic events can gradually erode the integrity of rock mass over time, particularly in faulted and fractured zones (Ohtsuka and Matsuo, 1995; Keefer, 2000; Bommer and Rodrı’guez, 2002; Dahal et al., 2006; Orense, 2012). During recent seismic events, several cases of slope failures induced by ground motion have been also reported (e.g., Ohtsuka and Matsuo, 1995; Lu et al., 2014, 2015). Particularly, Orense (2012) reported cases of slope failure induced by large-magnitude ground shaking and soil liquefaction of weathered tuffaceous sandstones, mostly at the boundaries between fill and cut slope sections during the 2011 Tohoku earthquake in Japan.

The above studies confirm that the interplay of geological, hydrological, and operational factors significantly increases the likelihood of slope deformation and failure, necessitating comprehensive analyses that integrate these dynamics for effective rock slope assessment and stabilization. At Mt. Buko, slope deformation is likely influenced by mining activities, geological conditions, rainfall, thermal and/or earthquake activity. However, the effects of thermal and seismic activity are considered minor, as no cyclic surface displacement changes have been observed during seasonal temperature variations, and the area has experienced no significant seismic events since 1998.

In contrast, as mentioned in background, the measurement results strongly show the relationship among the geological structures, excavation levels, and deformation behaviors. In addition, rainfall appears to have a stronger impact on slope stability due to its frequency in the mining region. Yamaguchi, Ozawa, and Kondo et al. (2018) identified a strong correlation between rainfall and slope surface displacement, though rainfall alone cannot fully explain the observed deformation process. Therefore, in this study, the assessment of slope stability is based on the consideration of the geological conditions, properties of rock mass, excavation-induced stress changes and mining progression in the quarry to well-understand behavior of the rock mass.

1.2.3 Effect of excavation on rock slope deformation

Typically, excavation leads to stress release in a rock slope, thereby causing elastic recovery displacements (Kaneko et al., 1996; Najib et al., 2015; Abdellah et al., 2022; Kodama et al., 2009; Kodama et al., 2012; Amagu et al., 2022; Amagu et al., 2024). The elastic recovery deformation caused by excavation comprises two modes, contraction or extension, depending on factors such as excavation patterns, stress states, and rock elastic properties. Kaneko et al., (1996) investigated the effects of initial stress on the deformation mode of an open-pit mine using two-dimensional (2D) elastic analysis. They reported that the rock slope contracted when the ratio of horizontal-to-vertical stress was small during excavation, yet the slope extended as the ratio increased. Najib et al., (2015) analyzed the mining-induced elastic deformation of mountain-type mines by varying the Poisson's ratio from 0.1 to 0.4; the Poisson's effect enhanced the horizontal extension of the rock slope, increased with Poisson's ratio. Abdellah et al., (2022) simulated the displacements caused by excavation for slope angles in the range of 20° to 70° using a 2D model. A hybrid approach combining deterministic numerical simulations and probabilistic methods was used to represent rock mass heterogeneity. The results indicated that the slope extended forward at slope angles of less than 35° and contracted backwards at more than 35°.

The aforementioned mining-induced elastic deformation is important for understanding the displacements observed in quarries. Kodama et al., (2009) investigated the causes of the long-term deformation of a rock slope at the Ikura limestone quarry in Japan using three-dimensional (3D) elastic analysis. They estimated Young's modulus and Poisson's ratio of the rock mass using back analysis and concluded that the long-term deformation over more than seven years can be interpreted as elastic deformation caused by excavation at the working face 400 m away from the rock slope. Amagu et al., (2021) investigated the deformation mechanism of the rock slope in the Higashi-Shikagoe limestone quarry based on 2D elastic simulations. They presumed that the displacement on the right-hand side of the rock slope primarily resulted from excavation induced elastic deformation and concluded that the rock slope was stable. The aforementioned studies demonstrate that the elastic analysis is sufficient to understand mining-induced deformations of homogeneous rock slopes in stable conditions. However, geological structures such as faults, shear zones, and weak rock layers have not been considered, and the knowledge accumulated in these studies is insufficient to explain discontinuous deformations, such as sliding movements.

Previous studies have primarily predicted the elastic deformation of homogeneous rock slopes, clarifying the effects of mining-induced elastic deformation in these cases. Some deformation issues in open-pit mines have been adequately explained by the impacts of excavation. However, weak rock zones and discontinuities, which are common in rock slopes, still require further investigation to understand their role in slope deformation. Additionally, it is essential to carefully explore whether these weak rock zones and discontinuities, in interaction with excavation activities, might contribute to increased deformation or even lead to slope failure.

1.2.4 Effect of geological structures on rock slope deformation

The deformation and failure of rock slopes are frequently controlled by the orientation and geometry of the discontinuities, including bedding planes, geological boundaries, joint sets, and faults. They can be classified into three types: plane, wedge, and toppling failures (Hocking et al., 1981; Yoon et al., 2002; Lee et al., 2011; Tang et al., 2017), and their failure mechanisms have been extensively researched (Glastonbury et al., 2000; MacLaughlin et al., 2001; Stead et al., 2015). Recently, several studies (Azarfar et al., 2019; Kaczmarek et al., 2019; Li et al., 2019; Wang et al., 2019; Lemaire et al., 2020; Vick et al., 2020; Xie et al., 2020) have reported that the failure patterns of rock slopes with two or more discontinuous geological structures, such as faults or weak layers, are complex. Li et al., (2019) analyzed the effects of the combination of a vertical fault and weak horizontal layer on slope stability with complex bedding planes using the 3D finite element strength reduction models and reported that vertical faults had less influence on slope stability. Additionally, the interaction of the fault and weak layer developed a substantially large damage zone, rendering the slope highly susceptible to instability. Vick et al., (2020) investigated the mechanism of rock slope instability by incorporating foliation, faults, and rock cracks. Based on a field investigation, they determined that the sliding of the fault led to the formation of tension cracks at the back scarp of the slope, and landslides occurred along the foliation plane because of rainfall. These studies clarified that the presence of discontinuous geological structures increases the risk of slope failure.

The aforementioned studies on geological structure-related slope instability were conducted on rock slopes that did not involve mining activities. With respect to geological structures in open-pit mines, Nie et al., (2015) analyzed the mechanism of landslides occurring in an open-pit mine by comparing field monitoring data with the data calculated using the limit equilibrium method. They reported that excavation caused the slope to lose support, thereby increasing the sliding force. The excavation further resulted in the failure of the weak interlayer with low shear strength by reducing the vertical stresses in the slope. Amini et al., (2019) investigated the toppling failure that occurred at an open-pit mine using the finite element technique. The results indicated that the shear strain was significantly concentrated on the alteration of the rock layers and the vertical fault owing to excavation, which caused slip along the altered rock layer. This slip eventually resulted in the toppling failure of the external anti-dip layered slope.

The aforementioned studies highlighted the influence of both excavation and discontinuous geological structures on slope deformation and instability. However, the deformation observed in the quarry of Mt. Buko has not been adequately explained by existing studies. Additionally, the verification and validation in previous studies were insufficient as the rock slope deformation and instability were examined based only on numerical simulations without considering sufficient field monitoring data. Therefore, a comprehensive analysis is required to characterize discontinuous geological structures in mining activities to gain a better understanding of their influence on the deformation and instability of rock slopes.

1.2.5 Effect of countermeasures for slope stabilization

Countermeasures for slope deformation and failure are essential to ensure the stability of rock slopes, protect infrastructure, and safeguard human lives. Common countermeasures for slope stabilization include constructing retaining structures, such as stone wall, buttress and rockfill embankments, to enhance structural support and counteract destabilizing forces (Sarma et al., 1979; Ulusay et al., 1993; Ahmad et al., 2016; Moriya et al., 2016; Hicks and Li, 2018). Advanced drainage systems are implemented to control groundwater flow, reduce pore water pressure, and mitigate hydrological impacts on slope stability (Lee et al., 2007; Ma et al., 2015; Yamatomi et al., 2018; Gao, 2024). Additionally, rock mass reinforcement techniques, such as the application of anchors, rock bolts, and shotcrete, are employed to increase shear strength and cohesion within the rock mass (Mike et al. 2002; Ballou et al., 2004; Malmgren and Nordlund. 2008; Chen. 2014; Zheng et al., 2019). Surface protection measures, including vegetation cover, geotextiles, or geomembranes, are used to minimize erosion and limit water infiltration (Hassanin et al., 1993; Van Santvoort. 1994; Kateb et al., 2013; Ingold. 2013; Koerner et al., 2017). These strategies effectively mitigate slope deformation, enhance structural integrity, and address external influences such as rainfall, excavation-induced stresses, or seismic activity, thereby supporting the long-term stability and safety of slopes.

In the field of rock slope stabilization, various engineering interventions have been developed and studied to mitigate deformation and prevent failure. Zhang et al. (2020) study the application of shotcrete, a process where a mixture of cement, sand, and water is sprayed onto the rock surface to form a protective and reinforcing layer. discuss how this method improves surface stability and prevents weathering-induced degradation. Ortigao et al. (2004) explain installation of rockfall barriers serves as a preventive measure against falling debris from unstable slopes. They examine the effectiveness of these structures in intercepting and controlling rockfalls, thereby safeguarding infrastructure and human lives. Mike et al. (2002) explores the application of fiber-reinforced shotcrete in stabilizing soil and rock slopes. It emphasizes the importance of correct mix design and highlights the ease with which shotcrete technology can be adopted by construction crews. Similarly, Ballou et al. (2004) discusses the aesthetic and cost benefits of using fiber-reinforced shotcrete for slope stabilization. It underscores the material's ability to blend into natural landscapes while providing structural support.

Recent studies have highlighted the critical role of retaining walls in slope stabilization, offering insights into their design, performance, and innovative applications. Gu et al. (2009) provides a comprehensive overview of methodologies for analyzing slope stability and the use of retaining structures to enhance safety, setting the groundwork for understanding their application. Building on this, Kumar et al. (2024) emphasizes the strategic placement of retaining walls in disaster-prone areas, highlighting their effectiveness in mitigating landslides by counteracting lateral soil pressures. Sundaravel et al. (2023) delves into reinforced earth retaining walls, presenting a detailed evaluation of their stability and serviceability, and introducing advanced reinforcement techniques to improve performance. Kokada et al. (2024) compares traditional counterfort retaining walls with an innovative variation featuring relief shelves, demonstrating improved load distribution and enhanced structural efficiency. Ukritchon et al. (2017) introduces an optimization framework that integrates slope stability considerations into the design of reinforced concrete cantilever walls, ensuring both structural integrity and cost efficiency.

1.2.6 Previous studies of Mt. Buko

Many researchers have given different views of deformation mechanisms for Mt. Buko in the past (Aoyama et al., 2018; Yamaguchi et al., 2018; Kondo et a., 2018; Ozawa et al., 2018; Yamatomi et al., 2018; Ogawa et al., 2022). These perspectives include the effects of rainfall, excavation, low-angle cracks, and the weak rock zones.

The dominant view is that sliding of the parallel weak rock zone (PZ) leads to sliding of the slope surface. Aoyama et al. (2018) conducted a detailed statistical analysis of monitoring data from discontinuities distributed within the parallel weak rock zone and found a significant correlation between shear displacement of discontinuities and overall slope surface deformation. Remarkably, the shear displacement in the weak rock zones exhibited a fixed proportional relationship with surface deformation over the last fourteen years.

Some previous studies have attempted to analyze the relationship between slope displacements with rainfall. Yamaguchi (2018) and Kondo et al. (2018) investigated the relationship between slope surface deformation and rainfall over the past five years. Their findings revealed that rainfall significantly affected the deformation, and the water table responded sensitively to rainfall events. Ozawa et al (2018) et al. classified the observed deformations into Type I deformations associated with excavation and Type II deformations associated with rainfall. However, increased deformation during periods without rainfall remains unexplained. In particular, the cause of deformation initiation cannot be explained by rainfall alone.

As mentioned in Section 1.2.3, mining-induced deformation are often complex and characterized by the shape, angle of the slope, and the properties of rock mass. The deformation characteristics show different before and after the excavation level pass the vertical weak rock zone (Fig. 2.10) in section A-A'. Although Ogawa et al. (2022) concluded that the mining is one of the most important reasons for the occurrence of slope deformation, different mining areas with almost the same excavation rate and dimensions show different deformation characteristics, which make it difficult to explain how excavation affect the slope deformation.

Moreover, despite the contribution to the change in distance is small, the effect of low-angle cracks distributed in the limestone layer cannot be ignored. Aoyama et al. (2018) points out that the shear displacements of No.1 and No.3 cracks located in limestone cover rock show a high degree of correlation with the downward displacement of the surrounding rock mass.

In summary, the mechanism of deformation in Mt. Buko should be complex, which includes the effects of excavation, geological structure, and rainfall. Especially the effect of weak rock zones, how it slides and why it stops gradually needs to be explained urgently.

1.3 Content of research

In this study, the cause of the long-term deformation of Mt. Buko was successfully elucidated for the first time, and a novel deformation mechanism was proposed based on the relationship between geometric characteristics of the weak rock zones and excavation state. In addition, based on the proposed deformation mechanism, the effects of the stone wall were evaluated for different dimensions and construction timings. The findings provide a reference to future excavation at Mt. Buko and to stability assessment of rock slopes in open-pit mines with similar weak rock zones.

In chapter 1, the general overview on the assessment of rock slope stability is given. The objectives of the research are explained.

In chapter 2, the deformation issues, geological conditions, monitoring systems and stone wall countermeasure at Mt. Buko are systematically introduced. The slope deformation characteristics and challenges based on the long-term observation data are summarized.

In chapter 3, 2D section numerical models with discontinuous structures are developed based on the geological map and mining history of the quarry. The simulation results are compared to the measurement results. The mechanism of slip movement during excavation progress in numerical models are discussed. In addition, an interpretation of long-term deformation at the quarry is provided based on the proposed slip mechanism, along with a discussion of the quantitative differences between measurements and simulations.

In chapter 4, the effectiveness of the current stone wall at Mt. Buko is verified by numerical analysis. The effect of stone wall properties such as Young's modulus, Contact stiffness, Poisson ratio, and density are discussed to understand the mechanism of the stone wall against the slip deformation. Moreover, the optimal dimension of the stone wall at Mt. Buko is investigated and recommended by varying its height and width.

In chapter 5, the general effects of the weak rock zones on mining-induced deformation are investigated. The effects of dip direction of weak rock zones and connectivity, the thickness of cover rock and triangular zone are comprehensively assessed based on the simplified models. The effects of a stone wall on restraining slip deformation are also examined, focusing on the factors such as height, width, and construction timing.

Chapter 6 summarizes the main conclusions of this study and provides recommendations for future research and applications.

2. Overview and characteristics of rock slope deformation at Mt. Buko

2.1 Summary of Mt. Buko

Mount Buko is a mountain in Chichibu, Saitama prefecture, Japan (Fig. 2.1). The origin of the name is recorded as Yamato Takeru dedicated his armor to the rock chamber of this mountain. As a largest limestone open pit mine in Japan, the annual production in recent years is around 7 million tons.

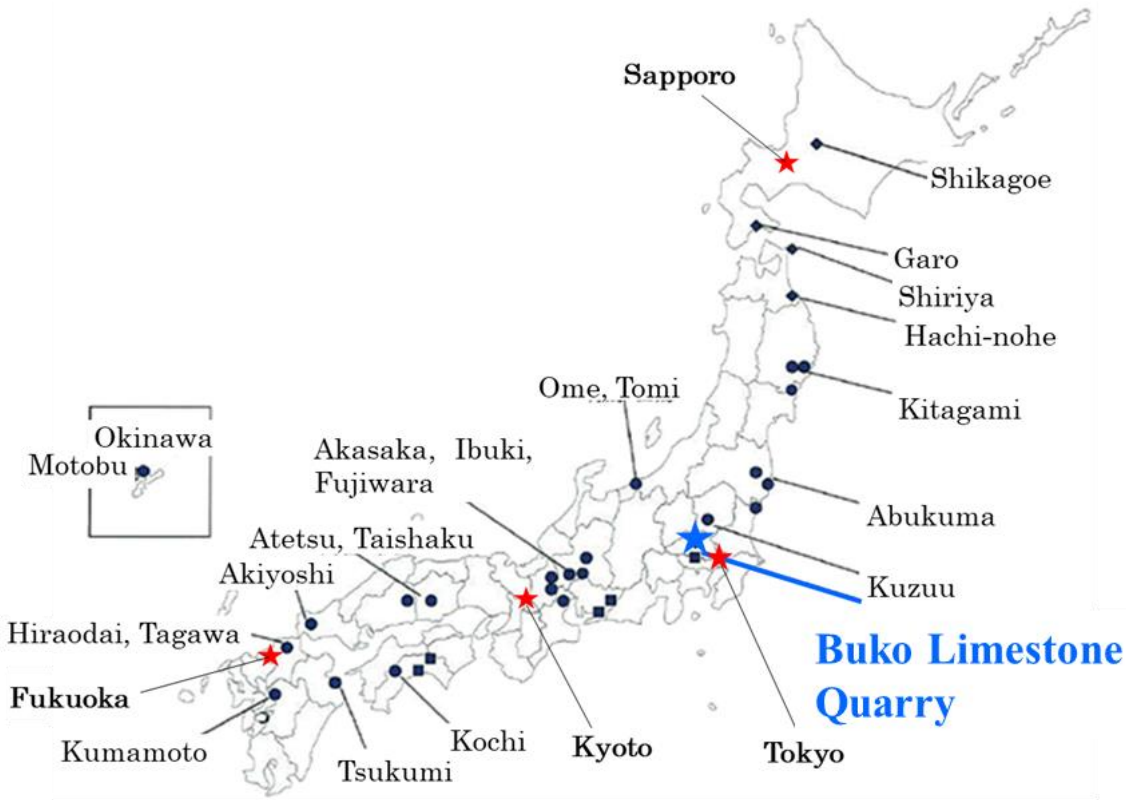

Fig.2.1: Location of Mt. Buko.

The mine is documented to have gone on excavation from Edo period, and has been officially mined from the top of the mountain at an elevation of 1,304 m since 1915. The working face of the mine extends approximately 2 km from west to east, and the height of the rock slope is approximately 400 m at present (Fig. 2.2). The mine is currently divided into three mining areas, being excavated by 3 companies, from west to east, they are Minowa, Une, and Buko mines. Mining is expected to continue until 2050, with the height of the rock slope reaching more than 700 m at mine closure.

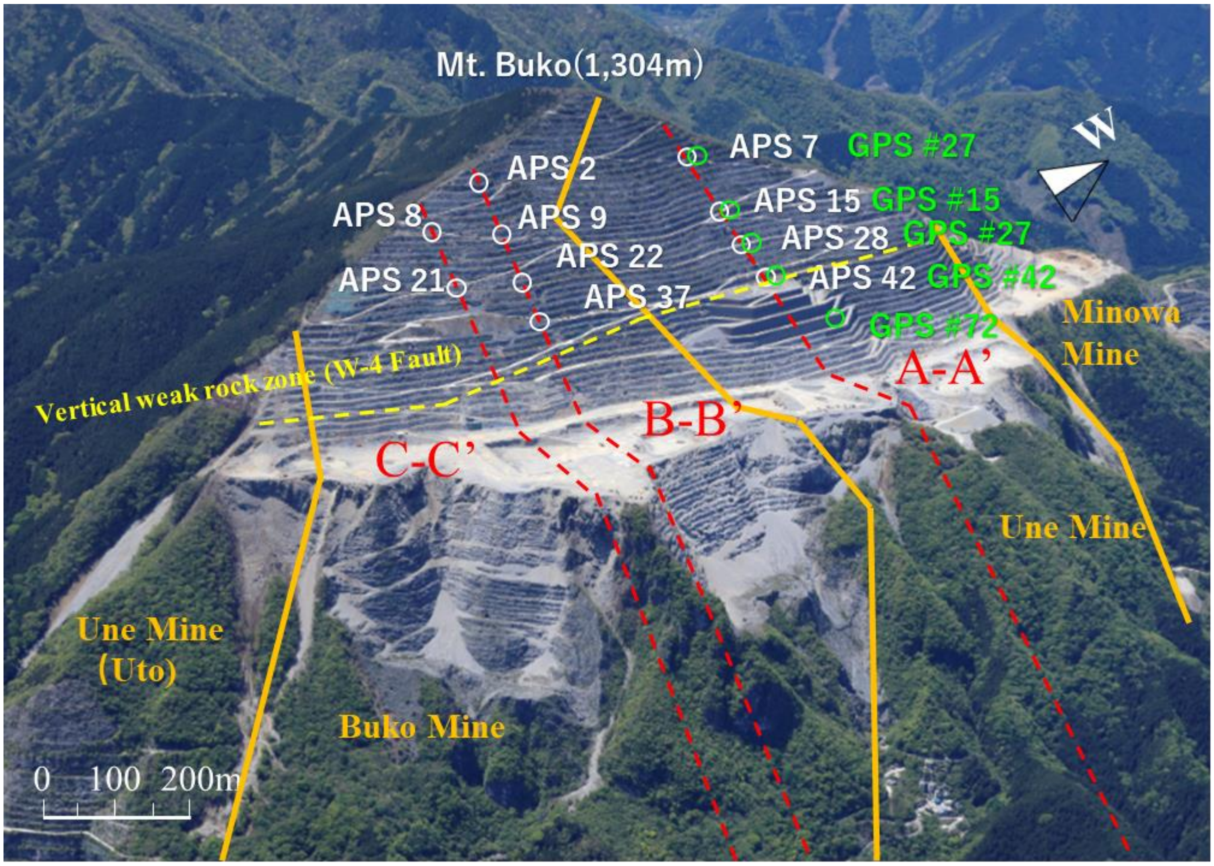

Fig.2.2: An aerial view of the rock slope of Mt. Buko, the while circles (i.e. APS 8) represent APS monitoring points, the green circles (i.e. GPS#7) represent GPS monitoring points.

2.2 Geological and hydrogeological conditions

2.2.1 Rock formation

Limestone and green rock formations are mainly distributed in the mining area. The limestone formation generally trends northwest-southeast and dips steeply to the north (Fig. 2.3, Yamatomi et al.,2018). The limestone deposits (Fig. 2.4a and 2.4b) have a maximum width of 1,000 m but converge towards the east and west (Eang et al., 2018). Dip angle of the geological boundary between the limestone deposit and the green rock formation from the mountain peak to around the 1,000 m level is approximately 45°, but below 1,000 m, it increases to over 60°. While the fresh green rock layers are solid, they show signs of weakening due to weathering caused by water present in cracks, joints, and weak zones associated with structural movements (Fig. 2.4e and 2.4f). Especially near the boundary of the formations, the green rock formation is brittle, with developed foliation and slickensides, making them prone to flaking into small fragments (Yamatomi et al., 2018). To prevent the weathering and alteration of the green rock formation, some of the limestone on the upper side is left unmined as a protective cover rock.

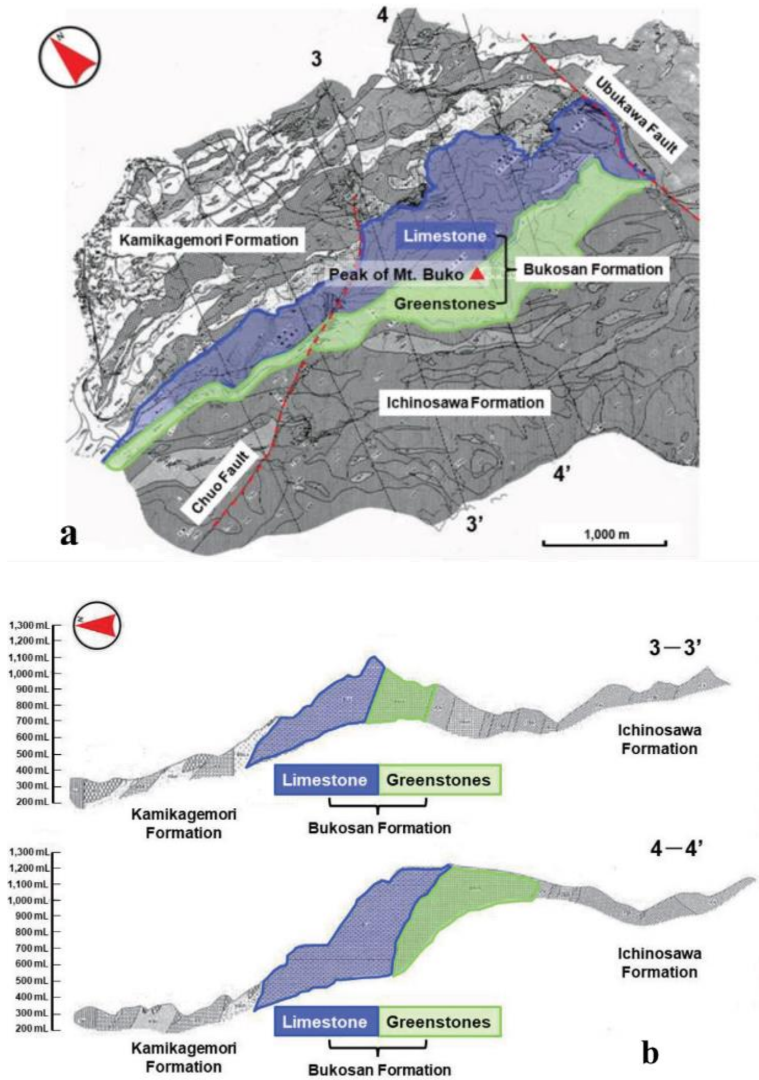

Fig.2.3: (a) Geological plan view of Mt. Buko, limestone and greenstones. (b) Geological cross sections of Mt. Buko, limestone and greenstones (Yamatomi et al., 2018).

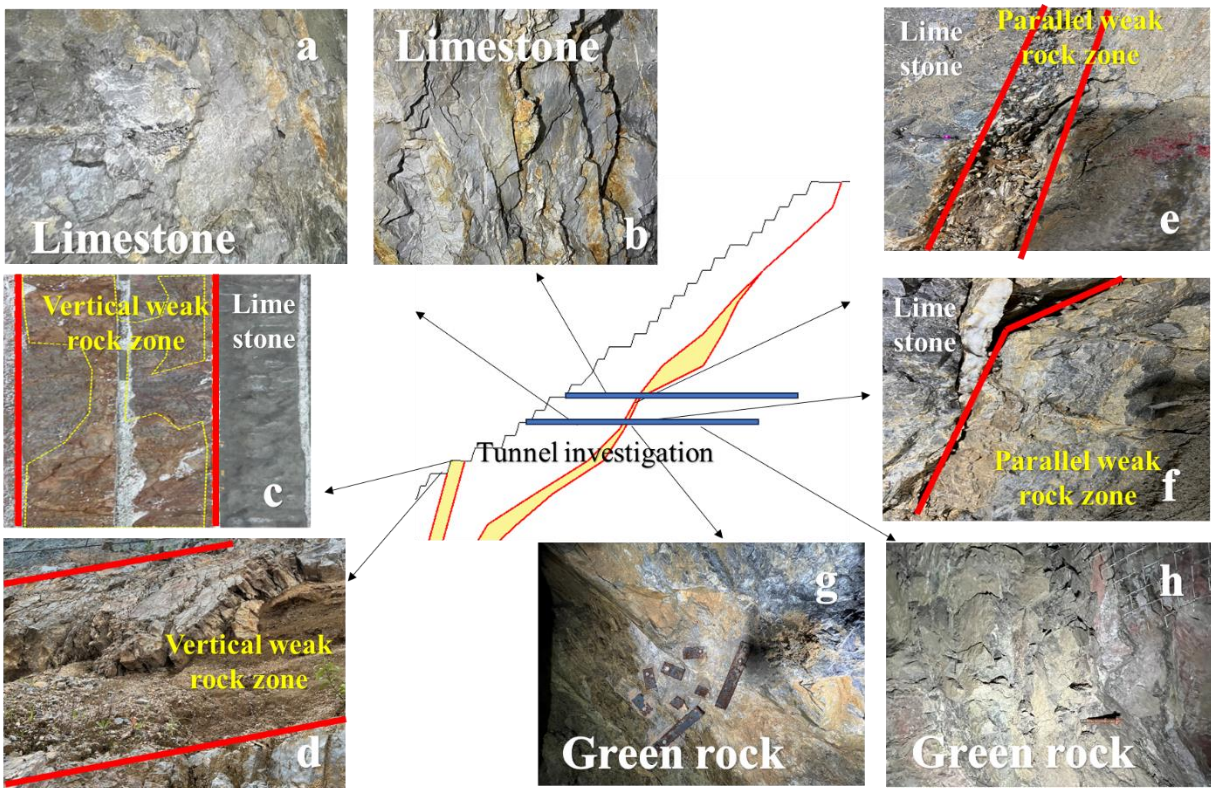

Fig.2.4: Rock mass and the weak rock zones in the case study quarry. The yellow dashed line in Fig. 2.4c shows the distribution of clay.

2.2.2 Weak rock zones

Two major weak rock zones are developed in the cross-section under the mining area and presenting different spatial characteristics in different sections. The first one, referred to as VZ, is a nearly vertical weak rock zone. The VZ is basically a near east-west fault (W-4 fault in Figs 2.2 and 2.5). The second one, refereed to as PZ, is an inclined geological boundary between the limestone and green rock, which is nearly parallel to the slope surface. Certain discrepancies were observed in the geometric characteristics of the cross-sections with respect to the connectivity of the geological structures. Particularly, in the case of A-A' in Fig.2.2, the PZ is connected to the VZ (Fig. 2.5a). In the case of sections B-B' and C-C', no connection is formed between the VZ and PZ (Figs. 2.5b and 2.5c). Accordingly, weak rock zones in Mt. Buko considered in the case study can be classified as (i) connective patterns and (ii) non-connective patterns.

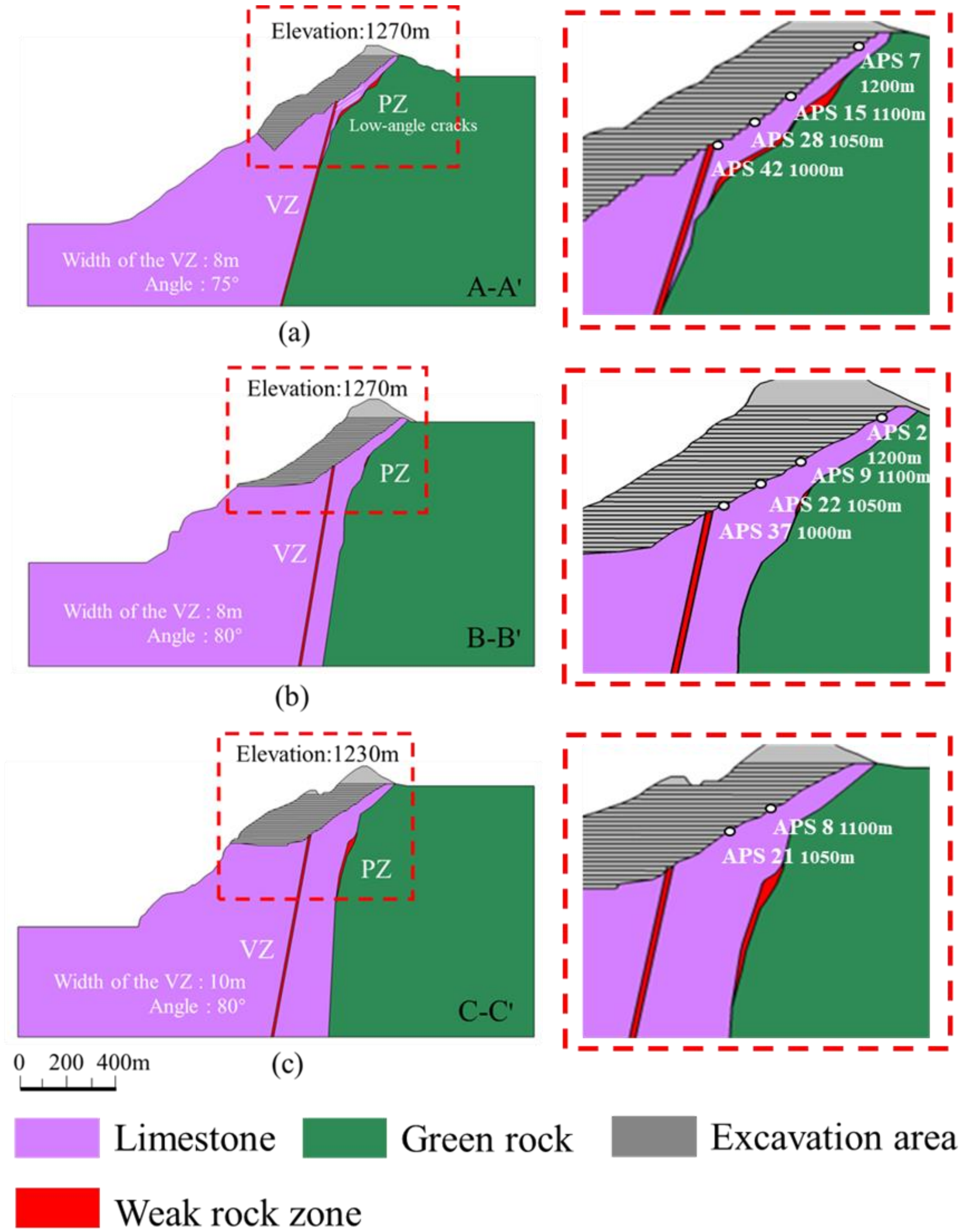

Fig.2.5: Geological condition of Mt. Buko on 3 sections in Fig. 2.2. (a) section A-A'. (b) section B-B'. (c) section C-C'.

2.2.3 Hydrogeological condition

In past investigations, rainfall has been a significant contributor to change in slope water levels. Considering that rainfall has a significant effect on the stability of slopes and the high-water storage capacity of the weak rock zones, some boreholes for monitoring groundwater level were set up in the Une mining area (Fig. 2.6, Kondo et al., 2018).

Fig. 2.6 shows the long-term fluctuation of groundwater level for 5 years with rainfall. Although groundwater levels tend to increase in response to rainfall at all boreholes, UN111 on the lower part increase the most significantly, while the other boreholes, M2010-2 and M2010-3, in the upper side showed slightly water level change. Based on monitoring data of the water level change, the predicted water level at heavy rainfall is plotted in Figure 2.7.

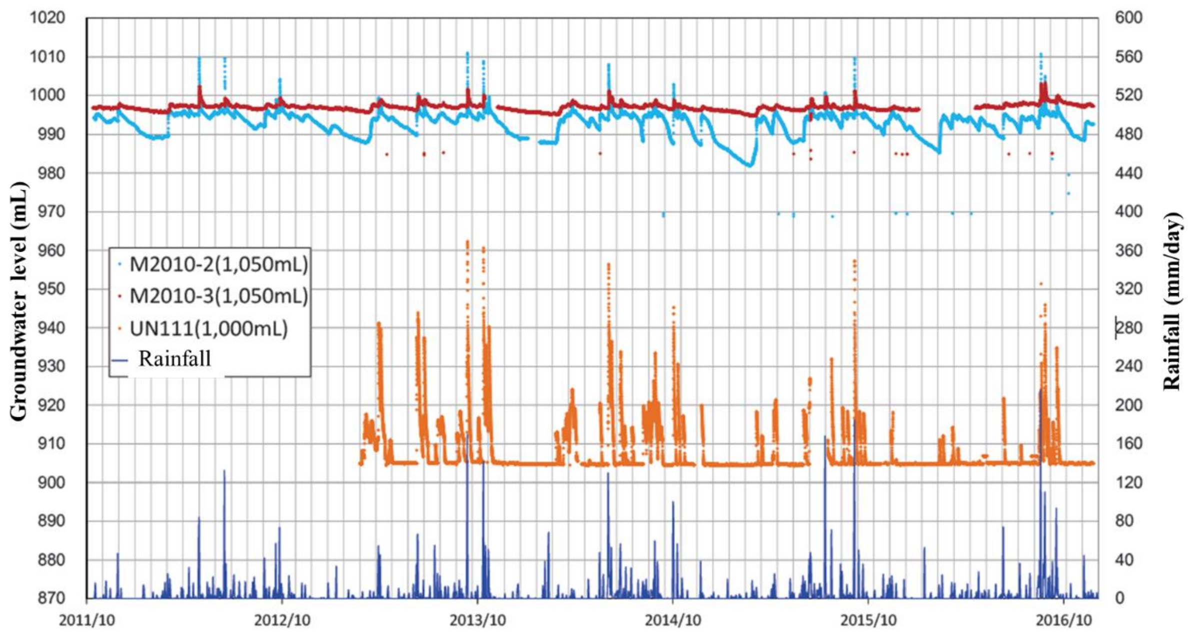

Fig.2.6: Long term fluctuation of groundwater level (M2010-2, M2010-3, UN111) (Kondo et al., 2018).

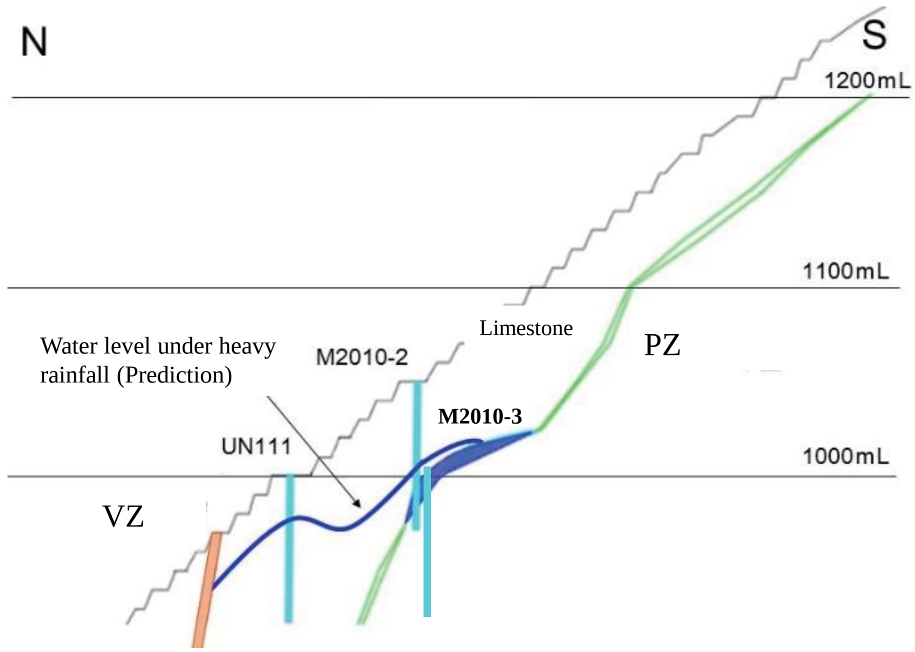

Fig.2.7: Location of the groundwater monitoring points and influence of geological structure on rising groundwater level (Kondo et al., 2018).

2.3 Countermeasures

In response to the rainfall and long-term deformation issues in Une mine (west side of Mt. Buko) mentioned in 2.2, draining and stone wall countermeasures were started from 2007 and 2013 (Yamaguchi et al. 2018), respectively.

As shown in Figure 2.8a, a total of 23 H-type steel pipes for drainage were set at 1,010 m (10 steel pipes) and 1,050 m (13 steel pipes) (Yamaguchi et al., 2018). As described in Chapter 5, the stone wall (Fig. 2.8b) were constructed to restrain the slip deformation. The current stone wall ranges from 930 m to 1,000 m with about 100 m width. The overall slope angle and shape consist of the original excavation bench. The construction period was from 2013 to 2017. In the future, although there are plans to expand the scale of the current stone wall to a higher level, the design is still under discussion.

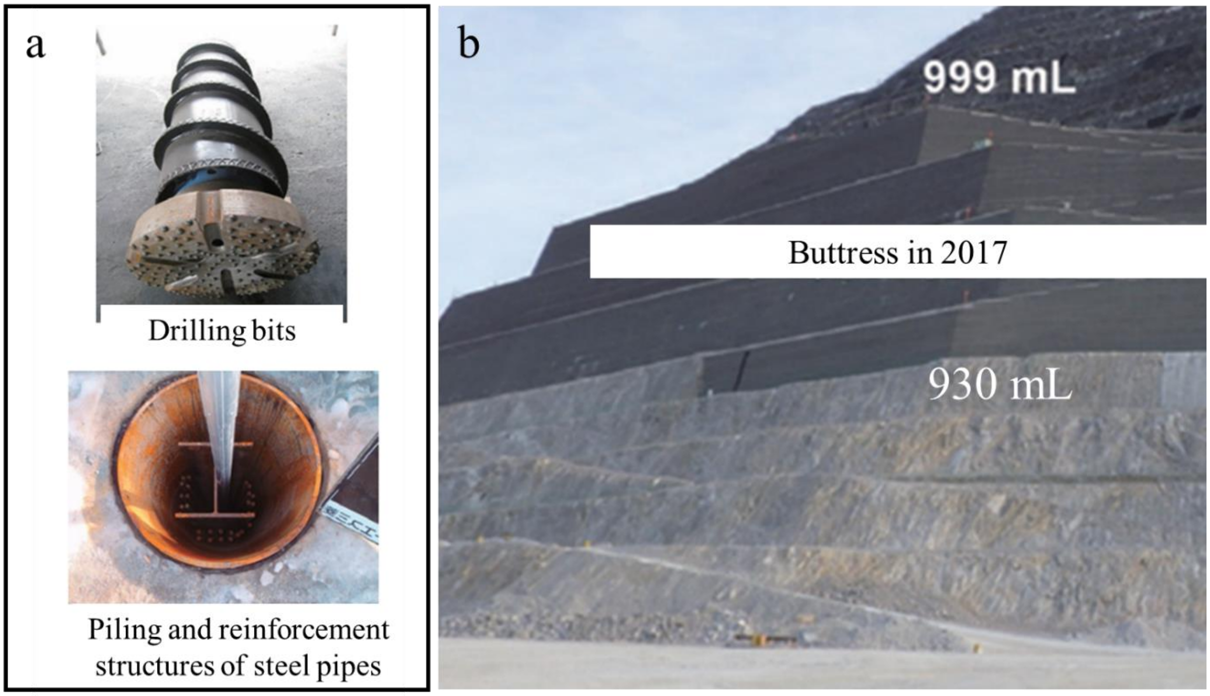

Fig.2.8: Countermeasures in Une mine. (a) Draining pipe. (b) Stone wall (Yamaguchi et al., 2018).

2.4 Measurement of the rock slope displacement

In 1994, the Automated Polar System (APS) was introduced at the quarry to address concerns regarding mining safety (Yamaguchi, 2018). The rock slope has been continuously monitored for over 30 years. APS consists of mirrors, which are placed on the slope surface, and a distant beam generator. The beam generator is located 4.5 km away from the top of the rock slope in Mt. Buko (Fig. 2.9). The change in distance between the beam generator and each mirror is measured 12 times/day with accuracy of ±0.12 mm.

However, the measurement results are often influenced by meteorological conditions, such as temperature and humidity. To mitigate these effects, relative displacements to a reference mirror point located in a similar meteorological environment are computed (Nakatani et al., 2018).

To further improve accuracy, two methods were implemented. First, mirror points near section B-B' exhibited negligible displacement over the monitoring period according to GPS measurements (Fig. 2.10a). Therefore, the distance changes at other mirror points were calibrated from the mirror points located at the same elevation near section B-B'. Second, GPS devices were installed around the APS mirrors to verify deformation behavior. GPS monitoring, initiated in

2005, has validated the reliability of APS measurement results through extensive data collection (Yamaguchi, 2018).

In addition to APS and GPS, extensometers and crack gages (Fig. 2.10b) have been introduced to enhance the measurement of rock slope deformation in limestone, green rock and their boundary. Extensometers track expansion or contraction of rock mass by detecting relative displacements between multiple anchor points (Ogawa et al., 2024). Crack gages, consisting of two sensors, measure relative movement of crack surfaces in both normal and shear directions.

Fig.2.9: APS working mechanism and components.

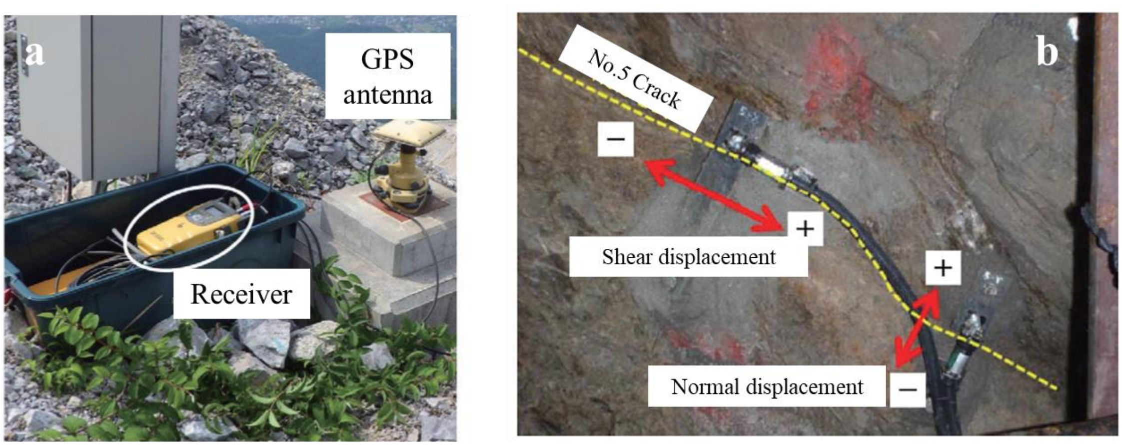

Fig.2.10: Measurement system in Mt. Buko. (a) GPS. (b) Crack gages.

2.5 Deformation and excavation history of the quarry

Fig. 2.11 depicts the changes in distance at mirror points in sections A-A' and C-C' in Fig. 2.2. APS 7-2, 15-9, 28-22, and 42-37 in Fig. 2. 11a denote the changes in distance in section A-A' at elevations of 1,200 m, 1,100 m, 1,050 m, and 1,000 m, respectively, whereas APS 8-9 and 21-22

(2. 11b) denote them in section C-C' at elevations of 1,100 m and 1,050 m, respectively. The first and second numbers in these expressions denote the target and reference mirror points at the same elevation, respectively. Negative quantities corresponded to a decrease in the distance.

The curves of the two sections indicated that the change in the distance in section A-A' was significantly different from that in section C-C'. In the case of section C-C', the distance remained nearly unchanged, whereas the distances in section A-A' decreased with time, indicating that each point continued to move in the forward and/or downward direction. The changes in distance in section A-A' can be summarized as follows. Initially, the distance decreased slightly at a nearly constant rate. However, as shown in Figs. 2.11 and 2.12, certain stepwise changes occurred after the excavation level passes the VZ level in 2004, which accelerated the rate of decrease. These stepwise changes did not occur after excavation level far away from the VZ level (2016), and the rate of decrease decelerated, indicating a convergence trend in all curves. The occurrence of stepwise changes, such as those in 2007 and 2011, concurred with heavy rainfall events (Ozawa et al., 2018).

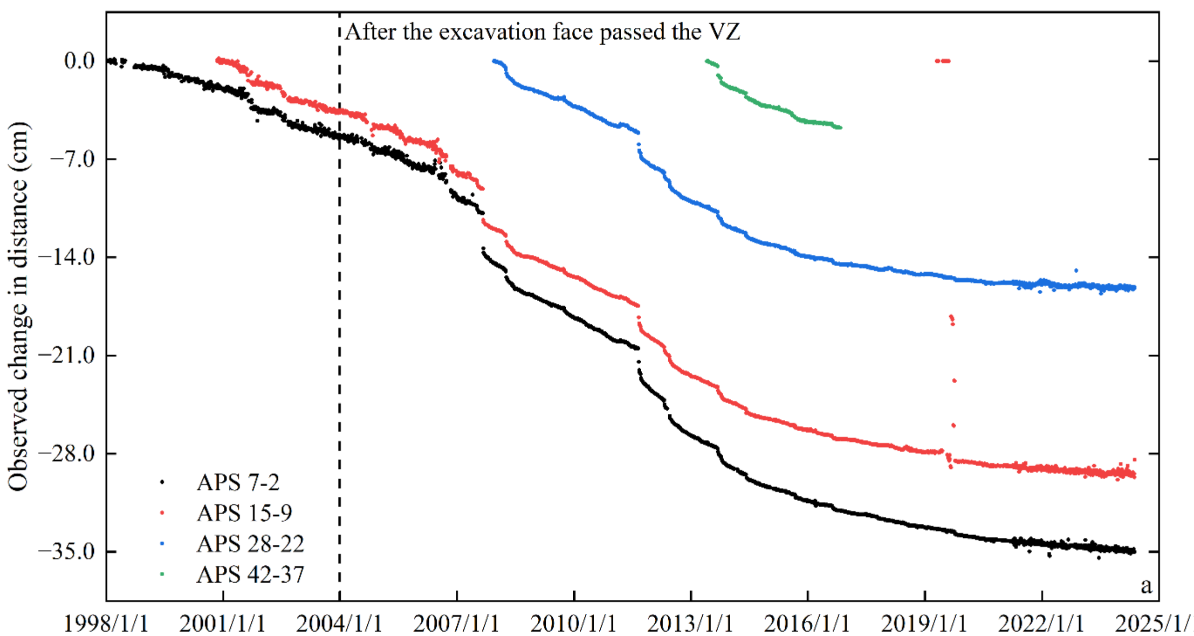

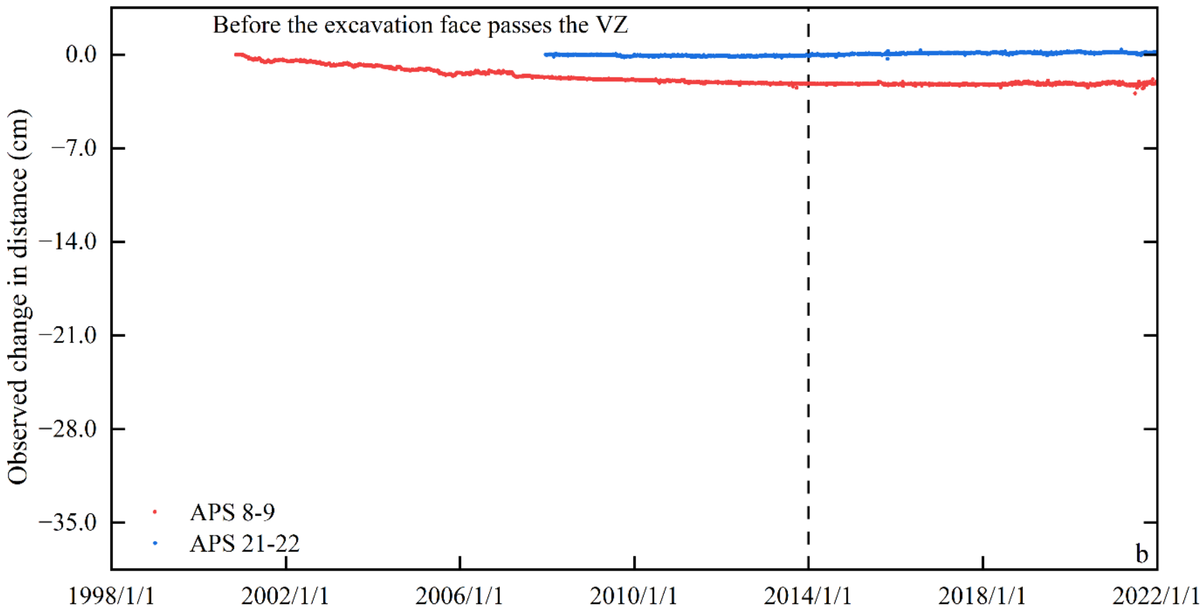

Fig.2.11: Change in distance results in section A-A' (a), and section C-C' (b).

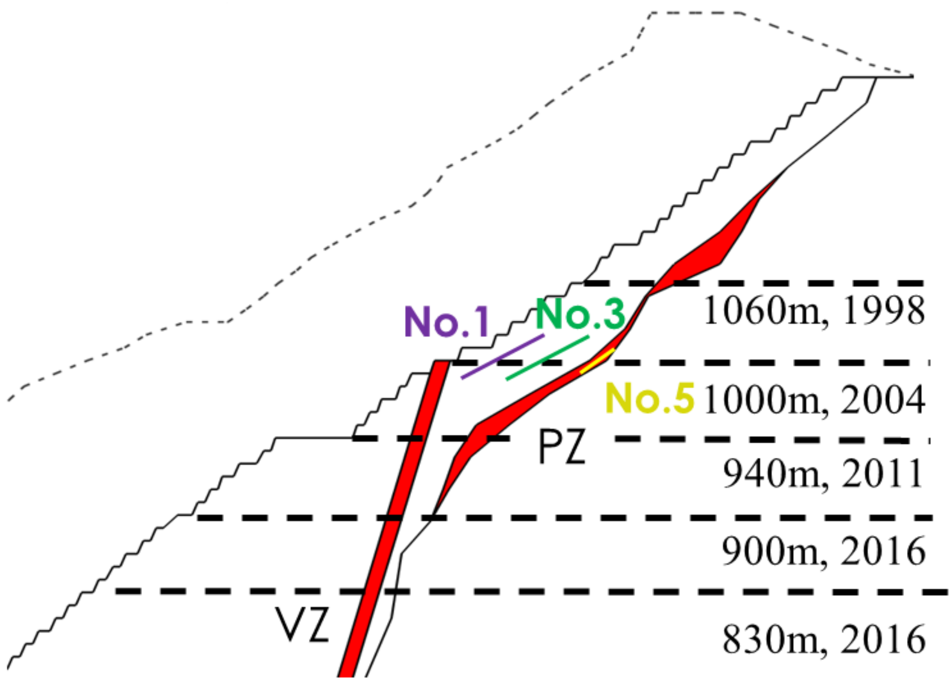

Fig.2.12: Typical excavation levels in different years and locations of low-angle cracks.

Fig. 2.13 shows the displacement vectors in section A-A' measured by GPS (Fig. 2.2) from 2011 to 2016 (Nakatani et al., 2018). All GPS points showed forward-downward displacement in the upper side of the VZ. However, directions of the displacement changes with elevation. The horizontal component relatively increases with the decrease in elevation. What's more, it is noted that GPS 72 located on the front side of the VZ (Triangular zone in Fig. 2.13) shows a forward-upward displacement.

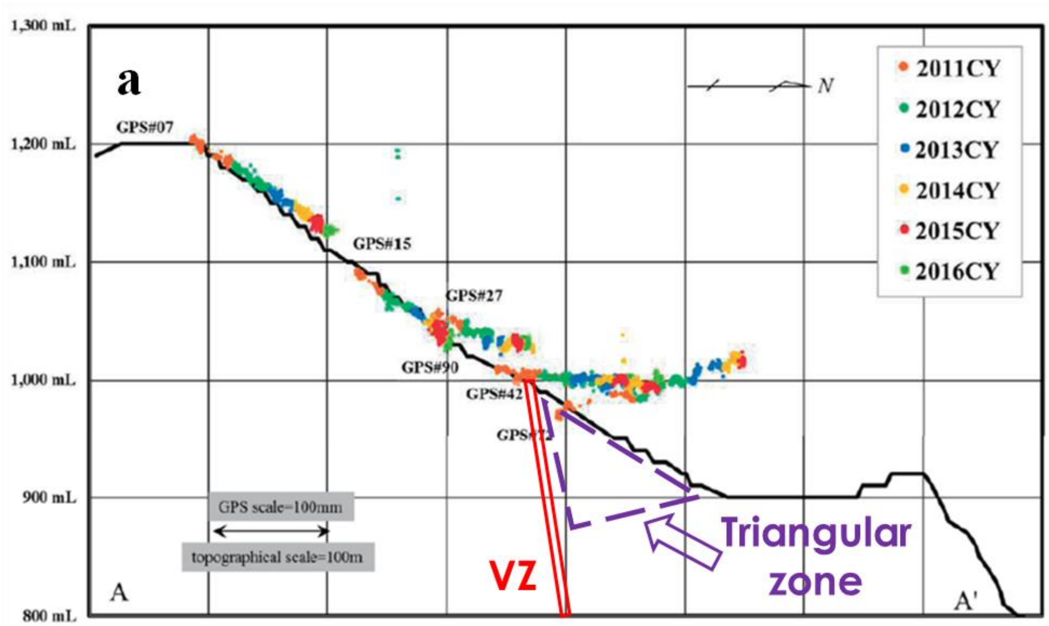

Fig.2.13: Observed GPS data from 2011 to 2016 (Nakatani et al., 2018), the color dots show annual displacement in calendar year (CY).

Fig. 2.14 illustrates the cumulative shear displacements of Cracks No. 1, 3, and 5, all located along the survey tunnel at 1,010 m (Fig. 2.12). Cracks No. 1 and 3 are located in the limestone whereas Crack No. 5 is located within the PZ. Although the shear displacement at all points continuously increased from 2010 to 2024, but the increment gradually decreased. The shear displacement at Crack No. 5 within the PZ is greater than Cracks No. 1 and 3 within the limestone. Aoyama et al. (2018) analyzed the relationship between the distance changes at APS 7 and the shear displacement of Crack No. 5. The results demonstrate there is a strong correlation between them (Fig. 2.15). This suggests that the slip deformation of the slope surface is closely related to the shear displacement of the PZ.

As seen in Fig. 2.15, the change in distance at APS 7 has been approximately 1.6 times the shear displacement of No.5. The ratio of the change in distance to the shear displacement tends to increase to 2.2 since 2018. The drainage described in Section 2.3 might cause the increase in the ratio.

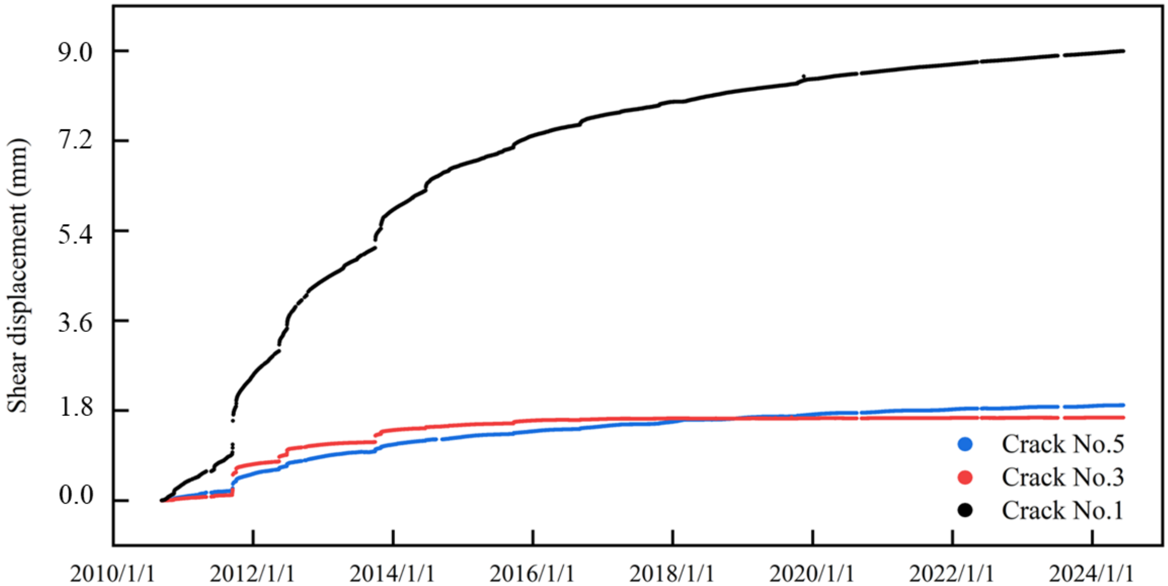

Fig.2.14: The cumulative shear displacements by year of low-angle crack No1, 3, and 5.

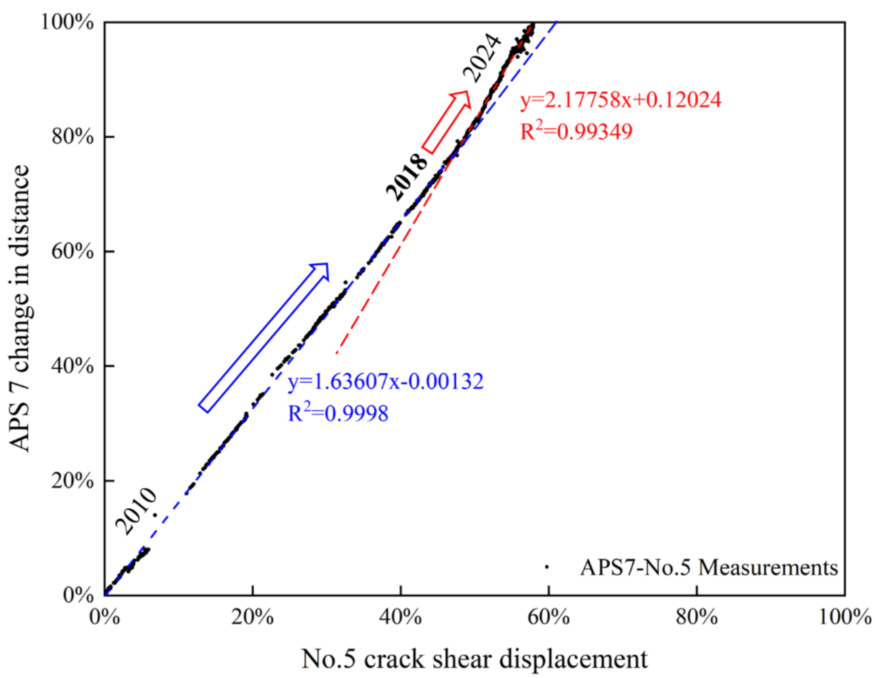

Fig.2.15: Relationship between displacement obtained from APS7-2 and crack No.5 (Aoyama et al., 2018).

2.6 Concluding remarks

In this Chapter, the deformation issues, geological conditions, monitoring systems, mining history and stone wall countermeasure at Mt. Buko are systematically introduced. The following characteristics among the mining-induced deformation, mining state, and the weak rock zones were cleared from analysis of measurement results:

1. Sliding movement occurs only in section A-A', where the parallel weak rock zone is connected with the vertical weak rock zone. This indicates that the displacement on the slope surface is closely related to the slip deformation occurring within the PZ.

2. The deformation rate accelerated once the excavation level passed below the VZ, then gradually decreased and converged as the excavation level moved further away from the VZ.

3. The horizontal component of slip deformation on the slope surface increases with decreasing elevation, and forward and upward displacement can be seen in the front side (triangular zone) of the VZ.

In Chapter 3, the deformation mechanisms of the rock slope at Mt. Buko are considered. It should be noted that the mechanism qualitatively can explain the three aforementioned characteristics.

3. Numerical simulation of mining-induced deformation of Mt. Buko

3.1 Introduction

In Chapter 2, we discussed the long-term deformation issues at Mt. Buko. While there are various perspectives on the causes of this deformation, a clear understanding of the mechanism behind slip deformation generation remains lacking. Specifically, the interaction between excavation levels, weak rock zones, and mining-induced deformation could be the key to explaining the observed long-term deformation.

In this chapter, we aim to scientifically interpret the deformation behavior of the rock slope at Mt. Biko cleared in Chapter 2 for assessment of the rock slope stability in the subsequent excavation period. Specifically: 1. Develop 2D simulation models incorporating the weak rock zones as discontinuities to estimate mining-induced displacements and compare them with field measurements. 2. Analyze the influence of weak rock zones on mining-induced displacements to elucidate the slip deformation mechanism. 3. Discuss the possible causes of the quantitative difference between the simulation results and the field measurement. 4. Evaluate the slope stability based on the proposed deformation mechanism.

3.2 Simulation model

3.2.1 Numerical models for the geological section at Mt. Buko

The 2D numerical methods for section A-A', B-B', and C-C' were constructed based on the vertical section maps of the quarry (Fig. 2.5). All three models were 2,500 m wide with two weak rock zones each. The dip angle and width of the VZ were set to 75-80° and 8-10m based on the geological map, respectively. The PZ was an interlayer composed of limestone and green rocks and its distribution in the three sections varied owing to differences in weathering. As depicted in Section 2.2.2, the PZ was continuously distributed along the geological boundary in section A-A', and its extension line intersected with the VZ. In contrast, the PZ in section C-C' was nearly parallel to the VZ and did not extend along the boundary at a higher level than the VZ. In section B-B', the PZ was nearly absent.

Limestone and green rock are modeled using an elastic approach, based on observations that the site does not exhibit significant plastic deformation. The approach to model the mechanical effects of weak rock zones is provided by the Universal Distinct Element Code (UDEC) manual

(Itasca, 2021), where discontinuous deformation at the boundaries between weak rock zones and the surrounding rock mass is represented. These boundaries are treated as discontinuity planes within the discrete element method framework. Additionally, although various constitutive models have been developed to simulate weak rock zones, our comparison showed that they have little impact on the overall results within the section models. The model specifically focused on the discontinuity of the weak rock zone, emphasizing its critical role in deformation measurements. Therefore, the weak rock zones were modeled as elastic but with a reduced Young's modulus to reflect their greater deformation capacity (Fig. 3.1).

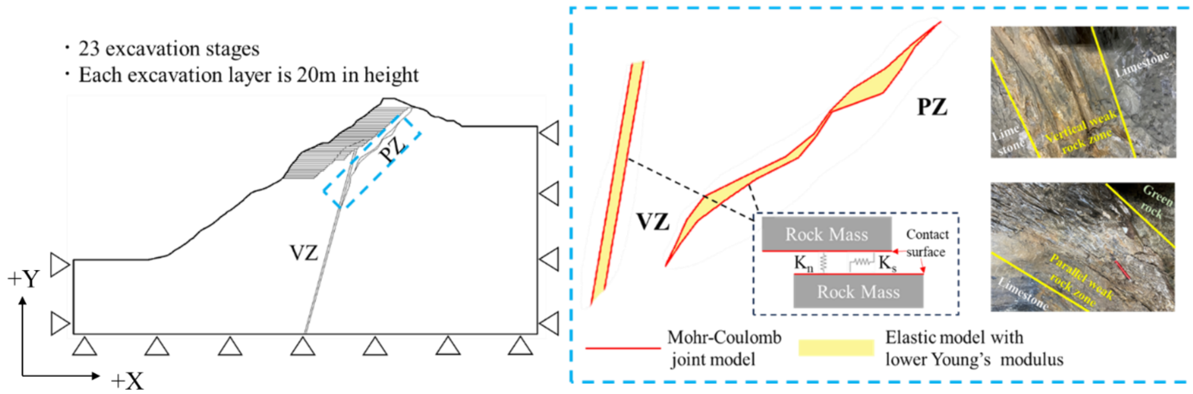

Fig.3.1: Simulation model and constraint condition.

3.2.2 Model parameters

The elastic moduli of the rock mass and the weak rock zones were estimated from those of intact rocks, considering the geological strength index (GSI) (Marinos and Hoek. 2000). Table 3.1 summarizes the elastic properties of intact limestone and green rock by laboratory test.

The GSI of limestone (Figure 2.4a, b) and green rock (Figure 2.4g, h) were estimated to be 70 because limestone with rough discontinuities was strongly interlocked, undisturbed, and almost unweathered. The GSIs of the weak rock zones (Figure 2.4c-f) were estimated to be 30 as they were formed by multiple intersecting discontinuity sets and highly weathered surfaces. The mechanical properties of the vertical weak rock zones were estimated based on the Young's modulus of the intact limestone because the VZ was formed in the limestone deposit, whereas the parallel weak rock zone was estimated based on both intact limestone and green rock because the PZ was composed of alternating layers of limestone and green rock.

The estimation of Young's modulus for limestone and green rock was based on five empirical equations shown in Table 3.2. It is important to note that the disturbance factor D in the equations often varies with the scale of excavation. In large open-pit mines, D typically ranges from 0.7 to 1 for overlying rock layers (limestone), while green rock types, which are less affected and located deeper, generally have D values between 0 and 0.7. For weak rock zones, Equation 5 was used to estimate Young's modulus, as it has shown excellent performance for rocks with clay interbedded layers. The estimated Young's moduli for limestone, green rock, and weak rock zones are shown in Table 3.3 with their density and Poisson's ratio.

Table 3.1: Elastic properties of intact host rock in the quarry by experiment.

Properties	Intact limestone	Intact Green rock
Density (kg m^{-3})	2548	2646
Young's modulus (GPa)	58.1	34.2
Poisson's ratio	0.25	0.25

Table 3.2: Estimation of rock mass Young's modulus based on various empirical equations.

Number	Equation	Reference	Limestone (GPa)	Green rock (GPa)	
(1)	$E_m = E_i\,(0.02 + \frac{1-D/2}{1+e^{\frac{60+15D-GSI}{11}}})$	Hoek et al. 2006	19.6 ~ 12.4	25.0 ~ 11.5	For Limestone, D= 1 ~ 0.7, For green rock, D=0.7~0.
(2)	$E_m = E_i\,(S^a)^{0.4}$, $\mathrm{S} = \exp\left(\frac{GSI-100}{9-3D}\right)$, $a = 0.5 + \frac{1}{6}(e^{\frac{-GSI}{15}} - e^{\frac{-20}{3}})$	Sonmez et al. 2004	24.3 ~ 21.3	17.5 ~ 14.3	
(3)	$E_m = E_i\,(S)^{\frac{1}{4}}$, $\mathrm{S} = \exp\left(\frac{GSI-100}{9}\right)$	Carvalho 2004	25.2	14.8	
(4)	$E_m = 0.35 * exp^{0.06GSI}$	Majdi et al. 2012	23.3	23.3	
(5)	$E_m = \sqrt{\left(\frac{E_i}{100}\right)10^{\frac{(GSI-20)}{35}}}$		20.4	15.6	

Table 3.3: Mechanical properties of rock mass in section models, assumed by GSI and experimental values.

Properties	Parallel Weak rock zone	Vertical Weak rock zone	Limestone	Green rock
Density ($kg \cdot m^{-3}$)	2597	2548	2548	2646
Young's modulus (GPa)	1.3	1.5	20	15
Poisson's ratio	0.25	0.25	0.25	0.25

As mentioned in Section 3.2.1, the geological boundary in three section models were modeled as a discontinuity plane in the discrete element method framework. Based on the Universal Distinct Element Code (UDEC) manual and previous studies (Table 3.3), numerical methods for discontinuous deformation typically treat these boundaries as rock-rock contact surfaces. K_n and K_s refer to the normal and shear contact stiffness of the contact surface, respectively. K_n and K_s determine the transfer of forces in the normal and shear directions on both sides of the contact surface.

Although K_n and K_s can be measured experimentally at the laboratory scale, determining their values for large-scale natural conditions is quite difficult. Additionally, setting K_n too low or too high can cause the model to fail to converge. Typically, K_n is close to the Young's modulus of the rock mass, as suggested in Table 3.4. Ultimately, K_n was chosen to match the Young's modulus of the PZ and VZ, respectively. Moreover, the ratio of K_n to K_s was assumed to be 2.0 based on Table 3.4.

The friction angle of limestone discontinuity is typically in the range of 30-40 degrees (Bandies et al., 1983; Peacock et al., 1994; Day et al., 2017; Morad et al., 2018). However, the presence of water often decreases the friction angle of discontinuities (Ranjith et al., 2018; Pirzada et al., 2020; Huang 2024). As described in Section 2.2.3 and 2.5, rainfall influences the rock slope deformation at Mt. Buko. This suggests that the friction angle along the geological boundary at Mt. Buko decreases during rainfall. Thus, the friction angle was adjusted to 15 degrees. Tables 3.5 summarize the specific values.

Table 3.4: Discontinuities parameters of different rock types.

Rock Type	K_n (GPa/m)	K_s (GPa/m)	K_n/K_s	Friction (°)	Young's modulus (GPa)	Resource
Limestone	6~10	4~8	1.3~2.5	31		(Day et al. 2017)
Limestone	4~6	3~4	1.0~2.0	36		(Bandis et al. 1983)
Limestone	9.4	4.9		34	57.0	(Morad et al. 2018)
Limestone	51.7	30.1	1.7		49.0	(Bandis et al. 1983)
Limestone	10	4.8	2.1	30	10.0	(Peacock et al. 1994)
Sandstone	11.7	5	2.3	30	11.5	(Jiang et al. 2008)
Shale	4.4	1.5	2.9	25	6.0	
Tuff	0.785	0.637	1.23	21	2.03	(Kuraoka et al. 2000)
Tuff	1.68	1.49	1.1	37	3.05	

Table 3.5: Mechanical properties of discontinuities.

Properties	Parallel weak rock zone – rock mass contact	Vertical weak rock zone – rock mass contact
K_n (GPa/m)	1.3	1.5
K_s (GPa/m)	0.65	0.75
Friction angle (°)	15	15

3.2.3 Simulation procedures and monitoring points

A gravitational force was applied to the model while maintaining the normal displacement on the lateral and bottom boundaries zero. The elements under the working face were then removed from the model in a stepwise manner to represent the excavation. The height of each excavation is 20 m. The excavation-induced displacement was recorded to calculate the change in distance monitored by the APS and GPS.

3.3 Simulation results

In this subsection, the results of relationship among the excavation level, geological condition, and mining activities are displayed. In addition, we use the same data processing method as the field monitoring to compare the simulation results with the observed data of APS, GPS, and crack gage shown in Section 2.5.

3.3.1 Displacement increment vector

As mentioned in Section 2.5, change in distance decrease rapidly after the excavation level passes the VZ level. To understand the relationship between the excavation level and the mining-induced displacement, the displacement increment vectors before and after the excavation face passed the VZ were analyzed in three simulation models. Figs. 3.2 and 3.3 depict the vectors in the former and the latter case, respectively. Despite the different properties of rock mass, as indicated in Fig. 3.2, the upward displacement was common in the three section models before excavation, whereas significant differences were observed after the excavation face passed the VZ (Fig. 3.3). In the case of section A-A', the rock slope on the right-hand side of the VZ indicated sliding movement in the forward and downward directions. Furthermore, the forward displacement component existed in the triangular zone adjacent to the VZ (Fig.2.13). In section B-B' and C-C', the rock slope behavior remained unchanged while exhibiting upward movement in all groups, although the displacements on the right-hand side of the VZ were extremely small.

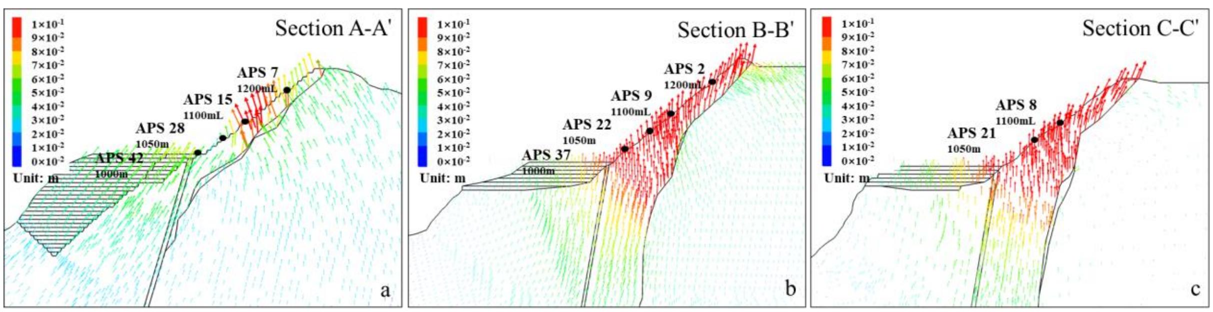

Fig.3.2: Displacement vectors of each section model, before the excavation face passes the VZ, respectively.

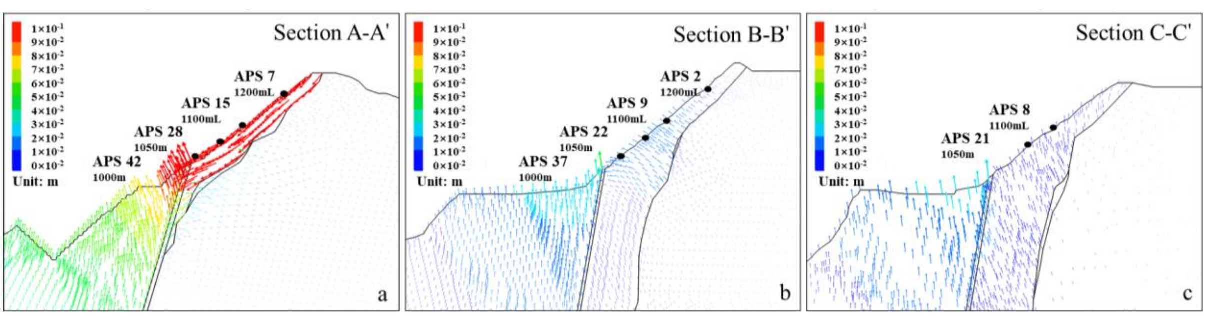

Fig.3.3: Displacement vectors of each section model, after the excavation face passes the VZ, respectively.

3.3.2 Comparison with the GPS measurement

The sliding movement occurring in section A-A' is very similar to the characteristics exhibited by the GPS-measured absolute value deformation. Therefore, we selected the heights at which GPS 7, 15, 27, 42, and 72 are located to further confirm the mining-induced deformation from 2011 to 2016. The results are plotted in Fig. 3.4, with GPS measurements on the left and simulation results on the right.

Although the section A-A' is slightly different from the section where the GPS is located, both show highly similar deformation characteristics from 2011 to 2016. On the upper sides of the VZ, all GPS points exhibit slip deformation, and the sliding gradient decreases gradually from 7 to 42. The sliding direction is nearly horizontal at GPS 42. On the other hand, on the lower side of the VZ, the triangular zone (GPS 72) shows forward and upward deformation.

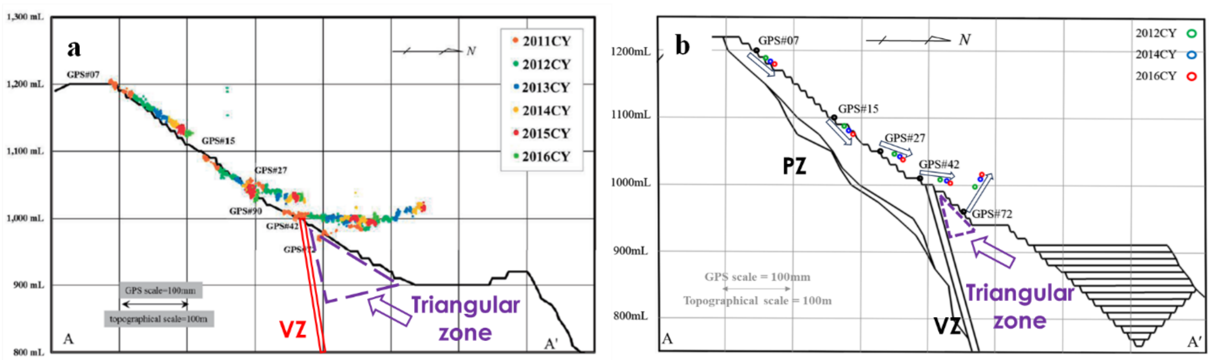

Fig.3.4: Observed GPS data (a) (Nakatani et al., 2018), and simulation result (b) of displacement from 2011 to 2016.

3.3.3 Comparison with the APS measurement

As described in Section 2.4, the changes in distance in sections A-A' and C-C' measured using APS were relative to that in section B-B'. In the numerical simulation, the relative distance change was calculated using displacements at locations corresponding to the APS mirror points for comparison between the measurements and simulation results. In the case of model A-A', the relative displacements between APS 7-2, 15-9, 28-22, and 42-37 were calculated, whereas the relative displacements between APS 8-9 and 21-22 were calculated for model C-C'. Finally, the change in the distance between each APS point and beam generator was evaluated by calculating the change in the displacement component at each point.

The open circles on the dashed line in Fig. 3.5 depict the simulation results and the solid lines indicate the measurement results. The date on the horizontal axis in the figure is estimated based on the date of each excavation stage. In the case of section C-C' (Fig. 3.5b), the calculated distance at APS 8 and 21 exhibited no apparent change, although a slight decrease and increase were observed after 2014. For section A-A' (Fig. 3.5a), the distance at APS 7 and 15 began decreasing in 2002 and the decreasing accelerated after 2006 when the excavation face passed the VZ. Subsequently, their decreasing rates gradually reduced with time. The distance at APS 28 similarly experienced a rapid decrease after 2008, then converged with APS 42. The changes in distance at all points were similar in the same year.

These characteristics concurred with those observed in the measurement results. However, the simulation results for section A-A' were smaller than the measurement results. For instance, the quantity difference between the simulation and measurement was near 70%. This difference between simulation and measurement will be discussed in section 3.4.2.

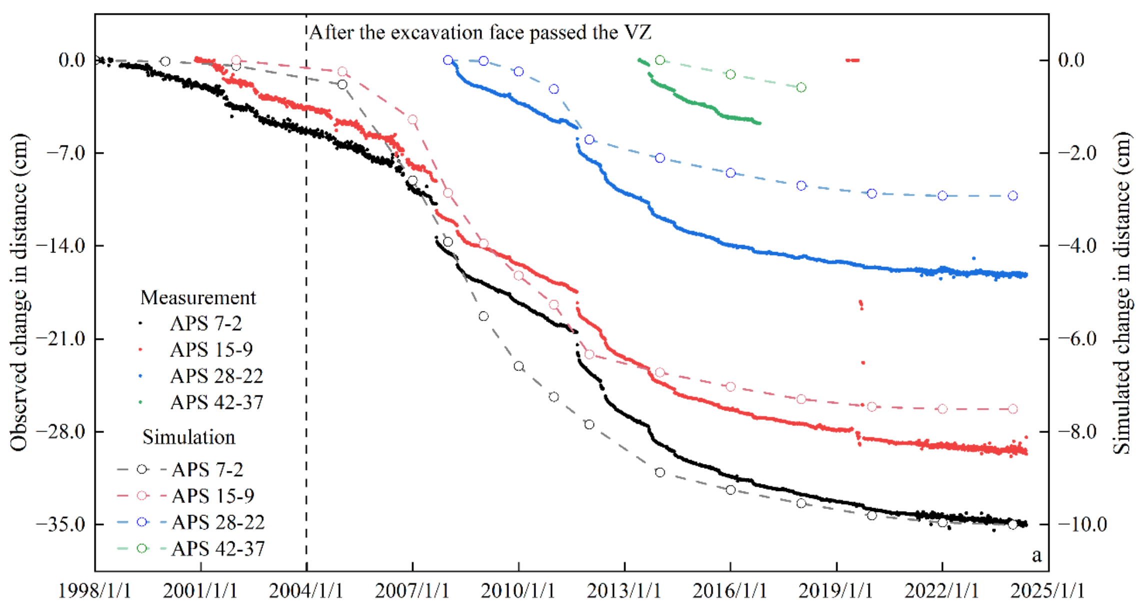

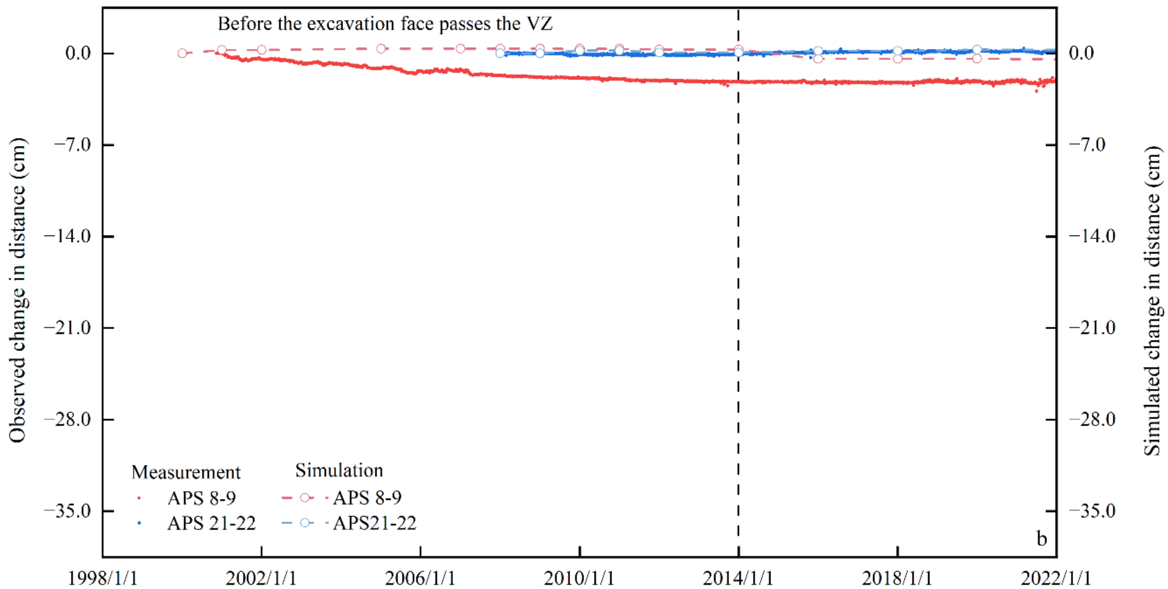

Fig.3.5: Comparison of observed data (point) on change in distance with simulation results (dot line). (a) The relative displacement in section A-A' to section B-B' (left-hand scale for measurements, right-hand scale for simulations) (b) The relative displacement in section C-C' to section B-B'.

3.3.4 Comparison with the crack gage measurement

Fig. 3.6 compared the observed shear displacement by crack gage and simulation results for No.5 low-angle crack since 2010. Attentionally, the cumulative deformation of crack No.5 in the simulation is represented as a point on the discontinuity located on the PZ very close to the actual position. It can be seen from the figure that the simulation results are qualitatively similar to the measurement results. Shear displacement continues to increase in both cases, but the rate of increase gradually decreases. However, the following same problem with the change in distance is found. The different between the simulation results and the observations was about 75%.

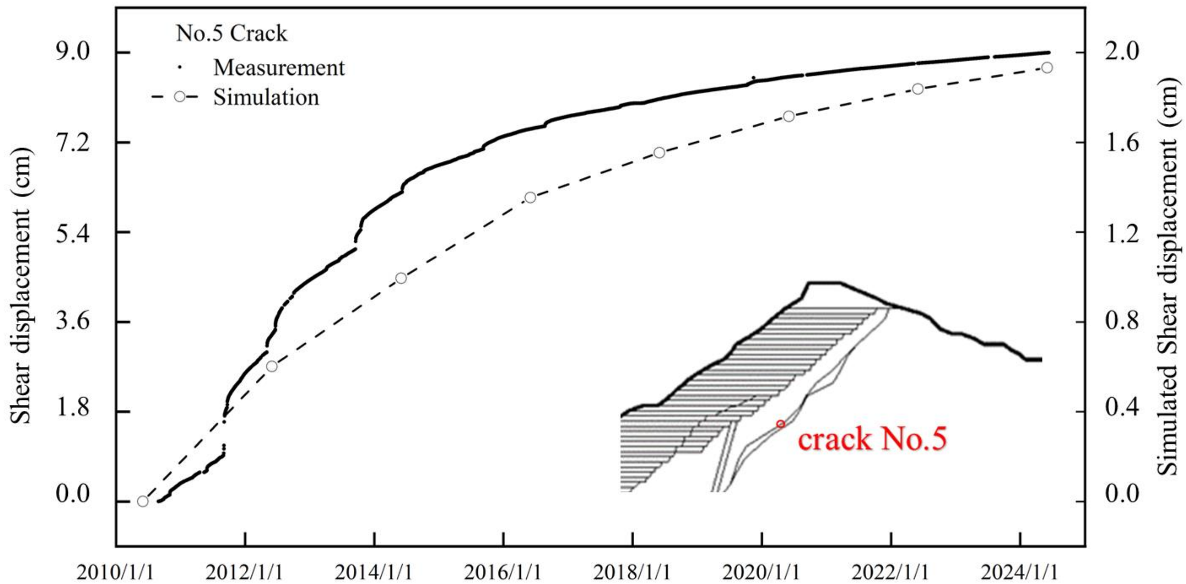

Fig.3.6: Cumulative shear displacements of low angle crack No 5. Solid line and black open circles represent monitoring data and simulation results, respectively.

Next, we examine the relationship between the cumulative shear displacement of the discontinuities at No.5 and the change in distance of APS7. The relationship is depicted as red open circles in Fig. 3.7. The cumulative shear displacement normalized by the maximum value of the calculated change in distance of APS7. The same relationship on measurement results is also shown in the figure for comparison. As seen in the figure, the relationship on simulation results is good agreement with that on measurement results. Shear displacement at No.5 has a linear correlation with the surface displacement at APS7. It can be seen from the figure that the ratio of displacements at No.5 and APS7 in the simulation results is almost equal to those in the measurement results. The ratios for measurement and simulation results are approximately 60% and 65%, respectively. These results indicate that the simulation model aligns well with the measurements, confirming that the observed deformation on the slope surface is highly dependent on sliding movements along the PZ. The reason why the displacement at APS7 is greater than that at No.5 remains unclear. Shear deformation of the cover rock might cause the difference in displacement between APS7 and No.5. The surface displacement on the cover rock is expected to be greater than its inner displacement if the cover rock shows shear deformation.

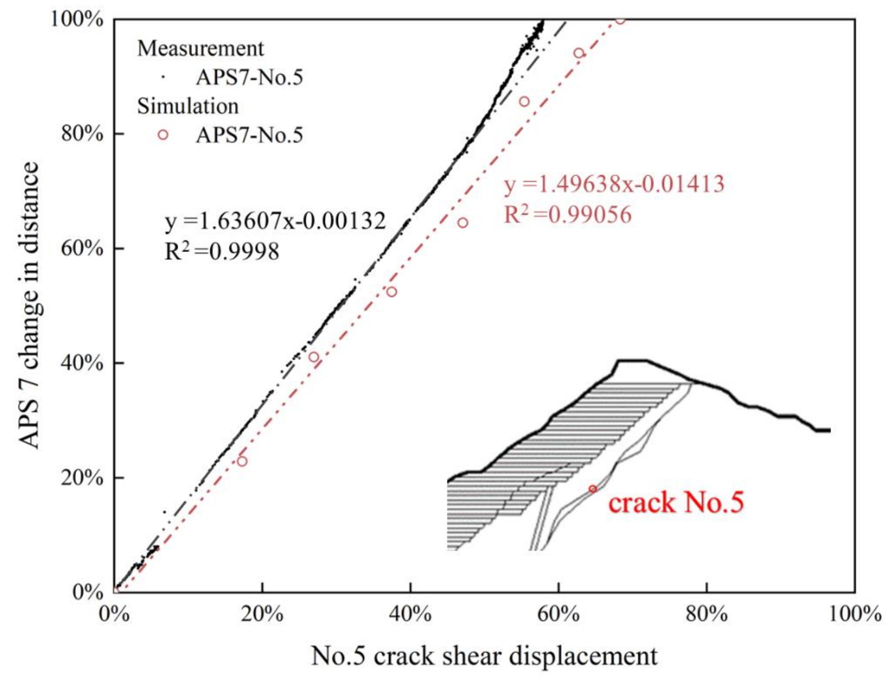

Fig.3.7: Relationship between displacement obtained from APS7 and crack No.5. Black dots represent monitoring data, red open circles represent simulation results.

3.4 Discussion

In the above results, the simulation demonstrates qualitative similarity with the observations. Therefore, it is reasonable to use this model to analyze the deformation mechanisms. However, there is a quantitative discrepancy between the simulation and measurement results. For ensuring accurate stability assessments of the rock slope, it is necessary to identify the causes of this discrepancy. In this section, we first examine the deformation mechanisms using the A-A' section model. Next, we investigate the causes of the quantitative differences between the measurement and simulation results. Finally, we evaluate the stability of the rock slope at Mt. Buko based on the deformation mechanism.

3.4.1 Mechanism of sliding movement

In the previous analysis we noted that the slip along the PZ is an important reason for the increase in the change in distance. In the results of Section 3.3, we found that the generation of this slip was also considered to be influenced by the excavation level. Therefore, change in stress state along the PZ due to excavation is analyzed.

Fig. 3.8 illustrates the change in the shear-to-normal stress ratio at Point A, B, and C, which are located on the discontinuity at the top, center, and bottom of the PZ in the section A-A'. The ratio at Point A increased, while Points B and C initially decreased in the early stages but later increased, eventually reaching 0.268, which lies on the Mohr-Coulomb failure envelope at a friction angle of 15°. The three points reached the failure envelope in the order of Point A, B, and C. After the excavation level passed the VZ level (1,000 m), the ratios at all points were 0.268, indicating that shear failure occurred sequentially along the discontinuity between the cover rock and PZ from the top of section A-A', with the entire boundary ultimately failing after the excavation face passed the VZ level.

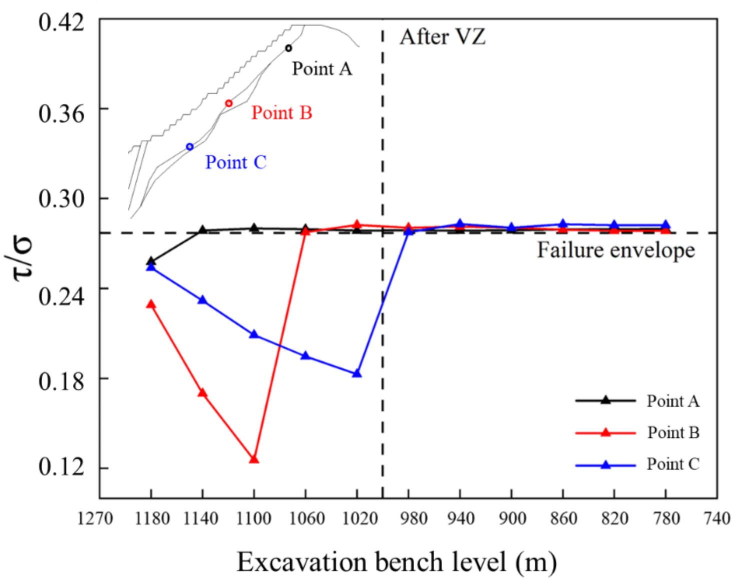

Fig.3.8: The ratio of shear stress and normal stress change during the excavation stage in the parallel weak rock zone. (The dot line in horizontal direction represents the Mohr Coulomb failure envelope at Φ=15°, cohesion=0 MPa).

Fig. 3.9 depicts the normal stress at Point #1 and #2 on the discontinuity on the right-hand side of the VZ, located 20 m and 40 m below the working bench in three sections, with negative values indicating compression. In section A-A', the normal stress increased gradually with the excavation progress. However, very little change in normal stress was observed in section B-B' and C-C'.

The gradual increase in joint normal stress before the excavation passes the VZ level corresponds well with the propagation of shear failure in the discontinuities of the PZ. The increase in normal stress in section A-A' indicated that the VZ on the upper side was gradually compressed by the cover rock sliding along the PZ. Under the effect of the compression, it is reasonable to speculate that the forward displacement component in the triangular zone adjacent to the VZ in Fig. 3.3a is induced by compression.

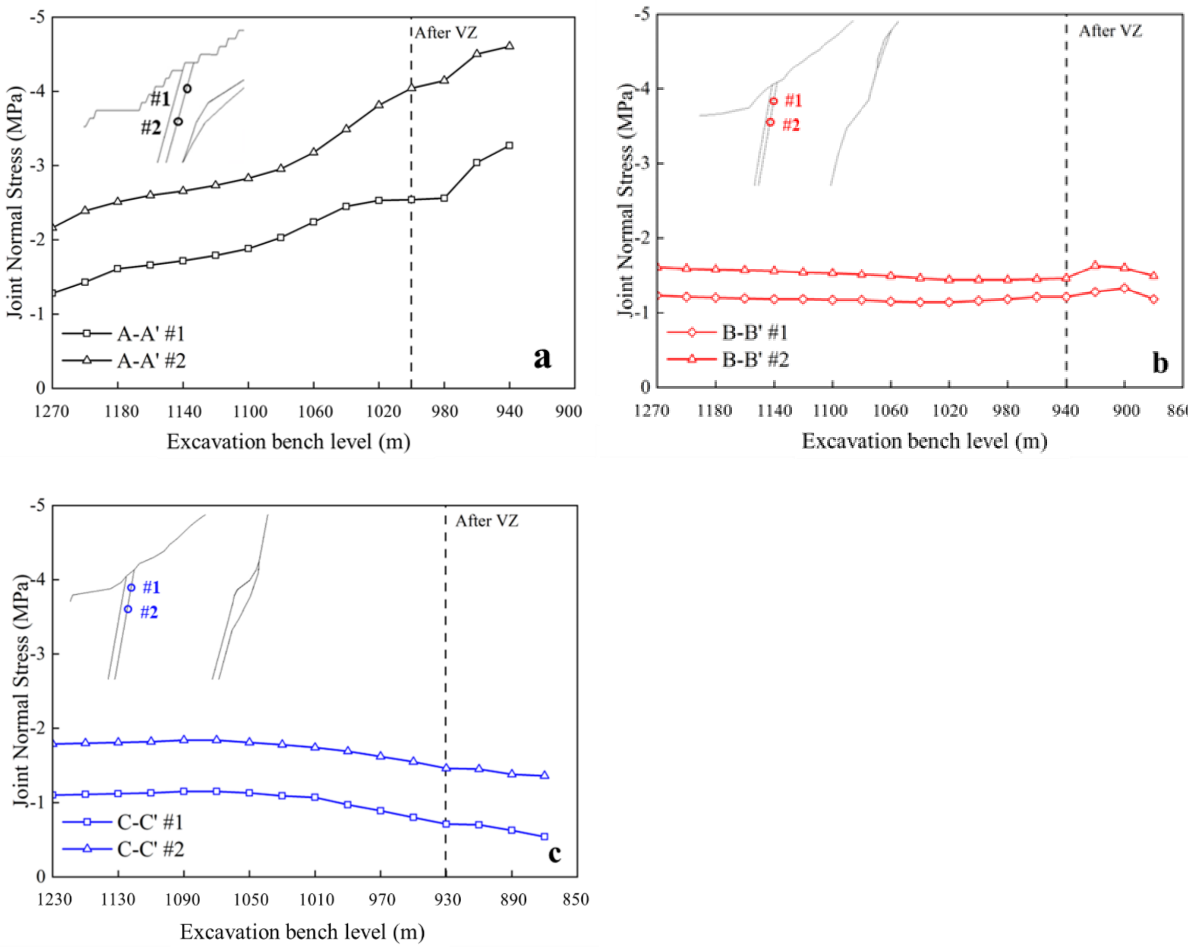

Fig.3.9: The normal stress variation at the points on the right side of the VZ discontinuity during the excavation stage in section models. (a) section A-A'. (b) section B-B'. (c) section C-C'.

Next, as indicated in Fig. 3.10, impacts of compression behind the VZ were examined by analyzing the minimum principal stress (the maximum tensile stress) in the forward zone of the VZ after the excavation face passed the VZ. Positive values in the vertical axis in Fig. 3.10 represent tension. Large tensile stresses are distributed in the forward zone adjacent to the VZ in the A-A' section, along the VZ direction, while sections B-B' and C-C' remain under compression. The tensile stress increased after the excavation face passed the VZ (1,000 m), showing a rapid increase in tensile stress during the stage of joint normal stress increase. Hence, it is believed that under the "push" of the upper cover rock, the forward zone shows bending deformation.

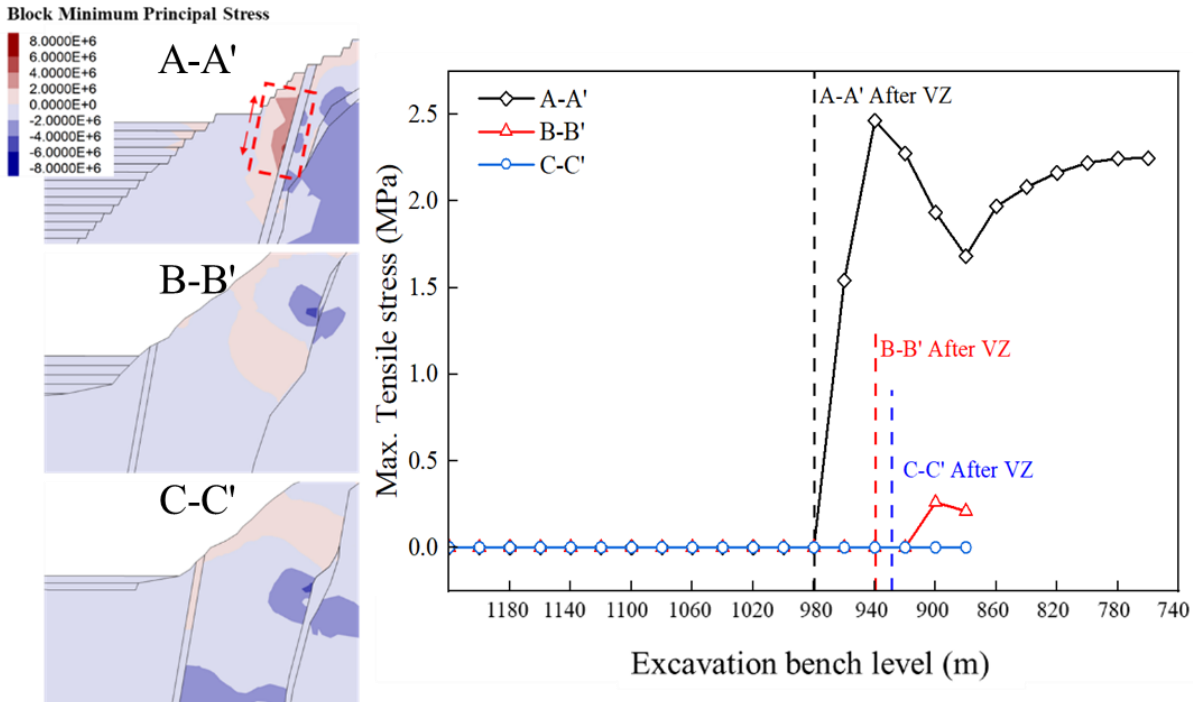

Fig.3.10: The Maximum tensile stress variation in the forward zone of the VZ during the excavation stage in three section models.

Based on the aforementioned considerations, we propose the following mechanism of slip movement in the section A-A' (Fig. 3.11). The normal and shear stresses on the discontinuity of the PZ decrease with excavation, and the decrease in the normal stress is greater than that of the shear stress, which increases the shear-to-normal stress ratio (Fig. 3.8). This change in stress induces shear failure of discontinuity, which develops from the top of the rock slope and gradually expands (Fig. 3.11a and 3.11b). After the excavation face passes the VZ, shear failure extends to lower part of the discontinuity in the PZ. The development of shear failure further induces an increase in the contraction of the VZ because the cover rock pushes the VZ from behind, enabling the sliding movement of the cover rock along the PZ. Subsequently, the triangular zone beside the VZ undergoes a bending load owing to the large thrust force applied by the cover rock, resulting in elastic deformation and escalation of the cover rock sliding (Fig. 3.11c). Eventually, the slip movement terminates when the elastic resistance force caused by the bending deformation of the VZ and triangular zone becomes equal to the sliding force of the cover rock.

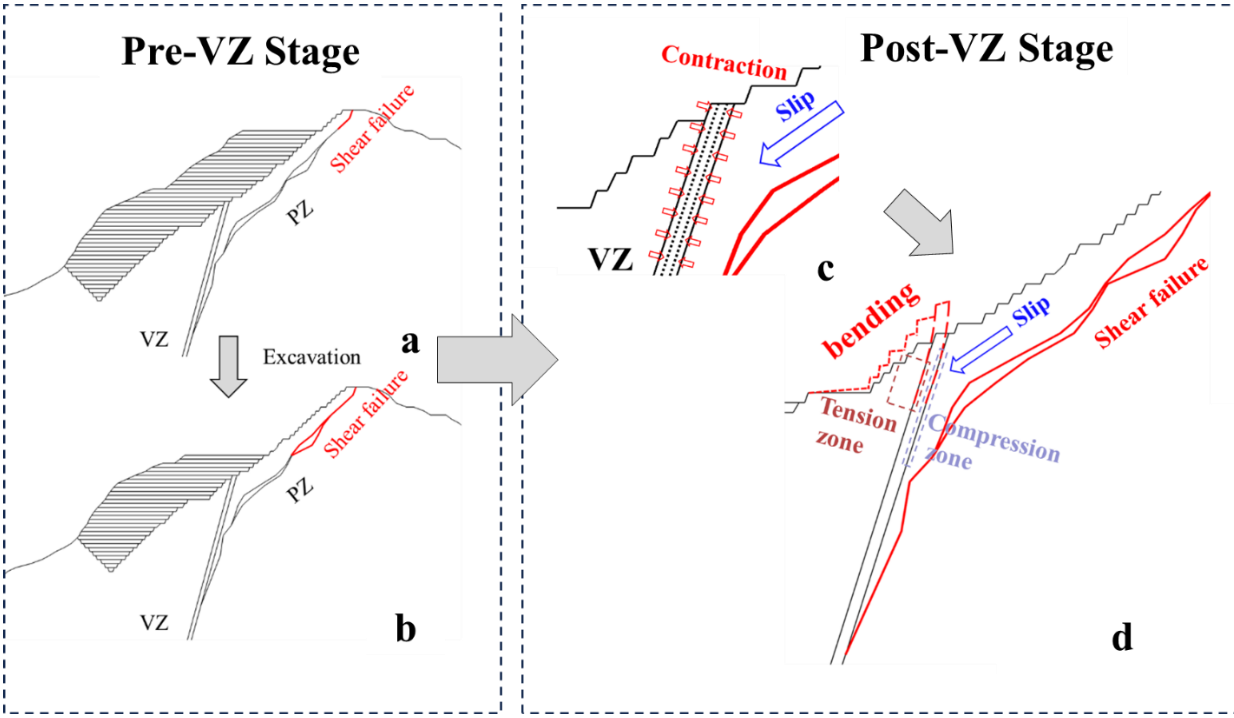

Fig.3.11: Slip generation process based on section models.

To verify the slip mechanism described above, specifically whether sliding movement occurs only when two weak rock zones are present and connected, we created three additional models: one without weak rock zones (Fig. 3.12a), one with a vertical weak rock zone only (Fig. 3.12b), and one with a parallel weak rock zone only (Fig. 3.12c). The parameter selection and simulation process for all models were identical to those used for the A-A' section model. The results shown in Fig. 3.12 indicate that no slip deformation occurs in any of these three scenarios. When combined with the simulation results of sections B-B' and C-C' (Figs. 3.2 and 3.3), these findings confirm that slip deformation occurs only when two weak rock zones are connected.

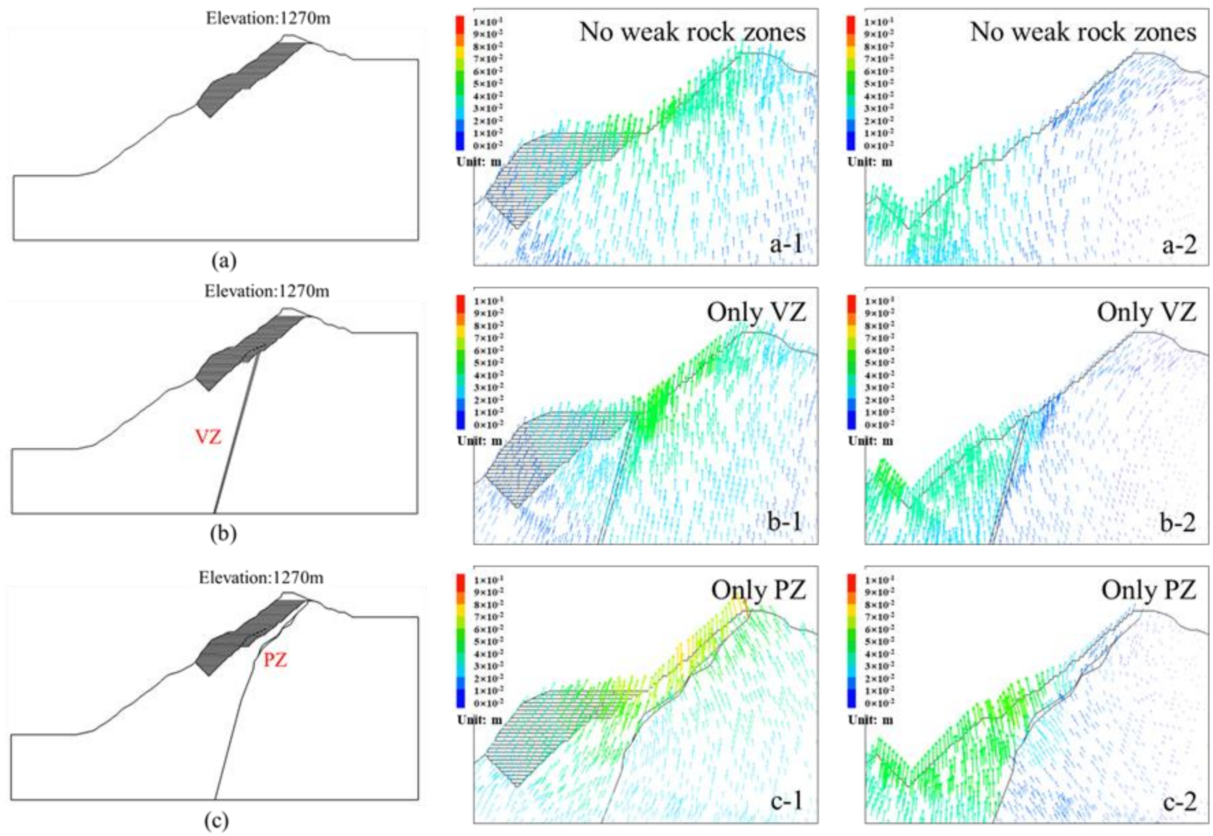

Fig.3.12: Displacement vectors of changing the combinations of weak rock zones. (a) No weak rock zones (b) Only Vertical weak rock zone (c) Only Parallel weak rock zone, 1 and 2 represent before and after excavation level passes the VZ level, respectively.

3.4.2 Difference in measurement and simulation

As mentioned in Section 3.3, there are notable differences between the measurement and simulation results. Although the simulation model captures the deformation characteristics, the difference in change in distance between measurements and simulations were near 70%. Sliding of the low-angle crack (No.1 and 3) in the cover rock could result in a decrease in change in distance (Aoyama et al., 2018). Overestimation and underestimation of mechanical properties used in the simulation could be also causes for the differences. In this subsection, effects of elastic properties of rock mass and discontinuities will be considered.

3.4.2.1 Effect of the elastic properties of rock mass

One of possible reasons for this discrepancy is the weathering condition of the rock mass. As seen in Fig. 2.4, numerous joints and cracks are present in both the limestone and green rock.

Combined with frequent rainfall in the mine area, these conditions contribute to the weathering of the rock mass (Erguler et al., 2009). Additionally, clay is distributed in parallel weak rock zones and the vertical weak rock zones. Generally, Young's modulus decreases as the clay content increases because clay typically has a Young's modulus of less than 250 MPa (Kulhawy et al., 1990).

To assess the impact of weathering and clay content on sliding movements, the influence of changes in Young's modulus across different rock masses was analyzed. The Young's modulus for each rock type was reduced to 75% and 50% of its original value after the initial stress field was equilibrated. The reduced Young's modulus values are summarized in Table 3.6.

Table 3.6: Reduced Young's modulus in each part of rock mass.

Properties	Limestone	Green rock	Vertical weak rock zone	Parallel weak rock zone
100%	20.0GPa	15.0GPa	1.5GPa	1.3GPa
75%	15.0GPa	11.0GPa	1.1GPa	1.0GPa
50%	10.0GPa	7.5GPa	0.7GPa	0.6GPa

Fig. 3.13 illustrates the changes in the distance of APS 7-2 for various elastic moduli in different rock masses. The results indicate that reducing the Young's modulus of green rock and the parallel weak rock zone has little impact on sliding movement, with only minor variations in the changes in distance. Conversely, reducing the Young's modulus of the limestone and the vertical weak rock zone significantly increases sliding movement. When the Young's modulus of both was reduced to half of its original value, the calculated change in distance increased to 40% of the observed data.

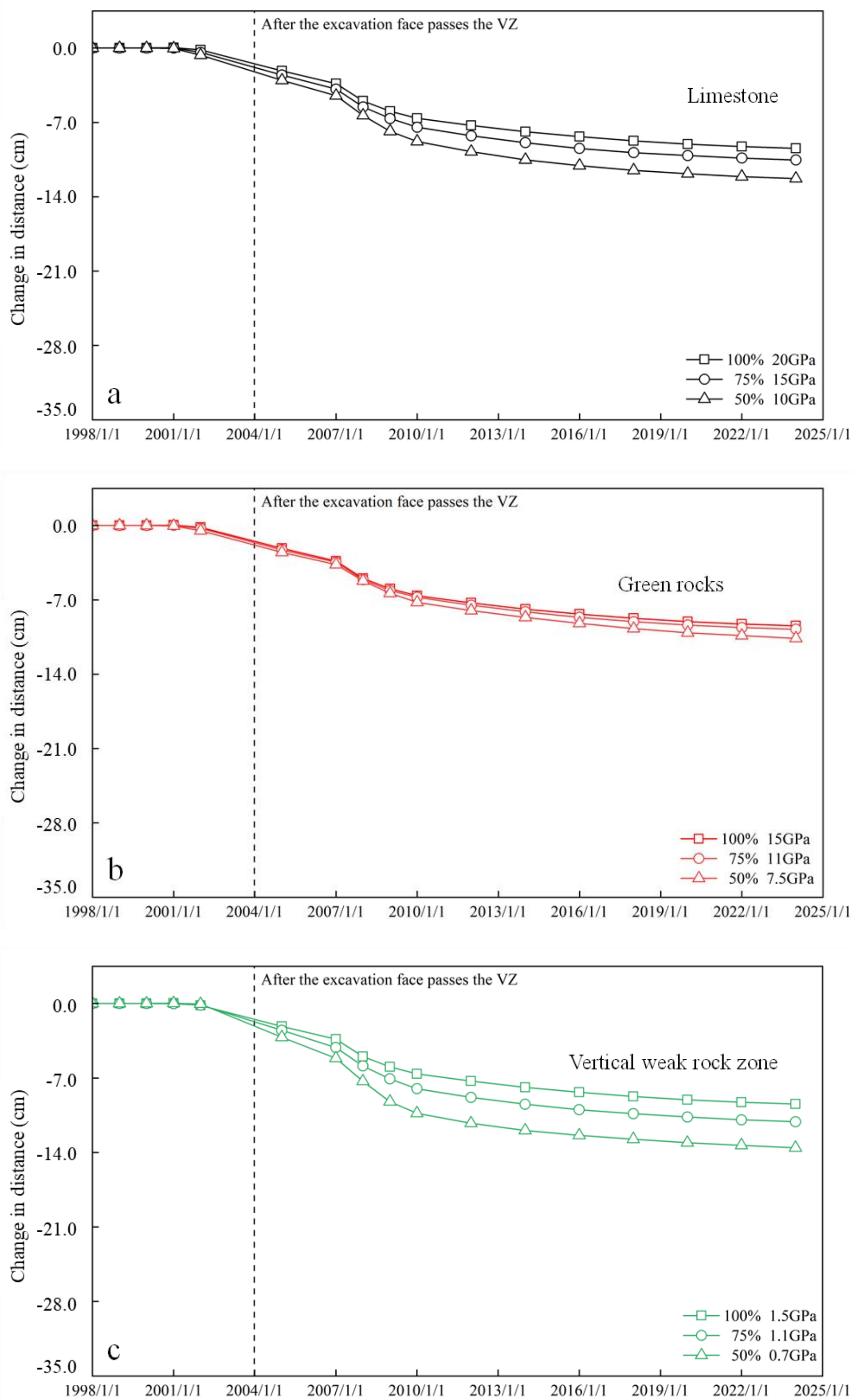
After the excavation face passes the VZ
Limestone
Change in distance (cm)
0.0
-7.0
-14.0
-21.0
-28.0
-35.0
100% 20GPa
75% 15GPa
50% 10GPa
a
1998/1/1
2001/1/1
2004/1/1
2007/1/1
2010/1/1
2013/1/1
2016/1/1
2019/1/1
2022/1/1
2025/1/1
After the excavation face passes the VZ
Green rocks
Change in distance (cm)
100% 15GPa
75% 11GPa
50% 7.5GPa
b
After the excavation face passes the VZ
Vertical weak rock zone
Change in distance (cm)
100% 1.5GPa
75% 1.1GPa
50% 0.7GPa
c

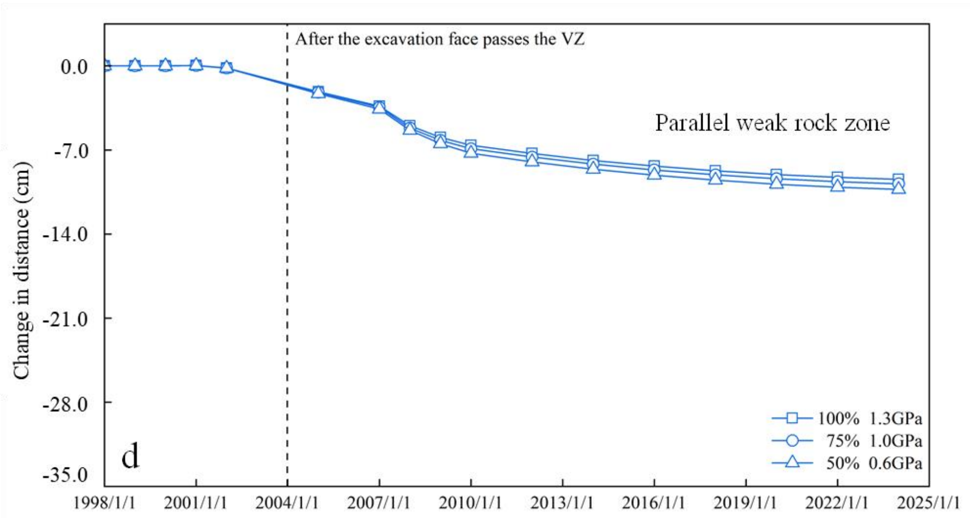

Fig.3.13: Effect of the Young's modulus of each part of rock mass on change in distance. (a) Limestone (b) Green rock (c) Vertical weak rock zone (d) Parallel weak rock zone.

Moreover, the effect of Poisson's ratio of rock mass has also been further explored. As shown in Fig. 3.14, the results of change in distance at APS 7-2 at Poisson's ratio of 0.2, 0.25, and 0.3 are compared. The results show that although a decrease in Poisson's ratio leads to a slight decrease in the change in distance, the effect is almost negligible.

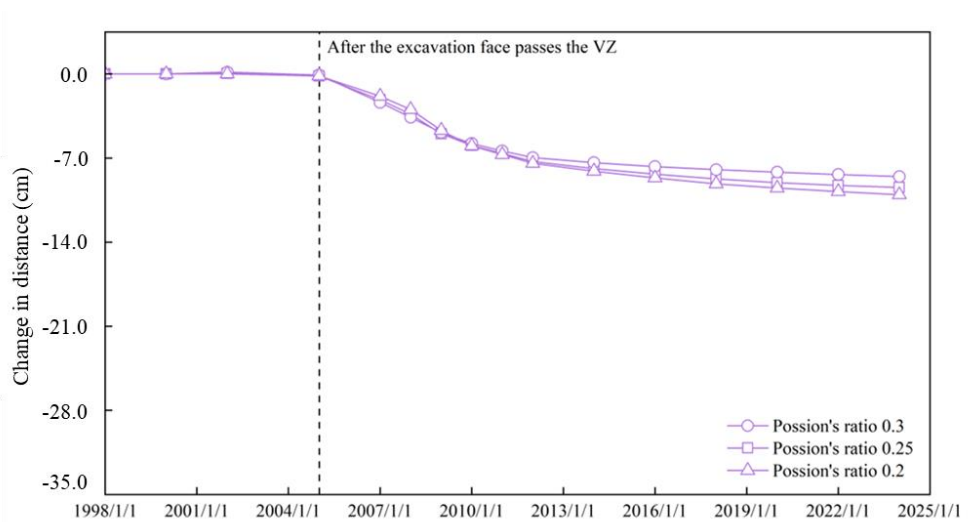

Fig.3.14: Effect of changes in Poisson's ratio on change in distance.

3.4.2.2 Effect of the discontinuity properties

Similar to the approach in subsection 3.4.2.1, we reduced the friction angle and contact stiffness of the discontinuities to investigate their effects on changes in distance. The friction angle in the original simulation model is 15°, such a small value itself already included the effect of rainfall on discontinuities. In addition, although contact stiffness parameters K_n and K_s can be measured at the laboratory scale, determining their values for large-scale natural conditions is challenging. The friction angle and contact stiffness properties were reduced to 75% and 50% of their original values. The corresponding values of reduced contact stiffness are summarized in Table 3.7.

Fig. 3.15 presents the calculated changes in distance at APS 7-2 after modifying the discontinuity properties. The friction angle significantly affects the change in distance, even showing a further decrease during the stage of initial convergence, which does not align with observations. In contrast, the contact stiffness shows negligible impact on the change in distance.

Table 3.7: Reduced contact stiffness of discontinuities.

Properties		Vertical weak rock zone – rock mass contact	Parallel weak rock zone – rock mass contact
100%	K_n (GPa/m)	1.5	1.3
	K_s (GPa/m)	0.75	0.65
75%	K_n	1.1	1.0
	K_s	0.65	0.5
50%	K_n	0.75	0.65
	K_s	0.38	0.33

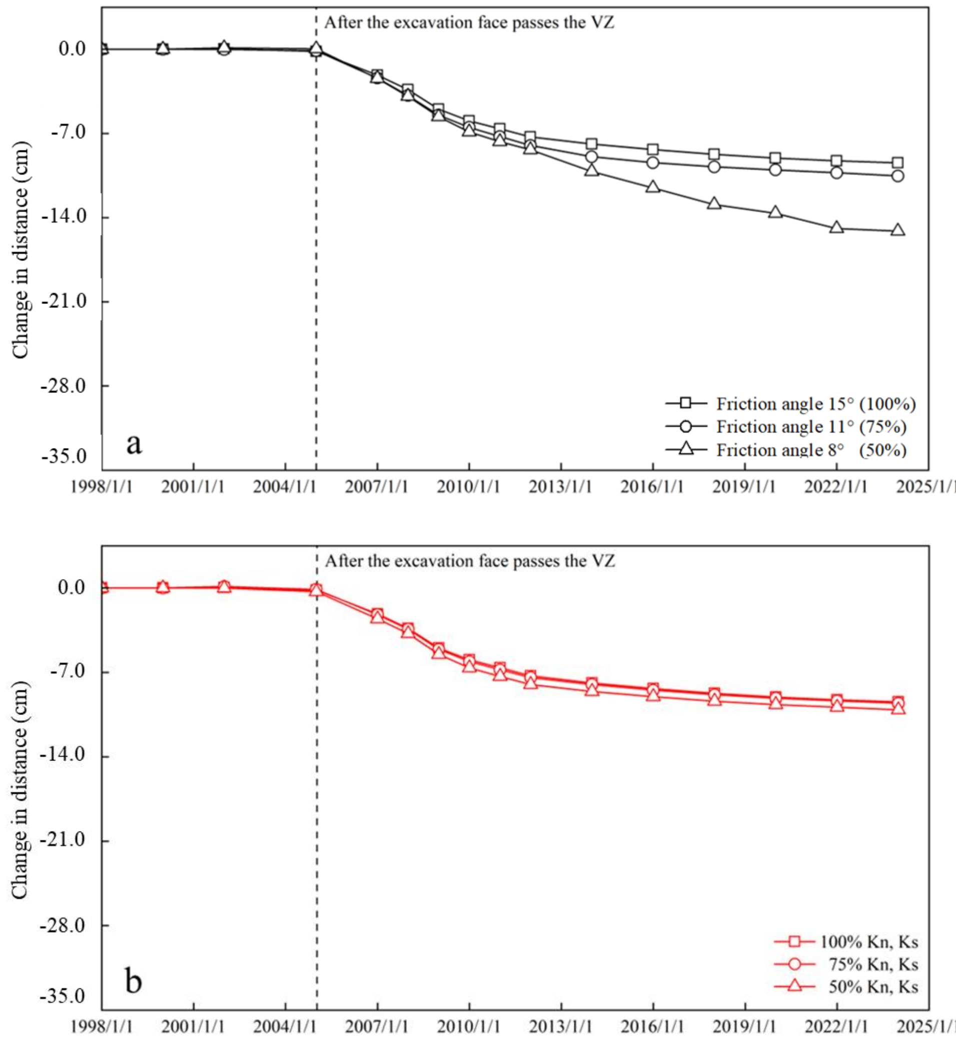

Fig.3.15: Effect of the discontinuity properties on change in distance. (a) Friction. (b) Contact stiffness.

3.4.3 Stability assessment of the rock slope at Mt. Buko

On the east side of Mt. Buko, the section B-B' and C-C' exhibited upward displacement during excavation progress. The cover rock between the limestone and green rock did not undergo sliding because the two weak rock zones were unconnected and did not mechanically interact with each other. The deformation occurred at both sections can be interpreted as elastic deformation caused by the release of gravity-induced elastic strain owing to excavation, indicating that the rock slope in section B-B' and C-C' remained stable.

On the west side, section A-A' experienced long-term slip deformation along the discontinuity of the PZ. However, the results demonstrated that the rock slope remains stable as long as the rock mass in the triangular zone stays in the elastic stage. Additionally, the friction angle was set at a lower value of 15° in the models to account for rainfall effects. Further slip deformation is not expected during future excavations due to the adequate implementation of drainage countermeasures in the PZ described in 2.3.

3.5 Concluding remarks

In this chapter, the observed deformation was successfully explained by 2D numerical models incorporating two weak rock zones observed in Mt. Buko. The main conclusions are follows:

1. Both the measurement and simulation results show the slip deformation only occurred when two weak rock zones are connective. The deformation is highly correlation to the distribution of the weak rock zones and excavation states.

2. Based on the simulation results, on the west side, mining changes the stress state, causing shear failure at the boundary between the parallel weak rock zone and the limestone cover rock. As the excavation level passes the vertical weak rock zone, the bending stiffness of the triangular zone decreases, leading to sliding movement of the cover rock along the parallel weak rock zone. Moreover, As the sliding movement progresses, the resistance to bending deformation at the triangular zone increases. When this resistance balances the sliding force, the movement tends to converge.

3. Mt. Buko is expected to remain stable during future excavations. The east side showed no significant deformation, while the west side experienced slip deformation that eventually stabilized due to the resistance provided by the triangular zone.

4. One reason for the discrepancy between the simulation and the measurement is considered to be the selection of rock mass properties. With a lower Young’s modulus of vertical weak rock zone and limestone in cover rock, the model shows greater sliding deformation, which aligns more closely with the field.

4. Verification of effectiveness of stone wall countermeasure at Mt. Buko

4.1 Introduction

As described in section 2.5, the cumulative deformation of the slope surface along the A-A' section at Mt. Buko had shown rapid increase until 2012 with the stepwise increments. To enhance the stability of the slope and control the continuous slip deformation, a stone wall scheme was designed and implemented in the west side of the rock slope including section A-A' (Fig. 4.1a).

In the initial plan, the stone wall was designed in two parts, as shown in Fig. 4.1c: stone wall I, ranging from an elevation of 940 m to 1,000 m, and stone wall II, ranging from 1,000 m to 1,050 m. The stone wall I, with an average inclination of 70°, was expected to consume 1,600 kilotons of limestone, while stone wall II, with an average inclination of 30°, was expected to consume 800 kilotons of limestone. However, due to economic and other constraints, only stone wall I has been completed to date, with construction occurring from 2013 to 2016.

Research on stone walls as countermeasures for rock slope stability has historically focused on two main areas. The first area investigates the structural strength of stone wall and their failure modeling (Buhan et al., 1997; Hendry et al., 1998; Milani et al., 2006; Fan et al., 2010; Cominelli et al., 2016; Ponte et al., 2023). Hendry et al. (1998) pioneered a method to evaluate stone wall strength by treating the stone wall and slope as an integrated system, determining failure when the design strength is exceeded by the design load. Milani et al. (2006) expanded this model to incorporate the effects of discontinuities at the stone wall-slope interface and contact surface failure. Later studies, such as Cominelli et al. (2016), advanced the understanding of stone wall damage by including the effects of confining pressure using a scaled stone wall model. Ponte et al. (2023) further refined these models by considering the internal particle structure of the stone wall and the interlocking of stones, enriching the calculations of stone wall strength.

The second area examines the role of stone wall in enhancing slope stability through various analytical approaches (Akin, 2012; Ma and Lee, 2018; Paul et al., 2018; Wang et al., 2021). Two mainstream methods are commonly employed. The first is the limit equilibrium method (LEM), which treats the stone wall as part of the slope and calculates the factor of safety with or without the conditioned slope. However, LEM is highly sensitive to the accuracy of physical property parameters, and incorrect assignments can lead to vastly different results. The second approach is the strength reduction method (SRM), which evaluates the failure condition of the stone wall under tension or shear by progressively reducing the slope's strength parameters until failure occurs. These methods have provided complementary insights into the role of stone wall in slope reinforcement while highlighting challenges in parameter selection and model complexity.

The above approaches offer valuable references for evaluating stone wall effectiveness. However, in the case of Mt. Buko, the deformation of the overall rock slope is still considered to be in the elastic phase, and excavation activities are ongoing. How the stone wall influences long-term mining-induced deformation during excavation and its role in restraining slip displacement are not clear. Additionally, the dimensions of the stone wall, which involve economic, environmental, and practical considerations, should be carefully examined and optimized.

This chapter aims to evaluate the effectiveness and mechanism in restraining slip deformation by the stone wall using numerical modeling. Additionally, as excavation activities continue and slope surface deformation persists, this study will explore optimal dimension of the stone wall to ensure long-term stability.

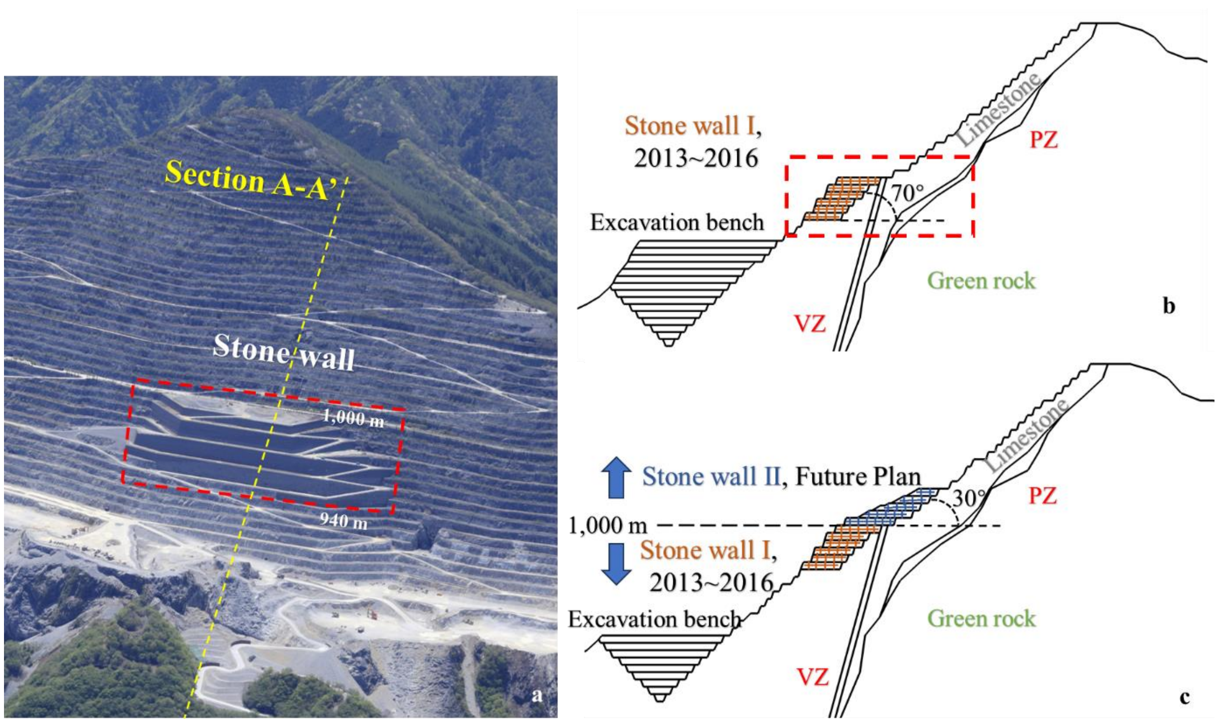

Fig.4.1: The Stone wall in Mt. Buko: (a) Location of the stone wall (b) section model of current stone wall (c) section model of planning stone wall.

4.2 Simulation method

4.2.1 Numerical models for stone wall

As outlined in Section 4.1, two stone walls, differing in construction years and heights, were modeled separately for analysis. Fig. 4.1b represents the current stone wall (stone wall I) at its current height in the quarry, positioned just below the vertical weak rock zone. For simplification, the entire stone wall elements were added to the numerical model when bench level in the A-A' section was reached to 920 m. Fig. 4.1c depicts the planning stone wall (stone wall II). The numerical model integrates the second-phase stone wall when at bench level in the A-A' section to 860 m.

The optimal dimensions of planning stone wall (stone wall II) are also examined by varying the width and height of the planning stone wall, considering it still under construction. As shown in Fig. 4.2, the width of stone II is changed to the 1/2 and 3/4 of the original width (Fig 4.2a). height of stone wall II is increased to 1,100 m (Fig 4.2b).

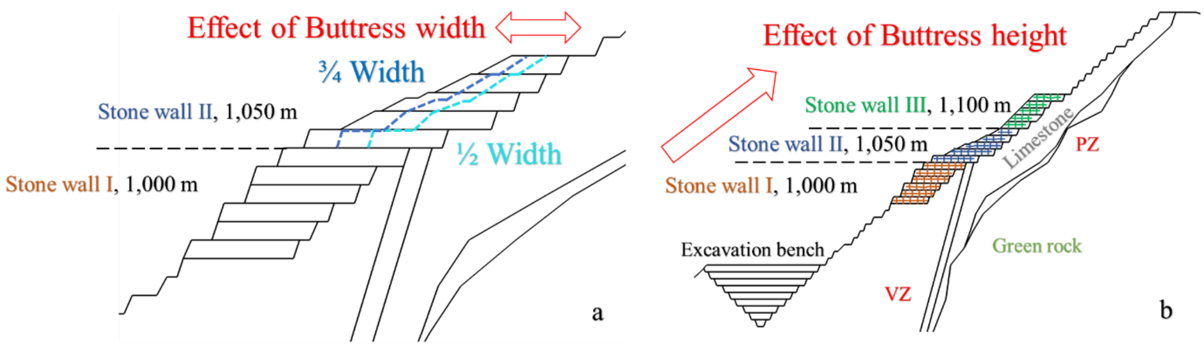

Fig.4.2: Simulation models of changing the width (a) and height (b) of stone wall II.

4.2.2 Model parameters

The stone wall was constructed using a gabion structure, with the primary aggregate being limestone from the quarry. The fill material had a particle size of approximately 10 cm to 30 cm, and the interior was grouted, resulting in an overall structure that could be approximated as a concrete structure. For simplicity, the stone wall model is treated as an elastic material.

Parametric test data for the stone wall are provided in Table 4.1. The overall Young's modulus is estimated using Equation 4.1 (Wang et al., 2008) while uniaxial compression strength was obtained from laboratory tests. Poisson's ratio of the stone wall is assumed to be same as that of the limestone as stone wall consists of blasted limestone blocks. The parameters of the stone wall models are summarized in Table 4.2.

$$E = 4700(f_c')^{0.5} \quad (4.1)$$

where f_c' is the uniaxial compressive strength of the concrete in MPa.

Table 4.1: Properties of the stone wall in the quarry by experiment.

Density (kg m^{-3})	2100
UCS (MPa)	3.8

Table 4.2: Elastic properties of the stone wall in the simulation models.

Density (kg m^{-3})	2100
Young’s modulus (GPa)	10
Poisson’s ratio	0.25

The contact interfaces between stone wall blocks, as well as between the stone wall blocks and the rock slope, are modeled as discontinuity elements. These interfaces, as illustrated in Fig. 4.3, are governed by the Mohr-Coulomb criterion, which accommodates separation and slip motion. The normal (K_n), shear (K_s) contact stiffness and friction angle are derived from concrete artificial structures and are approximated based on the Young's modulus of the stone wall (Fan et al., 2010). For both parameters, a value of 10 GPa/m is used. Table 4.3 provides a summary of the selected contact parameter values.

Table 4.3: Mechanical properties of stone wall contact.

Properties	Stone wall block–stone wall block contact	Stone wall block – rock mass contact
K_n (GPa/m)	10	10
K_s (GPa/m)	10	10
Friction angle (°)	30	30

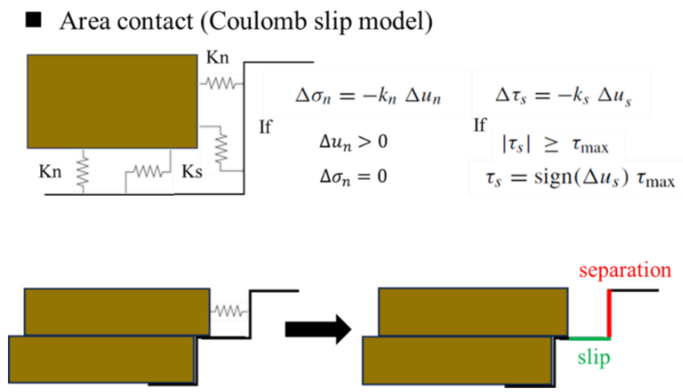

Fig.4.3: Contact model of the stone wall in section models.

4.2.3 Simulation procedures and monitoring points

Elements for stone wall was incorporated in the model shown in Fig.3.1 for analysis on section A-A' (Fig.2.5(a)). The simulation involved the following five steps: (1) Displacements perpendicular to the bottom and lateral boundaries of the model were fixed at zero. (2) Initial iterations under gravity were conducted to establish the initial stress state. (3) Iterations proceeded with the removal of excavation zones, during which changes in displacement and stress were monitored throughout the initial half of the excavation process. (4) Adding stone wall elements when excavation level reaches to 920 m or 860 m, followed by iterations under gravity. (5) The simulation concluded with the completion of the second half of the excavation, recording the variations in displacement and stress.

The monitoring points are same with the Section 3.2, the slope surface points (APS points in Fig. 2.5) are used to record the cumulative displacements under excavation progress.

4.3 Simulation results

4.3.1 Effects of Stone wall height

The cumulative displacement at APS 7 and APS 15 before and after the stone walls construction are depicted in Fig. 4.4. X and Y displacements are displacements in horizontal and vertical directions, respectively, as shown in Fig. 3.1. It can be seen that constructing stone wall up to 1,000 m (Stone wall I) reduce slip displacement in both the X and Y directions. However, the displacement at both points does not converge.

Corresponding to these displacement results, Fig. 4.5 shows the variations in maximum tensile stress in the triangular zone (Fig.2.13) with different stone wall heights. The presence of stone wall

I significantly reduces the maximum tensile stress there.

Compared to the scenarios with no stone wall or with stone wall of 1,000 m height (Stone wall I), slip displacement is further attenuated, nearly ceasing in both the X and Y directions when stone wall is constructed up to 1,050 m height (Stone wall II). Similarly, a significant reduction in the maximum tensile stress of stone wall II, with values not exceeding 1 MPa is shown in Fig. 4.5. Furthermore, the results indicate negligible differences in slip limitation effectiveness between 1,100 m and 1,050 m can be seen, as corroborated by the variations in the maximum tensile stress.

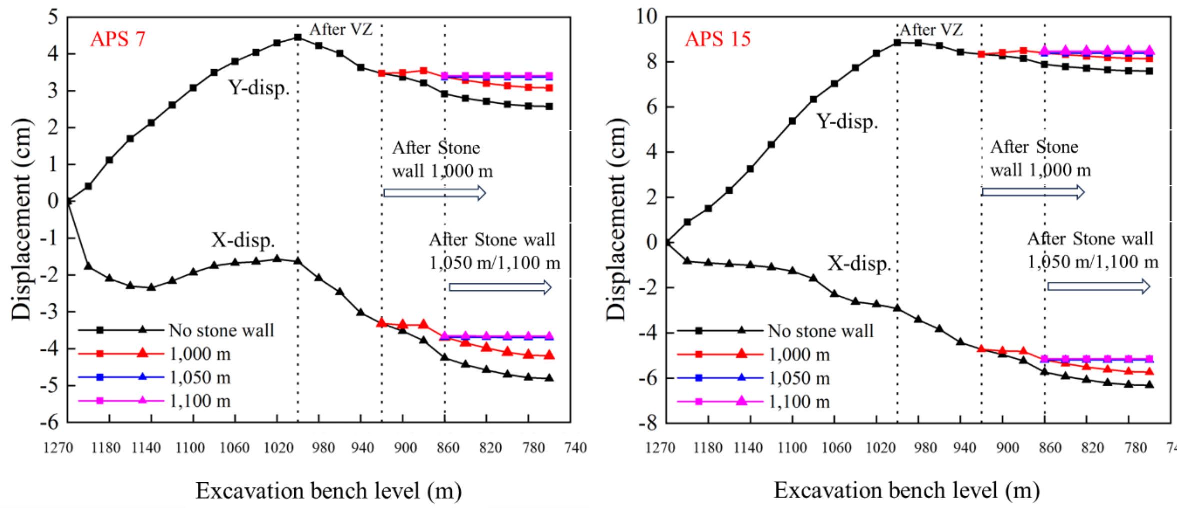

Fig.4.4: Displacement results by varying stone wall height at APS 7 and APS 15.

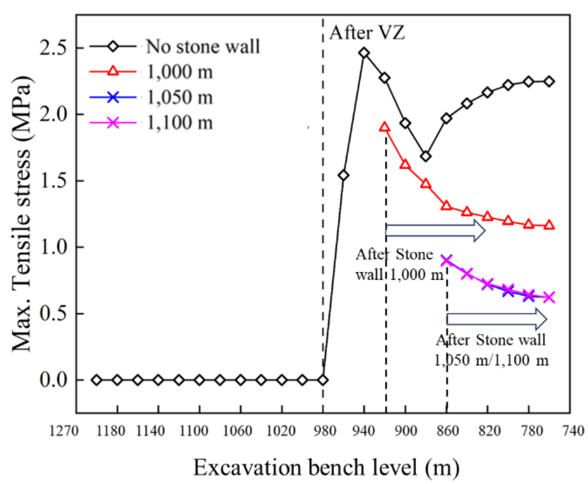

Fig.4.5: The maximum tensile stress change in triangular zone by varying stone wall height.

4.3.2 Effects of stone wall width

Fig. 4.6 shows the cumulative displacement changing the width of stone wall with 1,050 m height (Stone wall II). Slip displacement decreases progressively with increased width, and at the original design width (1.0), slip displacement is completely restrained. This trend is also observed in Fig. 4.7, which illustrates a uniform reduction in maximum tensile stress in the triangular zone as the width increases.

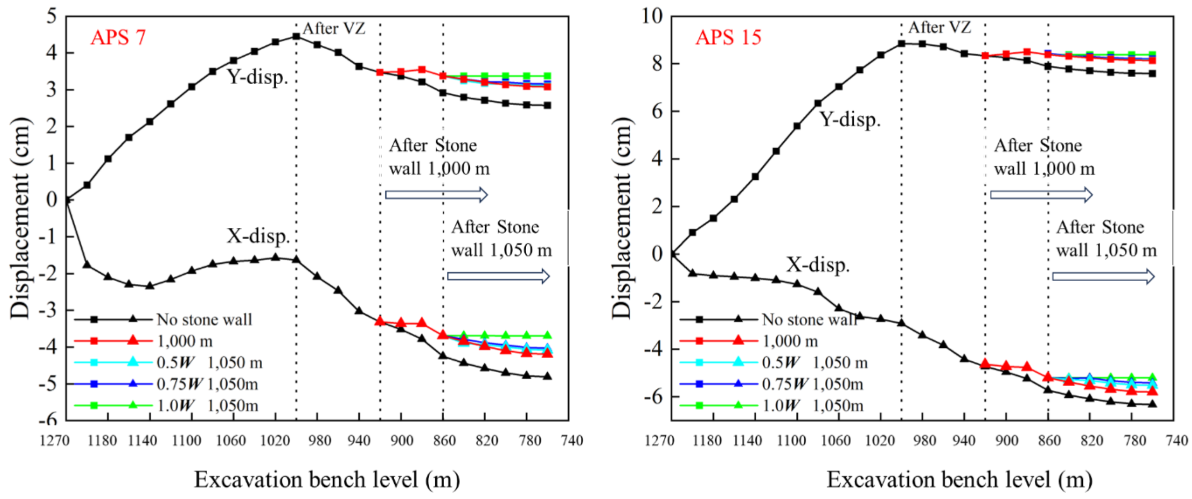

Fig.4.6: Displacement results by varying stone wall width at APS 7 and APS 15, ***W*** represents the original design width.

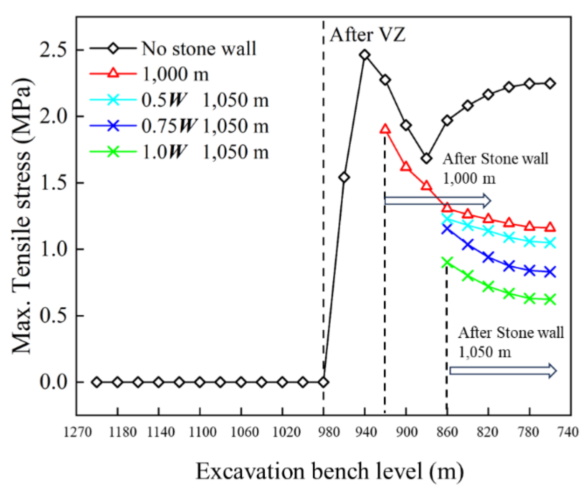

Fig.4.7: The maximum tensile stress change in triangular zone by varying stone wall width during excavation progress.

4.3.3 Effects of stone wall properties

Misestimation of stone wall material properties can lead to inaccurate assessments of their effectiveness. This subsection examines the contribution of different properties—density, Young's modulus, Poisson's ratio, and contact stiffness—for restraining slip displacement.

Figs. 4.8 and 4.9 present the cumulative displacement at APS7, 15, and maximum tensile stress variation in the triangular zone under various Young's modulus. Young’s modulus was set at less than 20 GPa which is Young’s moduli of limestone (Table 3.3). The results indicate that Young's modulus has a minimal impact on restraining slip displacement although slight change can be seen in the displacement and the maximum tensile stress with Young’s modulus.

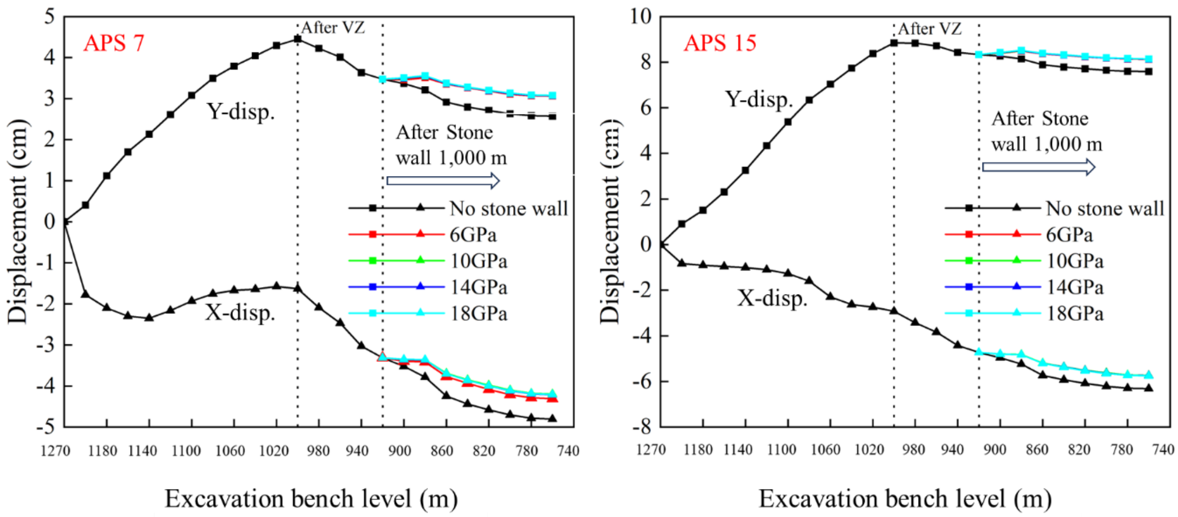

Fig.4.8: Displacement results by varying stone wall Young’s modulus at APS 7 and APS 15.

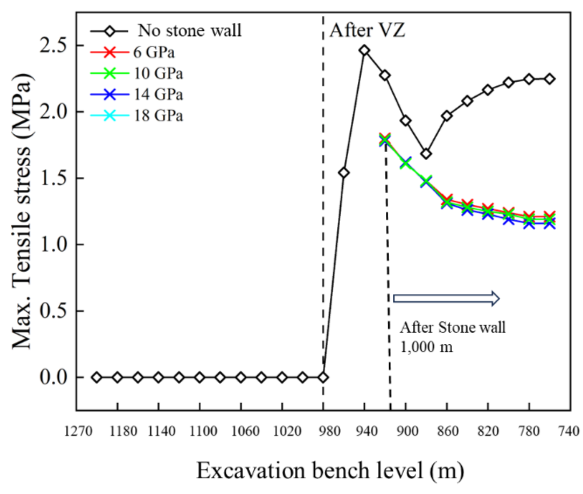

Fig.4.9: The maximum tensile stress changes in triangular zone by varying stone wall Young’s modulus.

We also examined the effect of contact stiffness between the stone walls and the rock slope. As shown in Figs. 4.10 and 4.11, the cumulative displacement at APS 7, 15, and the maximum tensile stress variation in the triangular zone were examined by varying simultaneously the Young's modulus and contact stiffness. With Figs. 4.8 to 4.11, it can be said that the deformability of stone walls in the extent of the simulation contributes little restraining of the rock slope displacement.

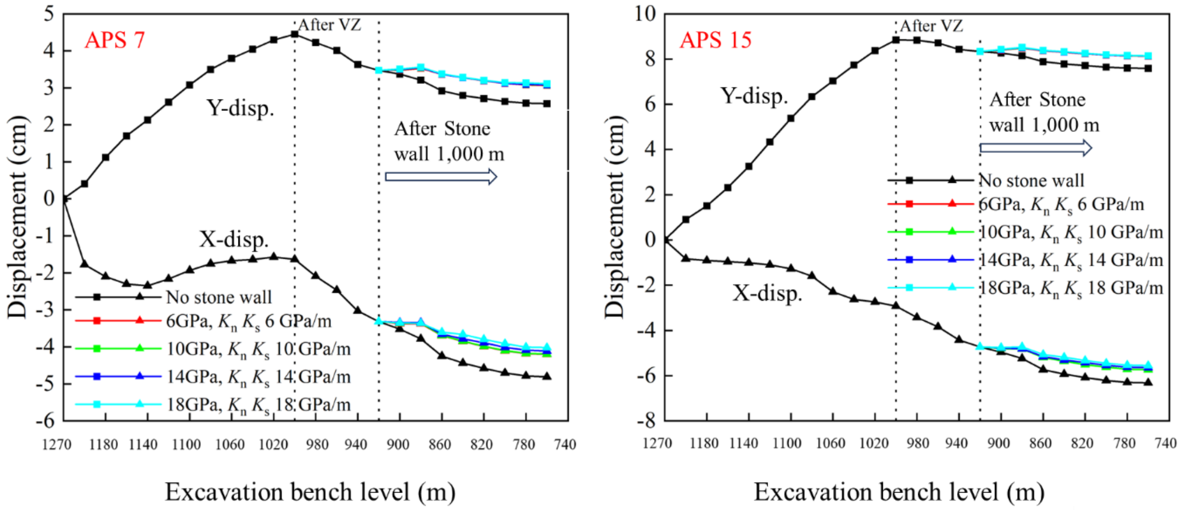

Fig.4.10: Displacement results by simultaneously varying stone wall Young's modulus and contact stiffness between stone walls and rock slope at APS 7 and APS 15.

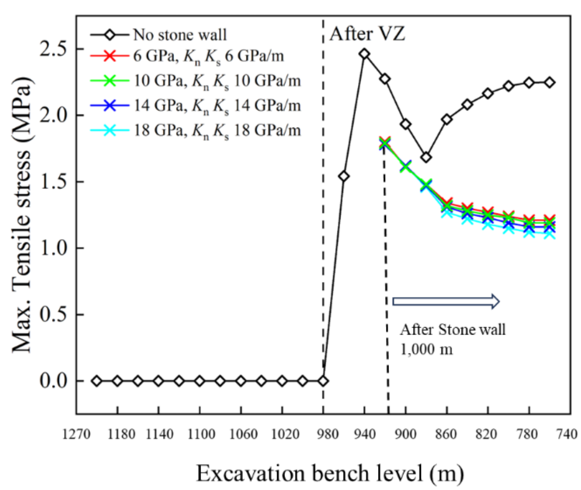

Fig.4.11: The maximum tensile stress changes in triangular zone by varying stone wall Young's modulus and contact stiffness between stone walls and rock slope.

Fig. 4.12 explores the influence of Poisson's ratio ($v = 0.2$, 0.25, and 0.3), showing negligible changes in slip displacement at APS7 and APS15. The result corresponds to the maximum tensile stress variation in Fig. 4.13.

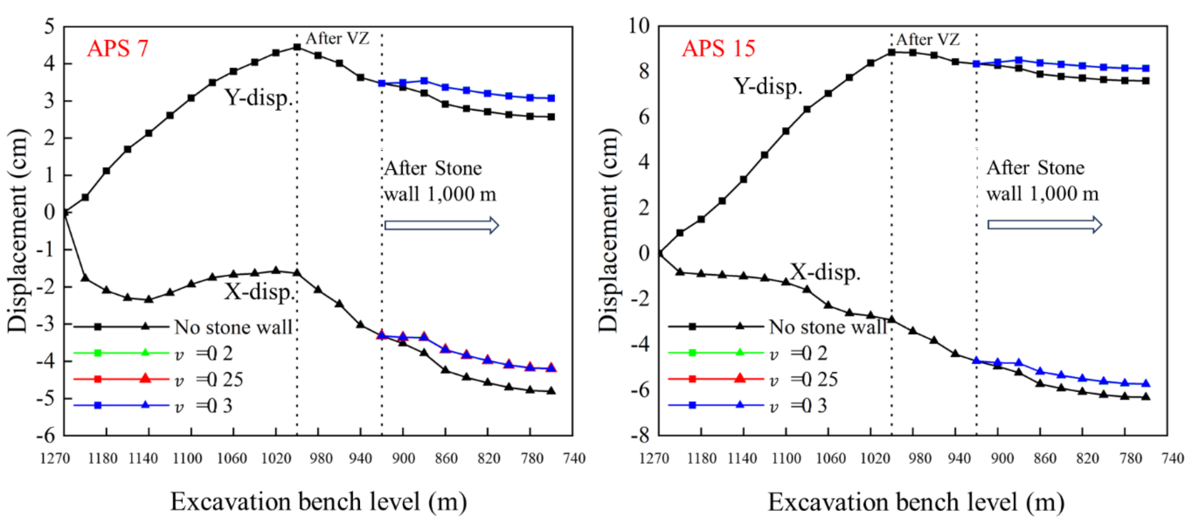

Fig.4.12: Displacement results by varying stone wall Poisson's ratio at APS 7 and APS 15.

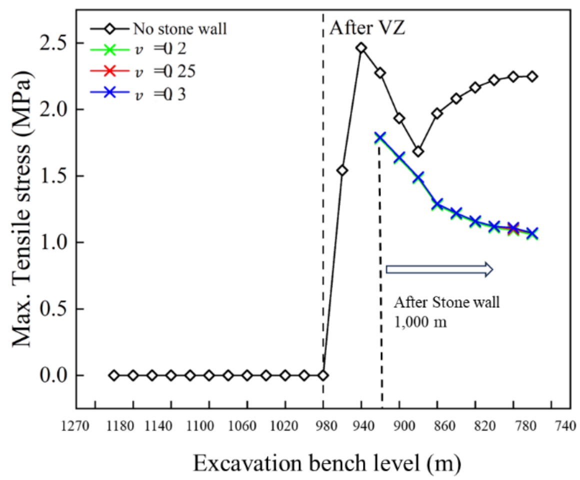

Fig.4.13: The maximum tensile stress changes in triangular zone by varying stone wall Poisson's ratio.

Fig. 4.14 examines the effect of density, defined relative to the limestone density of 2,548 kg/m³ (ρ). Slip displacement decreases with increasing stone wall density, and its limiting effect becomes almost negligible at 0.5ρ. However, as shown in Fig. 4.15, the maximum tensile stress decreases with increasing density, even when it is 0.5ρ, which also has a significant restraining effect on the tensile stress increasing. This result implies that the self-weight of the stone walls have a positive effect on restraining the slip deformation.

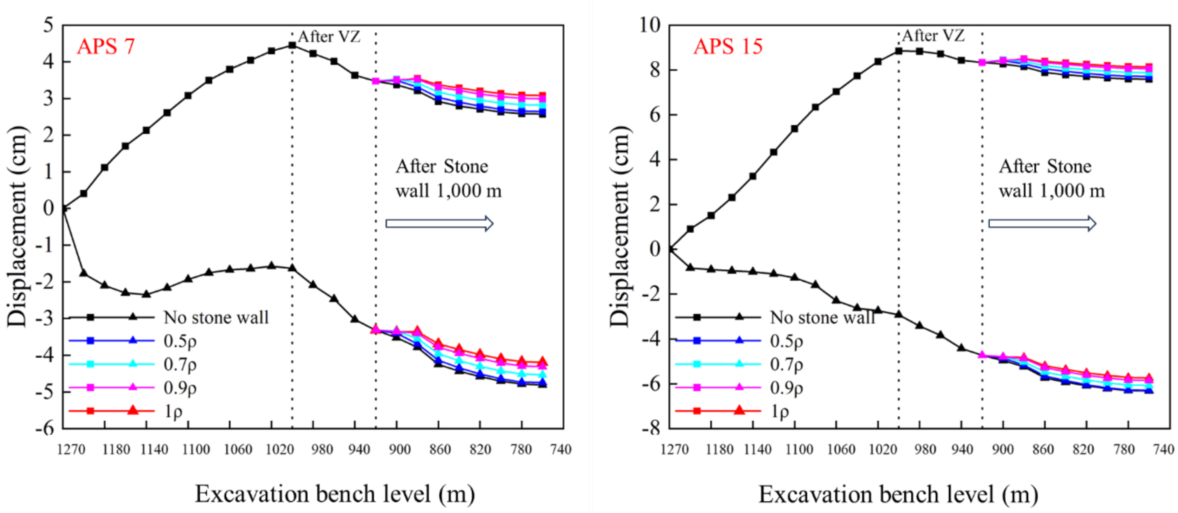

Fig.4.14: Displacement results by varying stone wall density at APS 7 and APS 15.

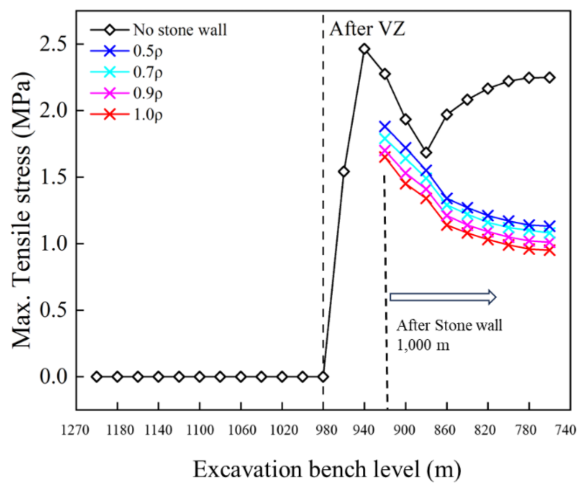

Fig.4.15: The maximum tensile stress changes in triangular zone by varying stone wall density.

4.4 Discussion

In the above simulation results, it is found that the increase in the self-weight (density and size) of the stone wall is effective in restraining the slip deformation. In this section, we will further investigate how the stone wall restraining slip deformation and give recommendation on dimensions of planning stone wall.

4.4.1 Mechanism of stone wall restraining slip deformation

Considering the slip mechanism proposed in 3.4.1, the stone wall is likely to restrain the bending deformation of the triangular zone. We first change the density of the stone wall to 0.0 to see if the stone wall can still limit the bending deformation of the triangular zone theoretically considering that the geometry of the triangular zone has changed under the construction of the stone wall. As shown in Fig. 4.16, although the maximum tensile stress changed little before the excavation level 880 m, decreased compared to the case without the stone wall. This result means the construction of stone wall can enhance the bending stiffness of the triangular zone by increasing second axial moment of area.

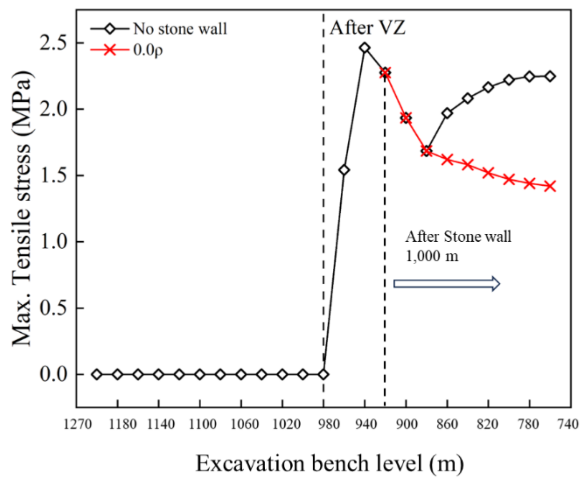

Fig.4.16: Maximum tensile stress variation in triangular zone under the density of stone wall 0.0.

We further investigated the effect of the Young's modulus and the contact stiffness between the stone wall and rock slope. In Figs. 4.9 and 4.11, the maximum tensile stress did not produce significant changes in the range of 6-18 GPa. However, the values of elasticity of the triangular zone should be very effective if the stone wall can enhance the bending stiffness of the triangular zone theoretically.

As shown in Fig. 4.17, we boldly changed the Young's modulus and contact stiffness simultaneously from 0.1 GPa and 0.1 GPa/m to 1,000 GPa and 1,000 GPa/m, respectively. The results show that a significant decrease in the maximum tensile stress in the triangular zone can be found at larger Young's modulus and contact stiffness. This further evidence that the stone wall can enhance the bending stiffness of the triangular zone. However, this effect is limited, considering that the elasticity coefficient of the stone wall does not produce such a large spanwise change.

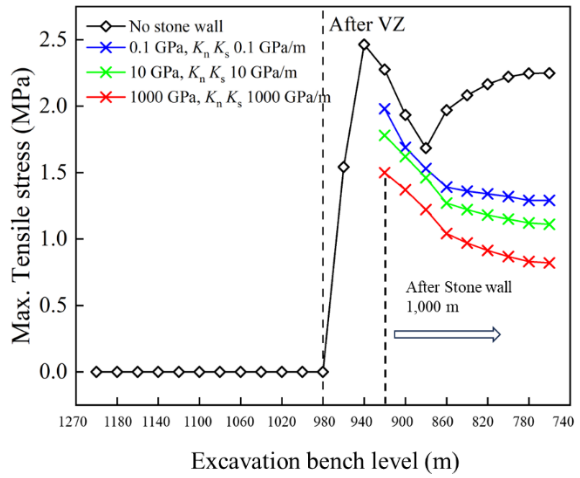

Fig.4.17: The maximum tensile stress changes in triangular zone by varying stone wall Young's modulus and contact stiffness from 0.1 GPa and 0.1 GPa/m to 1,000 GPa and 1,000 GPa/m respectively.

As shown in Section 4.3, the increases in the height and density of the stone wall induce a very significant change in the maximum tensile stress. Based on the proposed mechanism, stone wall can reduce failure zone along the discontinuity because the normal stress applied to the discontinuity certainly is increased. However, the reduction mechanism of failure zone is not so simple since there is no significant difference between stone wall height of 1,100 m and 1,050 m. In this subsection, stress state on PZ discontinuity is analyzed to understand the failure zone.

Fig. 4.18 shows the ratio between the shear stress (τ) and normal stress (σ) on PZ discontinuities after the construction of stone wall. The stone wall level of Figs (a), (b) and (c) are 1,000 m, 1,050 m and 1,100 m, respectively. The measurement points are the same in Fig. 3.8. It was found that when the stone wall was constructed up to 1,000 m, which is lower than VZ, stress state at Point C is lower than the failure criterion (Fig. 4.18a). Stress state at Point B as well as Point C is less than the failure criterion if the stone wall is constructed up to 1,050m or 1,100 m which is higher than VZ (Figs. 4.18b and 4.18c). In other words, the range of the non-failure zone on the PZ discontinuities was almost the same between 1,050 m and 1,100 m, suggesting that there was not much difference in the restraint effect of the two heights on slip displacement.

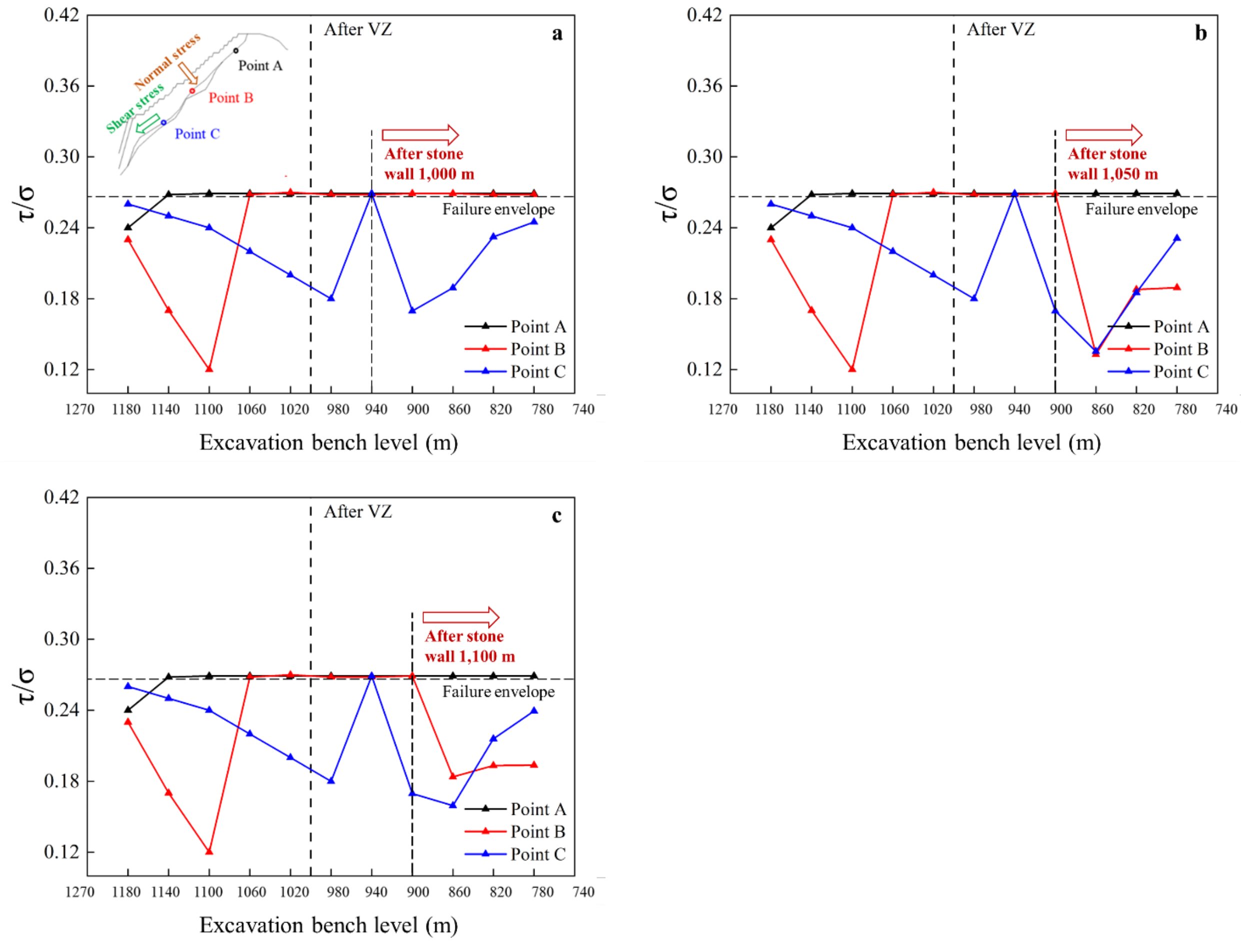

Fig.4.18: The ratio of shear stress and normal stress change after the construction of stone wall (a) with 1,000 m height, (b) with 1,050 m height and (c) with 1,100 m height in the parallel weak rock zone. (The dot line in horizontal direction represents the Mohr Coulomb failure envelope at Φ=15°, cohesion=0 MPa).

Based on the above change in stress state and the slip mechanism proposed in Section 3.4.1, the mechanism of stone wall restraining slip deformation can be explained as shown in Fig. 4.19. After the excavation level passed the VZ level, shear failure occurred along the PZ discontinuity due to the mining-induced normal stress reduction. The VZ is compressed and bending with the triangular zone (Fig. 4.19a). After the construction of the stone walls, the bending stiffness after the construction of stone wall (Figs. 4.16 and 4.17). Then, the stone wall presses the lower side of the slope, which in turn leads to the increase of the normal stress in the PZ discontinuities located on the lower side of the stone wall (Fig. 4.18). This ultimately leads to the stopping of the shear failure occurring along the PZ discontinuities (Fig. 4.19b and 4.19c).

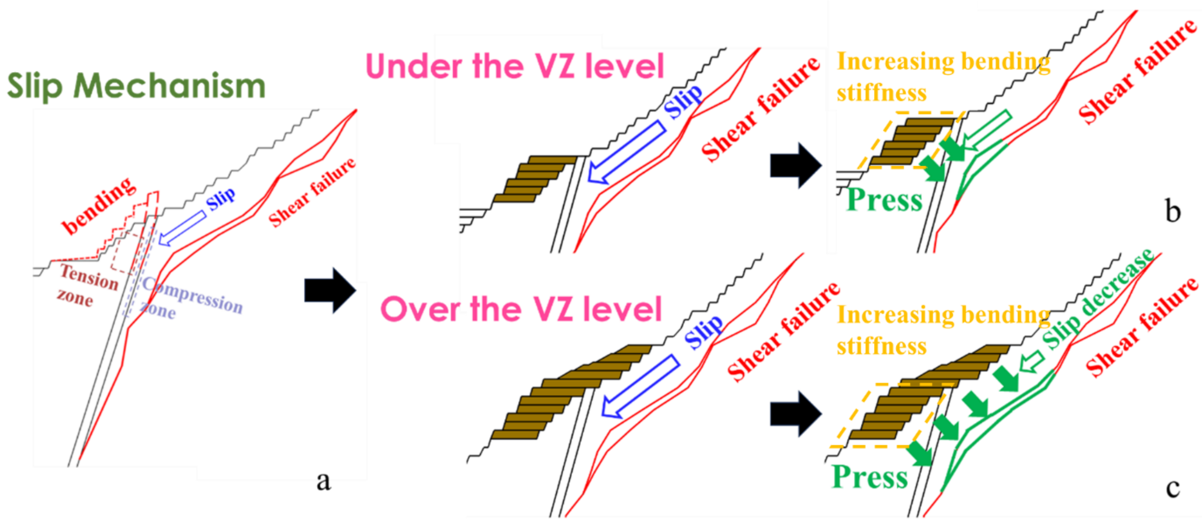

Fig.4.19: Mechanism of stone wall restraining slip deformation along the PZ discontinuities.

This "press effect" depends on the height of the stone wall. When the stone wall is constructed up to the VZ (1,050 m), the region of "press effect" is further expanded, and more PZ discontinuities located on its lower side will becomes a safe condition, so the slip deformation along the PZ almost stops, as shown by the cumulative deformation on the slope surface no longer decreases (Fig. 4.4).

4.4.2 Optimum design of stone wall

Despite the effectiveness of the current stone wall in restraining slip deformation at Mt. Buko, the dimensions of the stone wall are proposed to be further expanded for further increasing the rock slope stability.

As shown in Fig. 4.19, increasing the height of the stone wall can enhance the influence range of the "press effect". We found that when the height of the stone wall was constructed up to 1,050 m or 1,100 m, the slip deformation on the slope surface almost disappeared. In addition, considering that the effects between the 1,050 m height and 1,100 m height is not obvious either in terms of slope surface displacement or in terms of tensile stress in the triangular zone, it is recommended that the height of the stone wall be designed as 1,050 m.

Expanding the width of the stone wall likewise restraining the slip deformation significantly (Fig. 4.6 and 4.7). Considering that the slip deformation has almost disappeared with the planning stone wall width (Fig. 4.1c), there is no need to further expand the width of the stone wall, and continuing to build the stone wall to the planning dimension will effectively improve the slope stability in the future excavation.

4.5 Concluding marks

In this Chapter, we evaluated the effects of stone wall countermeasures on restraining rock slope deformation at Mt. Buko through numerical simulations. Impacts of dimensions and mechanical properties of the stone walls were examined for design of future stone wall. The specific conclusions are as follows:

1. The current stone wall, constructed to a height of 1,000 m, effectively restrains slip deformation. Increasing the height to 1,050 m, which is above the level of the VZ, results in a significant increase in effectiveness. However, raising the height to 1,100 m does not lead to a noticeable improvement.

2. The density and width of the stone wall influence its effectiveness. Higher density increases effectiveness, while reducing the wall's width decreases its performance. This indicates that the self-weight of the stone wall is a critical factor in enhancing its restraining effect.

3. The dominant mechanism of stone walls in restraining slip deformation is thought to be not only by increasing the bending stiffness of the triangular zone by changing the geometry of the triangular zone but also by the "press effect". This effect generated by the self-weight increases the normal stress on the PZ discontinuities, thereby stopping shear failure. This effect becomes more pronounced when the height of the stone wall exceeds the VZ.

4. Based on the above findings, a stone wall height of 1,050 m is sufficient for Mt. Buko, and the current width of the stone wall should not be reduced.

5. Several considerations on effects of weak rock zone and stone wall

5.1 Introduction

In Chapters 3 and 4, we evaluated the deformation mechanism of Mt. Buko and the role of stone walls. Our analysis revealed that the weak rock zone significantly affects mining-induced deformation, and stone walls are effective in restraining slip deformation. However, due to the unique rock slope geometry of Mt. Buko, key factors such as the dip direction of the weak rock zone and the construction timing of the stone wall could not be fully assessed. This chapter presents a more general study for further evaluation of the effects of weak rock zone and stone wall on mining-induced deformation of a rock slope by simplifying geometry of rock slope and weak rock zone. Specifically, effects of dip direction and connectivity of the weak rock zone, the thickness of a cover rock were investigated. Impacts of a height, width, and construction timing of the stone wall were also examined. These findings are expected to provide valuable insights for addressing deformation issues on rock slopes in open-pit mines.

5.2 Effects of dip direction of weak rock zone and connectivity

5.2.1 Discontinuous geological structures in open-pit mines

This section presents an overview of the typical discontinuous geological structures observed in open-pit mines (Fig. 5.1), including those considered in the case study. As illustrated in Fig. 5.1a, discontinuous geological structures that are nearly parallel to the slope surface (Nakamura et al., 2003) often exist between cover rock and base rock in limestone quarries, Japan. As the boundary between the limestone and base rock is often weathered by rainwater flow, it can become a discontinuous geological structure.

As indicated in Fig. 5.1b, a geological boundary is occasionally inclined against a rock slope surface with a high dip angle (Nakamura et al., 2003), where the geological boundary between slate and limestone is recognized as a discontinuous geological structure.

Additionally, faults can exhibit discontinuous geological structures. Fig. 5.1c illustrates an example of an inclined fault in a copper mine in Iran (Amini et al., 2019). The inclined fault between diorite and granodiorite is distributed in the middle of the rock slope. Figs. 5.1d and 5.1e indicate the faults dipping in a nearly vertical direction in a copper mine in Chile and a titanomagnetite mine in China, respectively (Flores-Gonzalez et al., 2018; Zhou et al., 2023). The ends of such faults exist either at the summit or hillside of the rock slope. The discontinuous geological structures observed in open-pit mines can be classified into the following patterns based on their dip direction: (i) parallel to the slope surface (parallel dip), (ii) nearly vertical (vertical dip), and (iii) inclined against a slope surface at a high angle (infacing dip).

In addition to a single geological structure, two discontinuous geological structures may exist in the rock slope of open-pit mines. Except for the Mt. Buko mentioned in Chapter 2, two open-pit mines with connective weak rock zones also exist in Fushun and Liaoning, China (Nie et al., 2014; Kang et al., 2022). In the former, a near vertical fault intersects a weak layer parallel to the slope (Fig. 5.1f), while in the latter, an oblique fault intersects a quartz vein (Fig. 5.1g). Combined with the distribution characteristics of Mt. Buko in Fig. 2.5, geological structure with two discontinuities can be classified as (iv) connective patterns and (v) non-connective patterns.

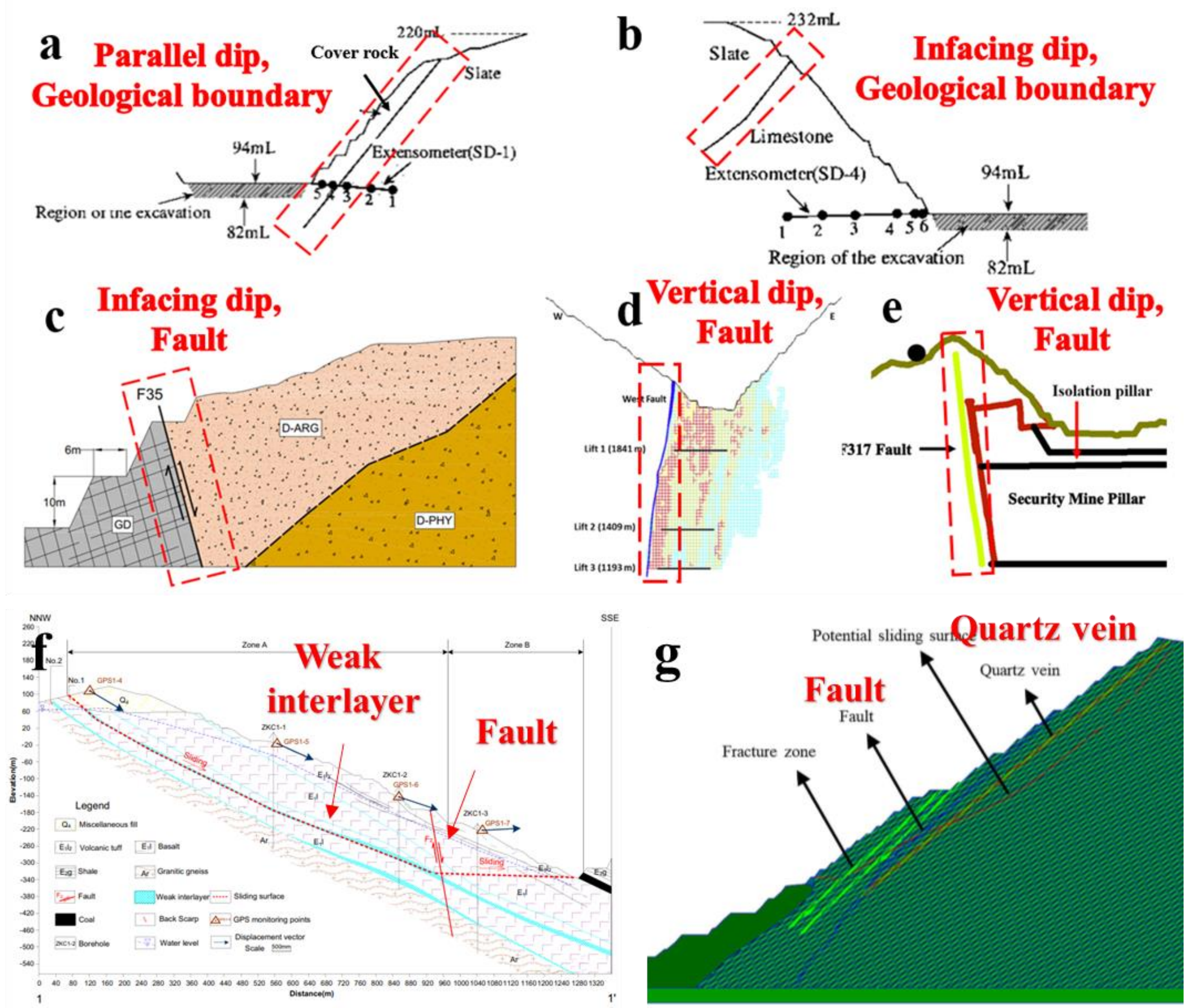

Fig.5.1: Examples of distribution patterns of geological structure in different open-pit mines.

5.2.2 Model introduction

As described in Section 5.2.1, there are many distribution patterns of discontinuous geological structures composed of geological boundaries and faults in open-pit mines. Here, we refer to a discontinuous geological structure as a weak rock zone since the strength of such a structure is usually smaller than the surrounding rock masses. In this section, a series of numerical models are prepared to examine the effects of weak rock zones on mining-induced deformation based on the cases classified in Section 5.2.1.

We constructed six simplified models corresponding to the patterns (i) to (v) in Section 5.2.1, including a homogeneous model with no discontinuity. Fig. 5.2(a) to (f) shows each model: (a) Homogeneous model (H model), (b) Parallel dip model (P model), (c) Vertical dip model (V model), (d) Infacing dip model (I model), (e) Connective Pattern model (CP model, (f) Non-Connective Pattern model (N-CP model). The model dimensions and shapes in all models are same. The lengths in vertical and horizontal directions are 500 m and 800 m, respectively, and the slope angle is 45 degrees.

The excavation area is set on the upper left side of the slope. Zones with a width of 50 m and a height of 180 m are sequentially removed from the top of the slope step by step to represent excavation progression with 9 excavation stages as shown in Fig. 5.3. Each excavation zone is 20 m in height. At the 5th excavation stage, the excavation face passes the vertical weak rock zone (VZ) in the V, CP and N-CP models as shown in Fig.5.2(c), (e) and (f). Additionally, in the model with the parallel dip (P, CP and N-CP models), a cover rock with a thickness of 10 m will be formed as the excavation proceeds (Fig. 5.2(b), (e) and (f)).

In this study, mechanical effects of the weak rock zones are represented by discontinuous deformation on the boundary between the weak rock zone and the rock mass. The boundary is modeled as a discontinuity plane in the framework of Discrete Element Method (DEM), while both the rock mass and the weak rock zone are modeled as an elastic material. For the sake of simplicity, Young's modulus for the rock masses and the weak rock zones are assumed as 1 GPa and 0.1 GPa, respectively, since the weak rock zone is expected to be more deformable than the rock mass. Poisson's ratio is set at 0.25. The stiffness and frictional angle of the discontinuities are determined based on several references (Table 3.4). Eventually, the value of K_n is calculated to be approximately 1.0 GPa/m, and the K_n-to-K_s ratio and the friction angle are assumed to be 2.0 and 30 degrees, respectively, according to the references. The specific values are summarized in Tables

5.1 and 5.2.

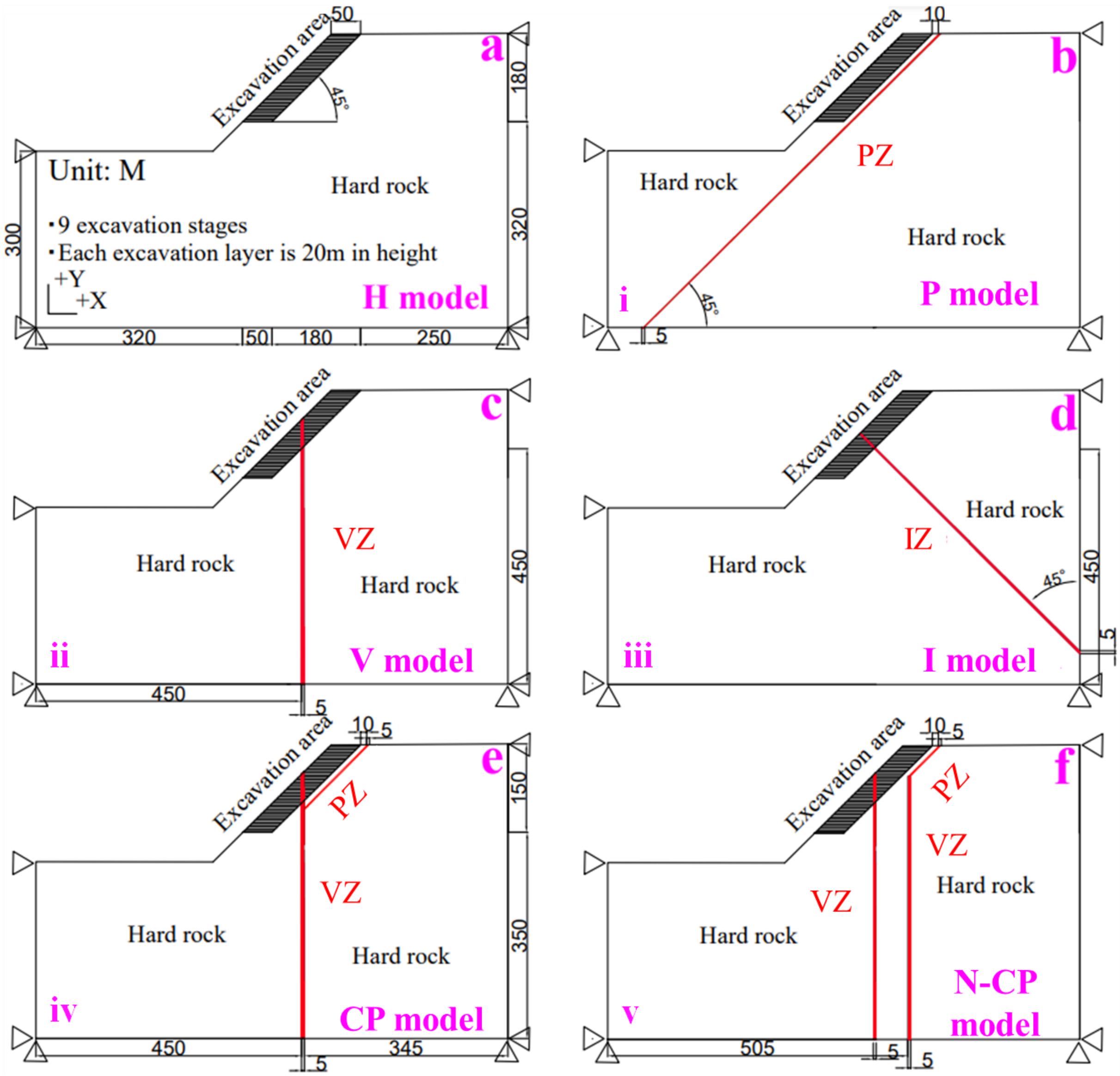

Fig.5.2: The geological condition of simplified models. (a) Homogeneous model, (b) Parallel dip model, (c) Vertical dip model, (d) Infacing dip model, (e) Connective Pattern model, (f) Non-Connective Pattern model.

Table 5.1: Mechanical properties of rock mass used in models.

Properties	Weak Rock Zone	Limestone
Density (kg/m³)	2700	2700
Young's modulus (GPa)	0.1	1
Poisson's ratio	0.25	0.25

Table 5.2: Mechanical properties of discontinuities used in models.

Properties	Weak Rock Zone-Rock Mass Contact
K_n (GPa/m)	0.1
K_s (GPa/m)	0.05
Friction (°)	30

5.2.3 Simulation procedure and monitoring points

The simulation involved the following three steps: (1) Displacements perpendicular to the bottom and lateral boundaries of the model were fixed at zero. (2) The initial iterations were performed under gravity to generate the initial stress state. (3) Iterations were executed while removing the excavation zones and recording the changes in displacement and stress. The model response was monitored during the third step.

Fig. 5.3 depicts the displacement and stress measurement points. Points 1 and 2 were used to observe the surface displacement of the rock slope. Considering the CP model as an example, Points 1 and 2 were located above and below the VZ, respectively. Points A–B were used to monitor the stress changes in the discontinuities along the weak rock zones. Point A was set on the weak rock zone parallel to the slope surface (PZ), whereas Point B was set on the vertical weak rock zone (VZ).

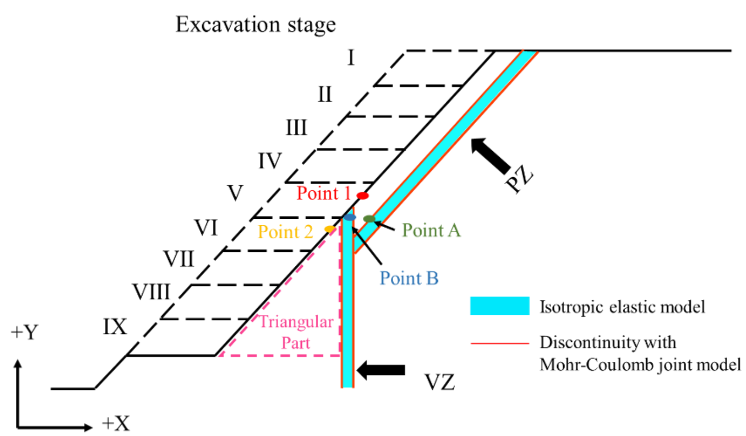

Fig.5.3: Measurement points in simplified models.

5.2.4 Simulation results

The horizontal and vertical cumulative displacement increments at Points 1 and 2 due to excavation are shown in Fig. 5.4 with positive values corresponding to the backward and upward directions in x and y direction, respectively (Fig.5.3). The vertical displacements in all the models except CP model exhibit upward through the nine excavation stages. In contrast, downward displacement is observed at Point 1 in the CP model after the 5^{th} excavation stage, although the upward displacement is seen at Point 2. The rate of the downward displacement tends to decrease with excavation stages. In the horizontal direction, mining-induced displacement of all the models except CP model is almost negligible compared to the vertical displacement. In contrast, horizontal displacement of the CP model shows an obvious increase in the forward direction after the 5^{th} excavation stage. However, the increasing rate gradually decreases with the progression of the excavation stage.

As mentioned above, vertical displacement and horizontal displacements of CP model shows dramatic change when the excavation exceeds the 5th stage at which the excavation face reached to the vertical weak rock zone. For understanding the mechanism behind this change, displacement increment vectors from the initial state to the 5th stage and from the 5th to 9th stages were analyzed. Fig. 5.5 shows the vectors in the former stage, while Fig. 5.6 depicts those in the later stage. From the figures, it is found that the displacement mode of models with a single weak zone and N-CP models is almost similar to that of the H model with no weak rock zone. Although there is a slight difference in the displacement in that the upward displacements of the models with a weak rock zone are greater than H model, the rock slope in these models shows upward displacement in both stages. As shown in the figure, the deformation mode of CP model is different in that the vectors are still upward until the 5th stages (Fig. 5.5e), but the rock slope on the PZ starts to show sliding deformation along the upper boundary of the PZ after the stage (Fig. 5.6e).

The above results indicate that the cover rock above the PZ in CP model begins to slide along the PZ when the excavation face passed the VZ and that the sliding deformation reduces in the subsequent excavation stage. Furthermore, the above results imply that the single weak rock zone does not significantly affect mining-induced deformation. The rock slope shows mainly upward displacements caused by elastic recovery due to the gravity release. A special structure such as the connection of PZ to VZ could induces downward and forward displacement due to the sliding.

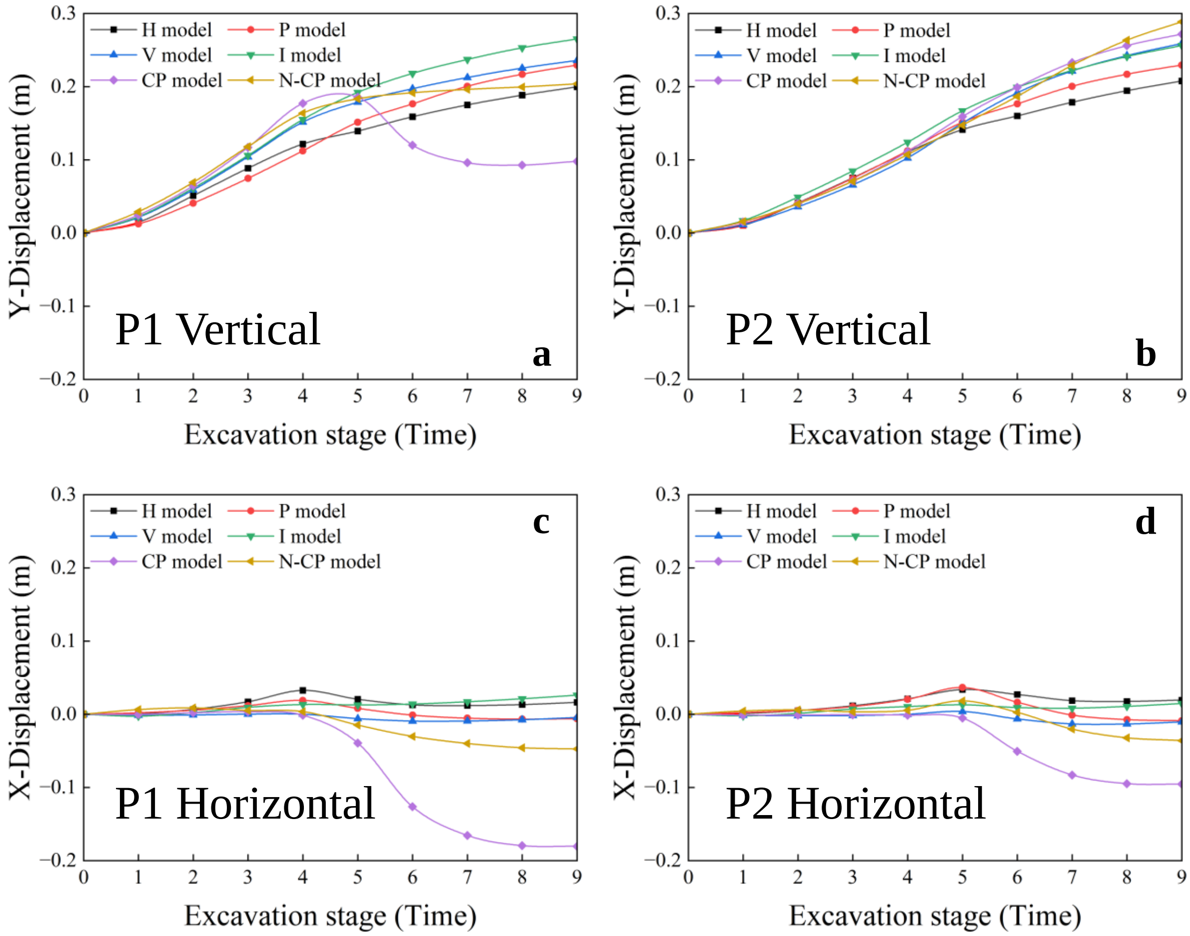

Fig.5.4: The cumulative displacement curves of each simplified model. (a) Vertical displacement in P1. (b) Vertical displacement in P2. (c) Horizontal displacement in P1. (d) Horizontal displacement in P2.

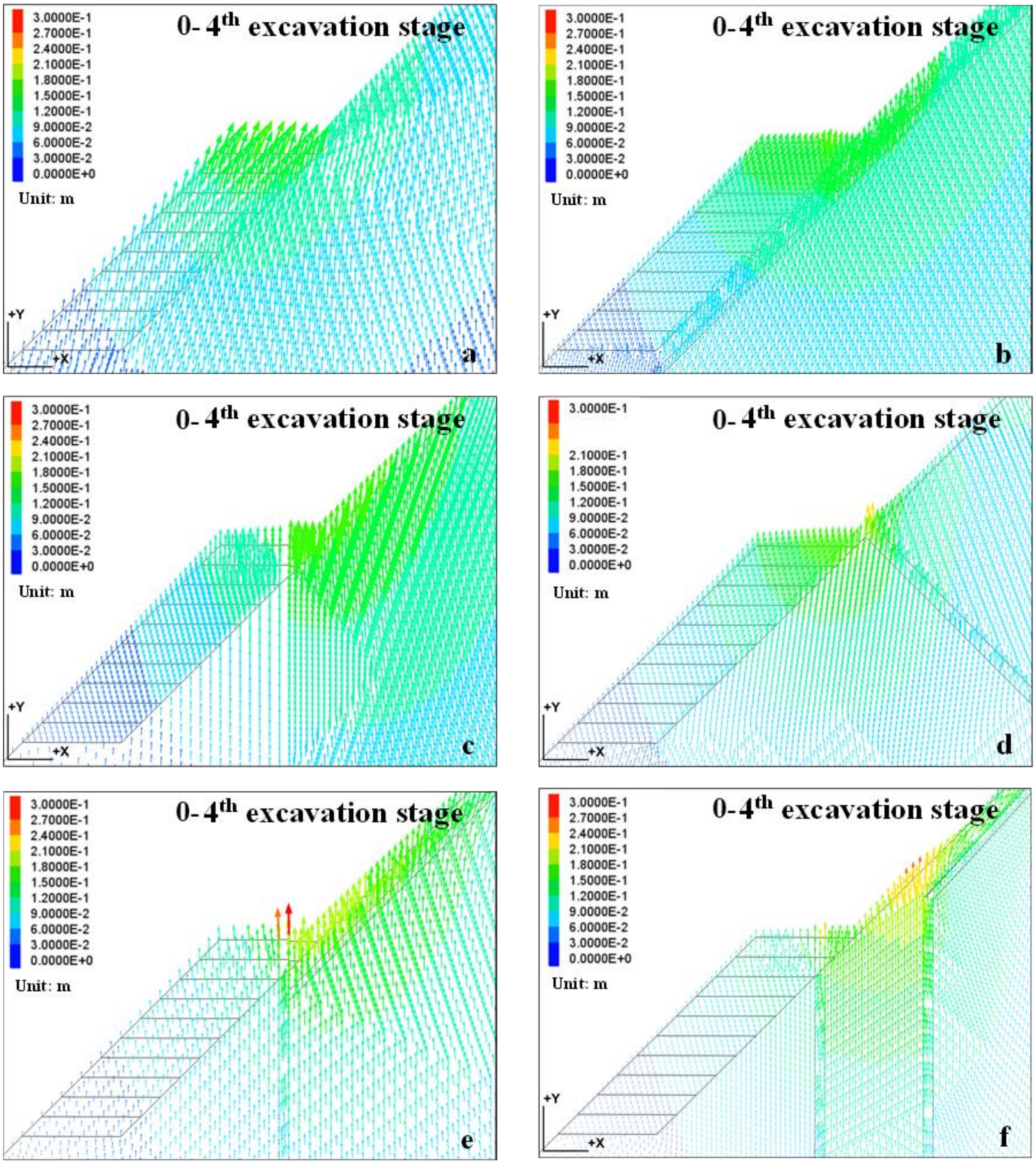

Fig.5.5: Displacement vectors of each simplified model, before the excavation face passes the vertical weak rock zone (0 - 4th excavation stages). (a) H model, (b) P model, (c) V model, (d) I model, (e) CP model, (f) N-CP model.

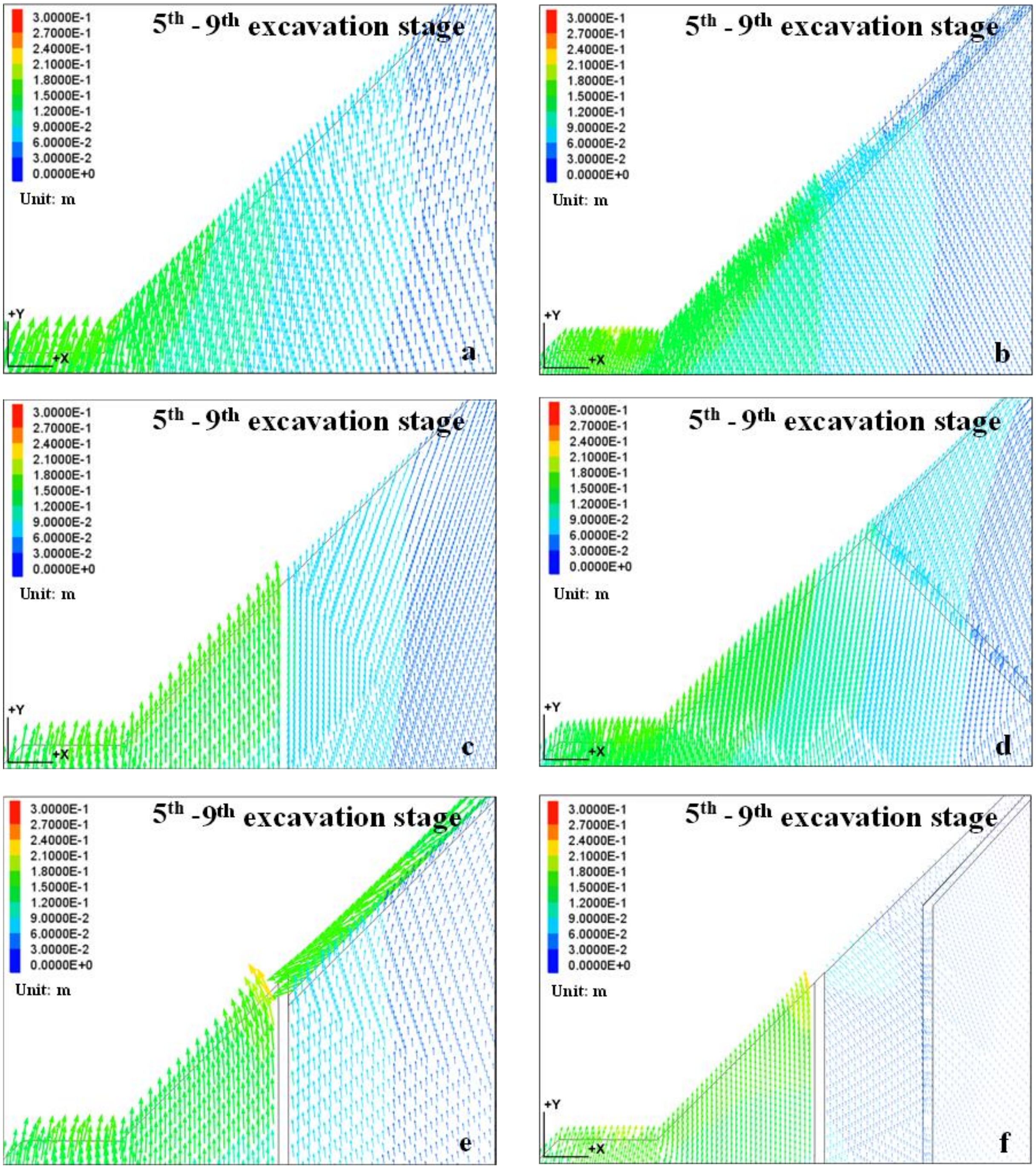

Fig.5.6: Displacement vectors of each simplified model, after the excavation face passed the vertical weak rock zone (5^{th} - 9^{th} excavation stages). (a) H model, (b) P model, (c) V model, (d) I model, (e) CP model, (f) N-CP model.

Given that the CP model can be viewed as a simplification of the A-A' section model of Mt. Buko, as well as the highly similar deformation characteristics of the two (Fig. 3.3a and Fig. 5.6e): both slip deformation occurs after the excavation level passed the VZ level; and both triangular zones show forward and upward deformation. The slip mechanisms of the two should be the same.

Further investigation was performed to verify the slip mechanism. Another model was constructed by varying the geometry of the VZ in the CP model (Figure 5.7a). In this model, the VZ did not cross the cover rock. Figure 5.7b illustrates the displacement increment vectors from the 5th to 9th stages of the new model. The mining-induced displacement was upward in the same manner as that observed in the P and V models (Figure 5.6a, b). Therefore, the triangular structure formed by the VZ crossing the cover rock in the CP model contributed to slip occurrence.

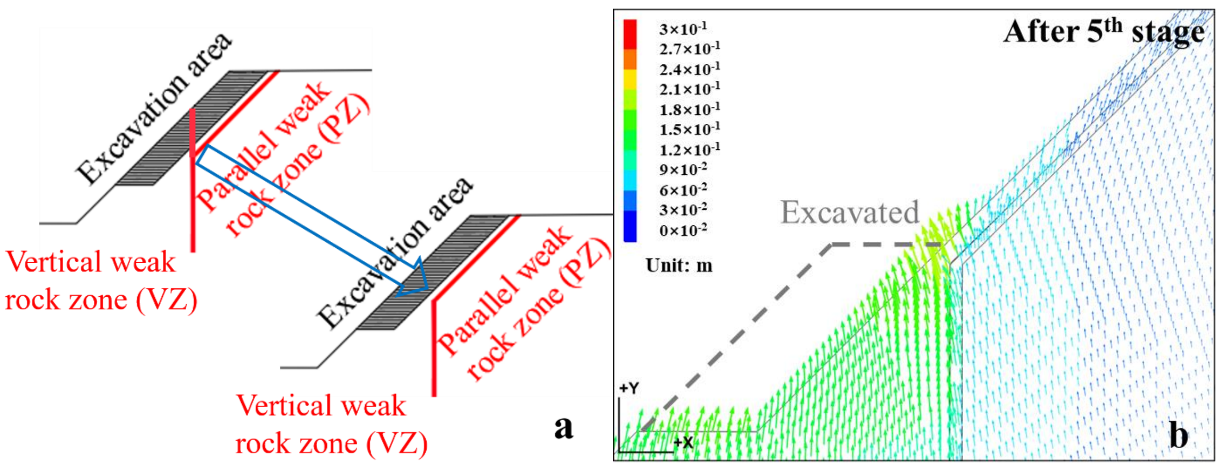

Fig.5.7: (a) Connecting the two weak rock zones (VZ and PZ) of CP model into one. (b) The result of cumulative displacement vectors after the excavation face passed the VZ.

5.3 Effects of cover rock thickness

In the description of the slip mechanism (Section 3.5.1), after the excavation level passed the VZ level, the cover rock slides along the PZ discontinuities, pushing the VZ and bending the triangular zone. The pushing effect and bending resistance are likely to relate to the cover rock thickness. In this section we will discuss the effect of cover rock thickness on slip deformation of the following two cases to provide recommendations for excavation design for open pit mines facing similar conditions. (a) cover rock thickness is not changed through excavation progression (No change case). (b) cover rock thickness is increased when the excavation face passed down the vertical weak rock zone (Increase case).

5.3.1 No change case

As shown in Fig. 5.8, cover rock thickness in the CP model which has cover rock height of H, is set at H/20, H/10, 3H/10, H/2, and H. For each case, we recorded the cumulative displacement at Points 1 and 2, located at 480 m and 460 m along the slope surface, respectively, to compare the intensity of slip occurrence. The simulation procedure and model parameters are same as those described in Sections 5.2.3.

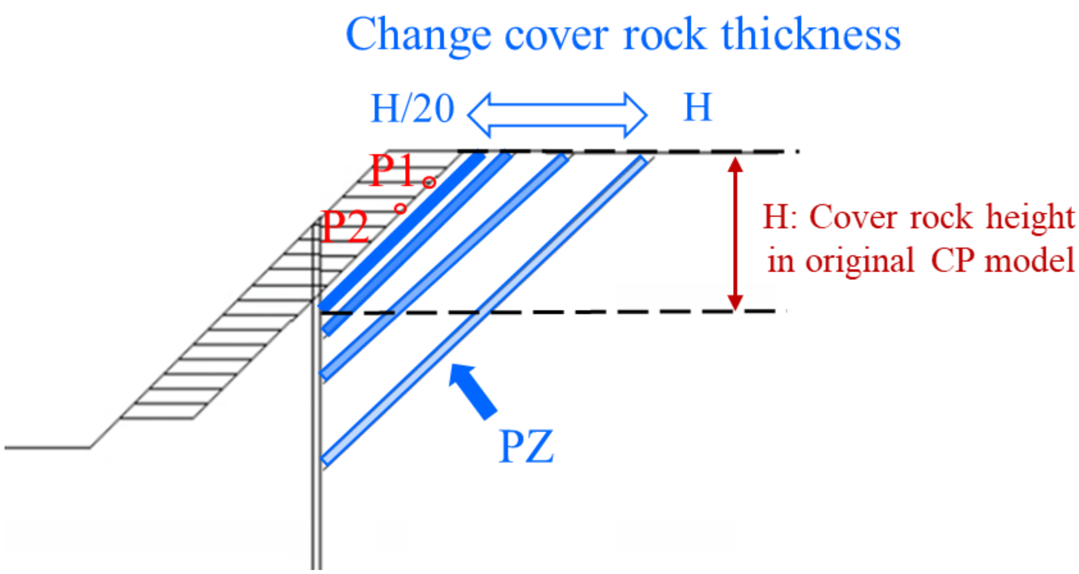

Fig.5.8: Diagram of Cover Rock Thickness Variations in the CP Model.

Fig. 5.9 shows the cumulative displacement with varying cover rock thickness. When the thickness increases from H/20 to H/10, slip displacement still occurs but is reduced. As the thickness continues to increase from H/10 to H, the slip displacement gradually decreases, eventually a little displacement can be seen when the thickness reaches 7H/10.

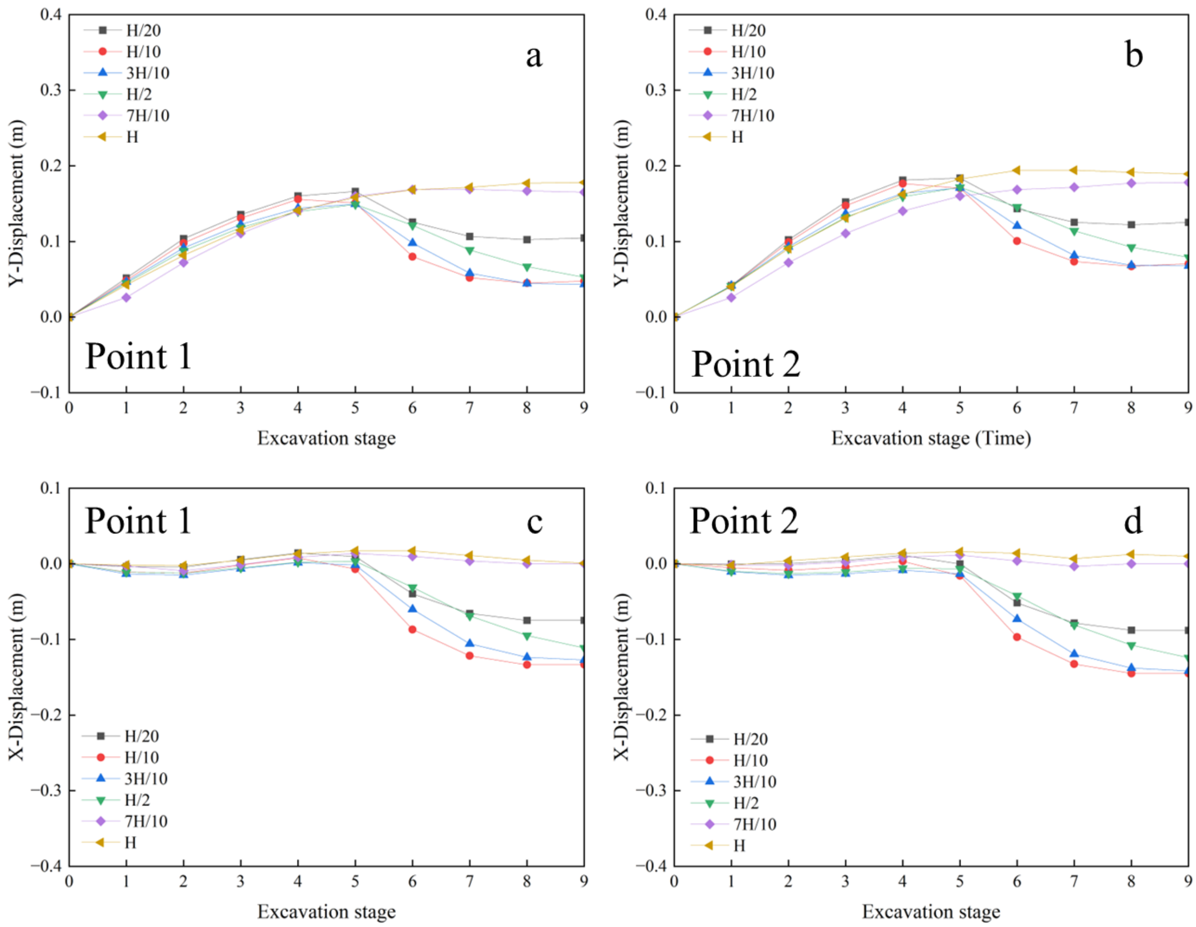

Fig.5.9: Results of cumulative displacement when changing the cover rock thickness. a. Vertical displacement in Point 1, b. vertical displacement in Point 2, c. horizontal displacement in Point 1, d. horizontal displacement in Point 2.

Fig. 5.10 illustrates the variation in joint normal stress at Point B (Fig. 5.3) at different cover rock thickness. Monitoring this indicator helps clarify the effect of the cover rock's extrusion on the lower VZ and triangular zone. The initial joint normal stress increases uniformly with cover rock thickness; however, after the excavation level reaches the VZ level (5^{th} excavation stage), the increment in joint normal stress varies depending on the thickness. Specifically, the increment tends to increase as the thickness increases from H/20 to H/10, but decreases as it changes from H/10 to H/2. The joint normal stress at a thickness of 7/H shows little to no change during excavation.

Fig. 5.11 shows the stress variation in the PZ discontinuity at Point A (Fig. 5.3) at the 7^{th} excavation stage. Although both normal and shear stresses increase with cover rock thickness, the ratio of shear to normal stress begins to decrease at 7H/10. The risk of shear failure decreases rapidly when the cover rock thickness is greater than H/2. This trend suggests that there is a critical thickness stabilizing a cover rock.

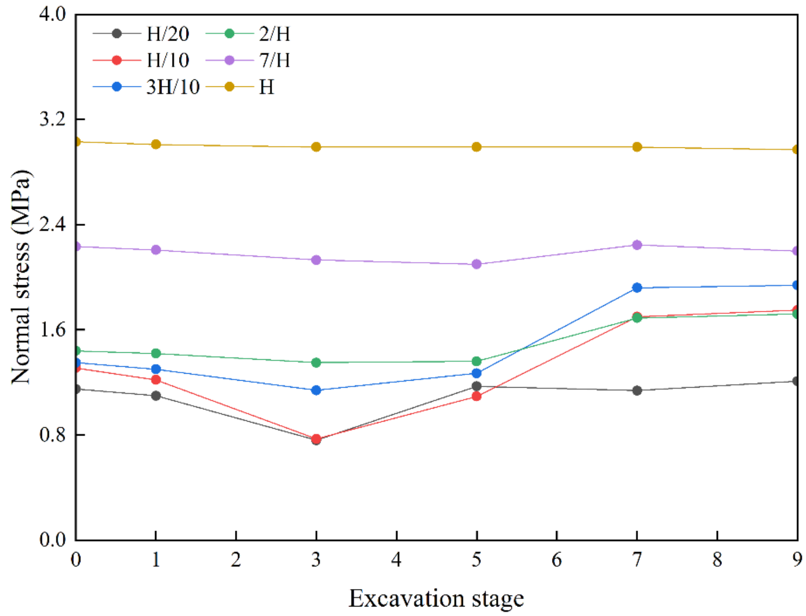

Fig.5.10: Results of joint normal stress at Point B when changing the cover rock thickness.

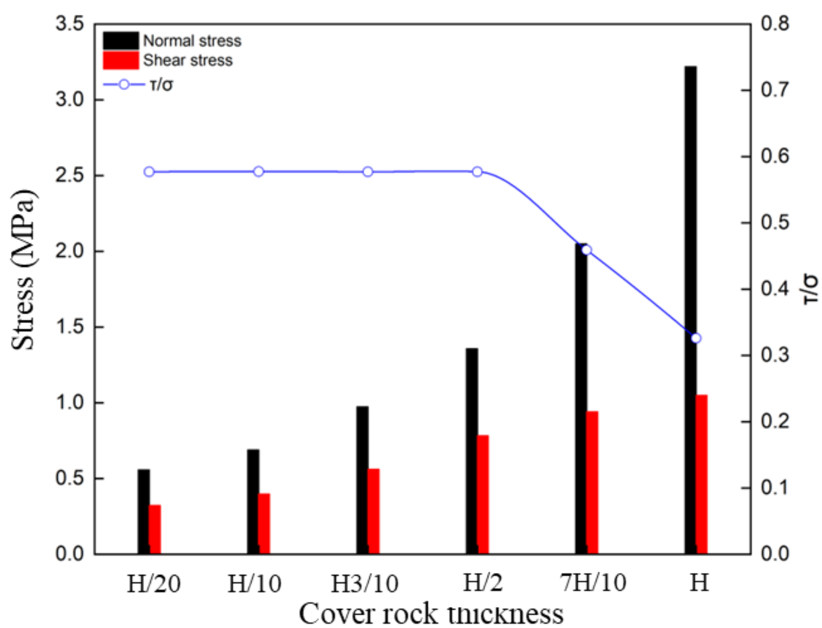

Fig.5.11: Stress variation at Point A when changing the cover rock thickness. The cylinders represent stress, and the blue line represents the ratio of shear stress and normal stress change.

Based on the CP model's slip mechanism, we believe that when the cover rock thickness is too low (H/20), its self-weight is insufficient to induce slip along the parallel weak rock zone and to bend the triangular zone, restraining the slip movement. Conversely, increasing the cover rock thickness will also be helpful for restraining the slip movement due to the contact area between the cover rock and the VZ. The slip displacement converged when the thickness of cover rock is greater than half of the cover rock height (7H/10).

5.3.2 Increase case

As shown in Fig. 5.12, The bench width is decreased to increase the dimension of front zone (triangular zone) to 1/10, 2/10, and 3/10 of the width of the excavation area (***W***) after the excavation face passed the VZ. For each case, we recorded the cumulative displacement at Points 1 (Fig. 5.3), to compare the intensity of slip occurrence. The simulation procedure and model parameters are consistent with those described in Sections 5.2.3.

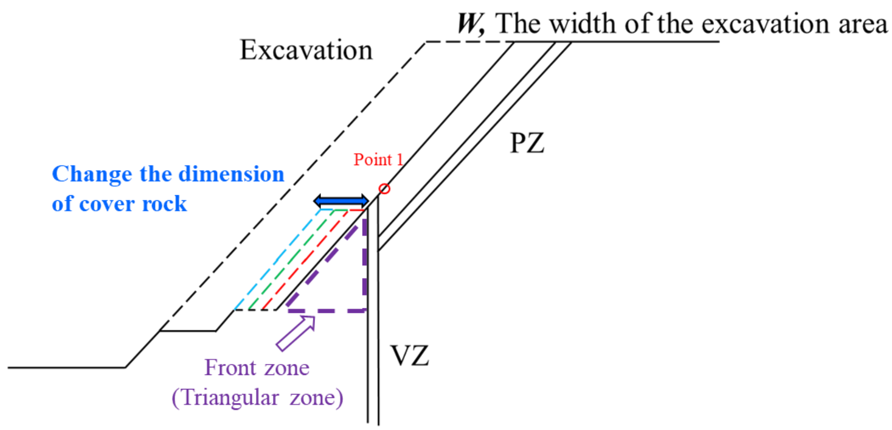

Fig.5.12: Diagram of dimensions of triangular zone variations in the CP Model.

Fig. 5.13 displays the displacement results of increasing the dimensions of front zone at Point 1, where T = 0 represents the original model. Positive values indicate displacement in the backward and upward directions in the X and Y axes, respectively. As the thickness of the cover rock in front of VZ (T) increases, slip displacement decreases in both directions following the VZ stage. This decrease is positively correlated with the increased thickness. When T equals 3W/10, almost no slip displacements occur.

Similarly, the maximum tensile stress in the front zone reflects the displacement trends, as shown in Fig. 5.14. The maximum tensile stress decreases gradually and ultimately converges with the increasing dimension of front zone. The minimum tensile stress reaches approximately 0.5

MPa at T = 3W/10 (Fig. 5.14a), and the decrease shows converge with the increase of thickness (Fig. 5.14b). Based on the results of displacement and tensile stress, we believe that there is a critical thickness stabilizing the cover rock. The thickness of 3/10W is the critical value for the model used in this simulation.

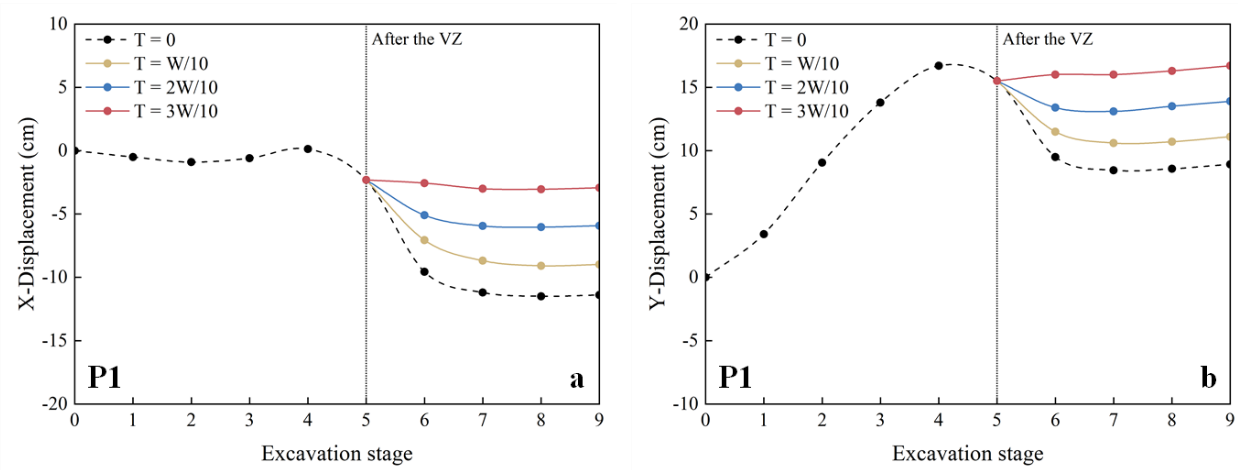

Fig.5.13: Impact of thickness in front zone on displacement at Point1 at (a) Horizontal direction, (b) Vertical direction.

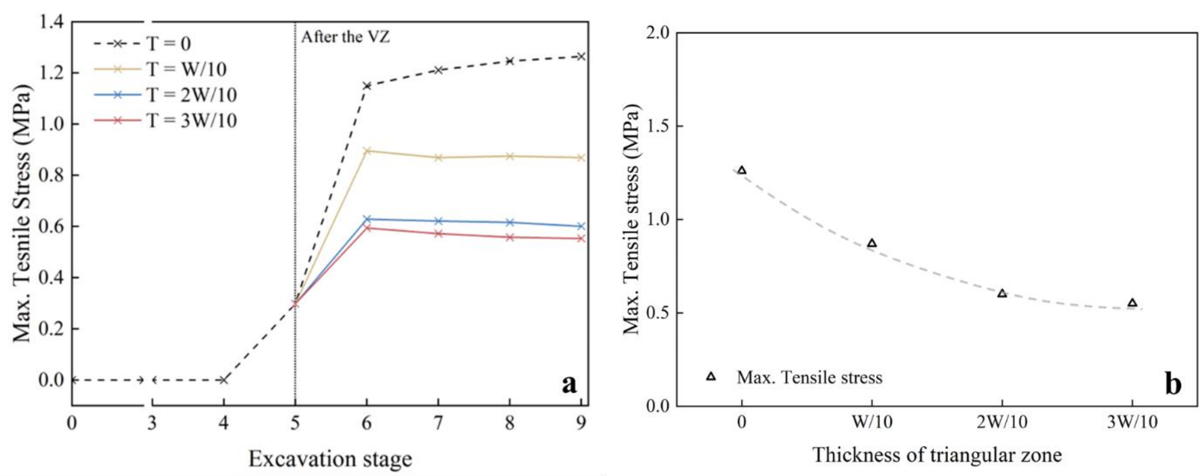

Fig.5.14: Tensile stress variations by front zone thickness (a) during excavation progress, (b) at final excavation stage.

5.4 Effects of stone wall dimension and construction timing

In Chapter 4, we analyzed the role of the stone wall at the quarry in restraining slip deformation. However, due to the geometrical characteristics of the stone wall and the rock slope at Mt. Buko, it is not possible to generalize and study the stone wall in a general way. In this section, we will use a simplified CP model to study the height, width, and construction timing of the stone wall more comprehensively, and give recommendations for the design of the stone wall.

5.4.1 Simulation models

As shown in Fig. 5.15, the following three effects are considered. (a) Effects of stone wall width. The stone wall is constructed up to the VZ level with four different widths: W/10, 2W/10, 3W/10, and 4W/10(W is the width of the excavation area). The stone walls are the same dimensions in subsequent excavations. (b) Effects of stone wall height. The stone wall is constructed at five different heights with a width of W/5: H/5, 2H/5, ..., H (H is the height of the cover rock). The case of H/5 represents the stone wall constructed up to the VZ level, while the other cases represent the stone wall constructed beyond the VZ level. (c)Effects of construction timing of stone wall. Stone wall is constructed at 6th excavation stage and at 7th excavation stage. Stone wall constructions in (a) and (b) were defaulted to begin at the 6th excavation stage at which the excavation level passes down the VZ.

The stone wall countermeasure models are developed based on the CP model, therefore, the numerical model and parameters for rock masses are same as the CP model in Section 5.2.2. The contact of weak rock zones and the contact of the stone wall with the slope were represented by discontinuous deformation as shown in Fig. 5.16. The boundary was modeled as a discontinuity plane in the discrete element method framework, whereas the rock mass, weak rock zone and stone wall were modeled as elastic materials. The Young's moduli for the stone wall were set to be 0.5 GPa. Young's modulus of the stone wall is certainly less than Young's modulus of rock mass because it consists of the blocks of the rock mass. Poisson's ratio was set to 0.2. The contact stiffnesses of the stone wall were defaulted to 1GPa/m, Tables 5.3 and 5.4 summarize the specific values.

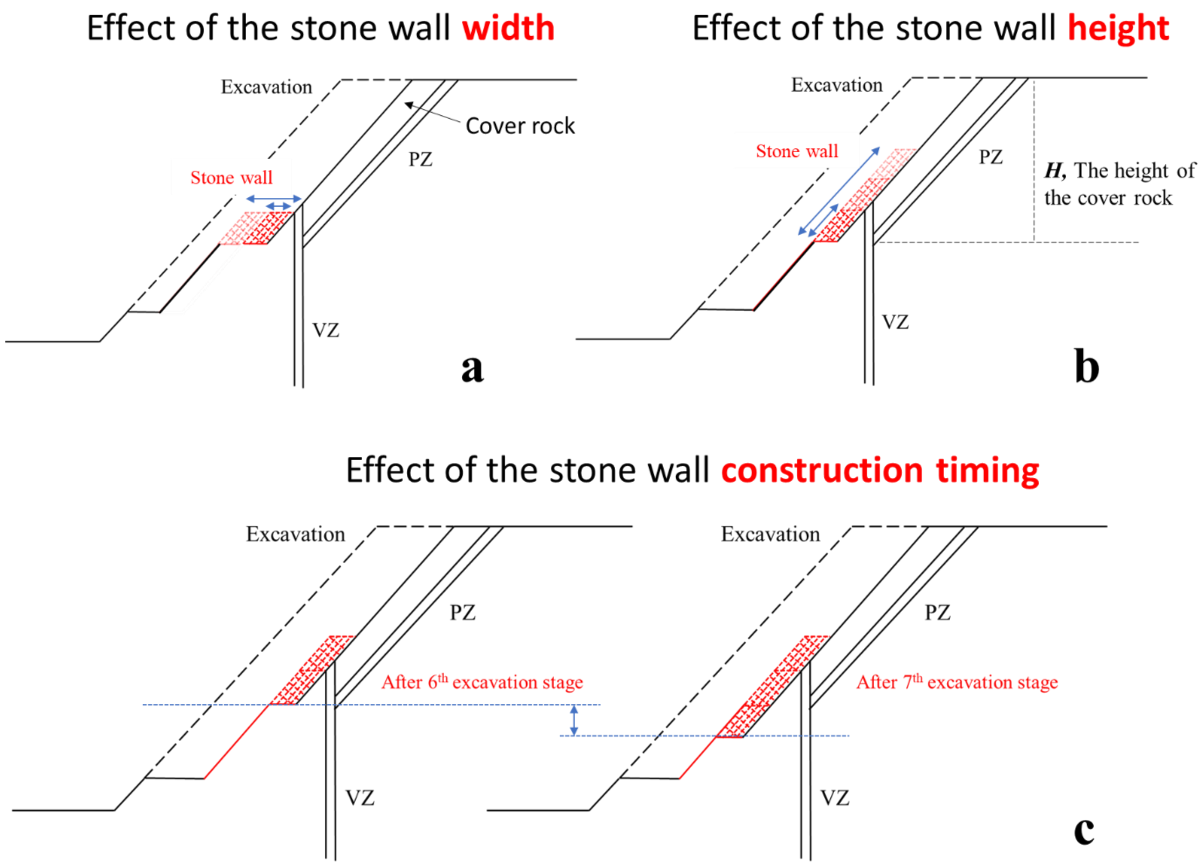

Fig.5.15: Countermeasure models.

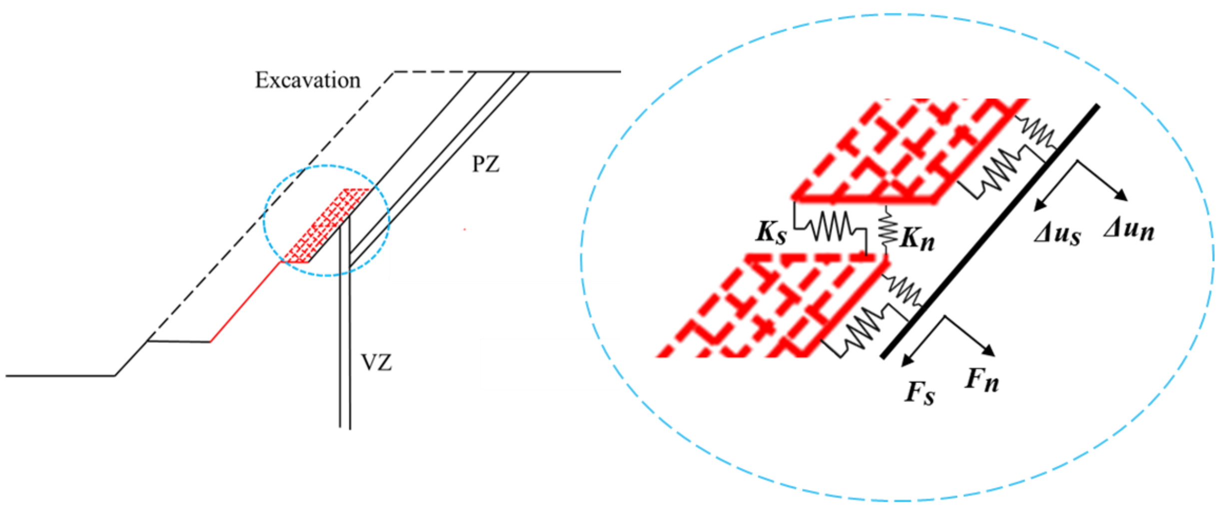

Fig.5. 16: Contact model of the stone wall.

Table 5.3: Mechanical properties of stone wall

Density (kg/m3)	2100
Young's modulus (GPa)	0.5
Poisson's ratio	0.2

Table 5.4: Contact properties of numerical models.

Properties	Stone wall – stone wall contact	Stone wall – rock mass contact
K_n (GPa/m)	1	1
K_s (GPa/m)	1	1
Friction (°)	30	30

5.4.2 Numerical simulation procedure and monitoring points

The simulation involved the following five steps: (1) Displacements perpendicular to the bottom and lateral boundaries of the model were fixed at zero. (2) Initial iterations under gravity were conducted to establish the initial stress state. (3) Iterations proceeded with the removal of excavation zones, during which changes in displacement and stress were monitored throughout the initial half of the excavation process. (4) Elements for stone wall were incorporated to the model in a single step, followed by iterations under gravity. (5) The simulation concluded with the completion of the second half of the excavation, recording the variations in displacement and stress. The maximum tensile stress in the triangular zone during excavation was recorded.

5.4.3 Simulation results

5.4.3.1 Effect of the stone wall width

Fig. 5.17 displays the variations in the maximum tensile stress in the triangular zone under different widths of the stone wall. All stone wall's heights are under the VZ level. Although the maximum tensile stress decreased after the construction of the stone walls, the effect of width of stone walls is not significantly (Fig. 5.17a). When the width of stone walls increased from W/10 to 2W/10, there was a slight decrease in the maximum tensile stresses, but increasing the width again produced no further change (Fig. 5.17b).

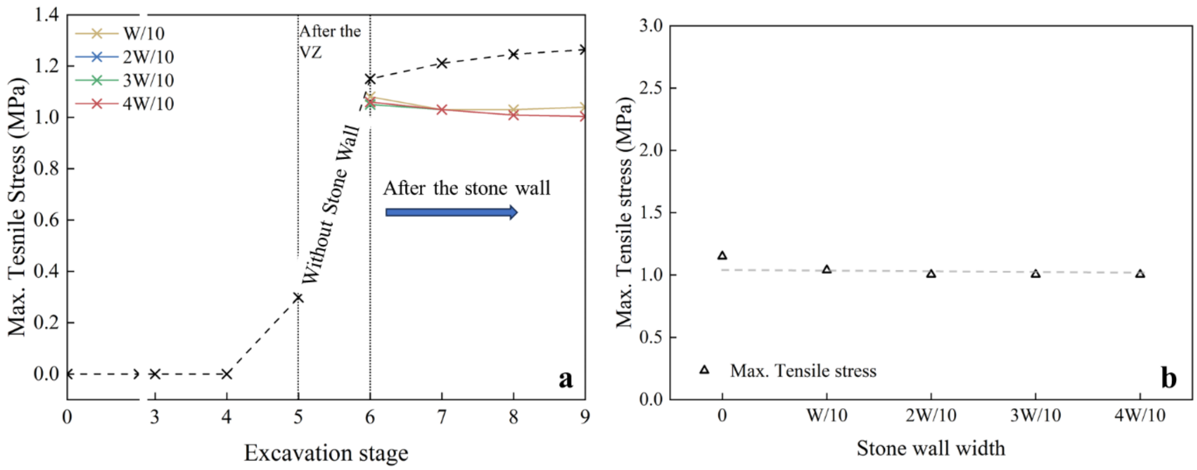

Fig.5. 17: Tensile stress variations by stone wall width.

5.4.3.2 Effect of the stone wall height

Fig. 5.18 presents the variations in maximum tensile stress in the triangular zone under different heights of the stone wall. All stone wall's widths are 2W/10. Compared to scenarios with no stone wall, all heights of the stone wall contribute to the reduction in maximum tensile stress. However, the reduction is significantly greater when the stone wall is constructed beyond the VZ level than at the VZ level (H/5) (Fig. 5.18a). In addition, when the height of the stone wall exceeds 2/5H, the change in maximum tensile stresses is no longer significant (Fig. 5.18b).

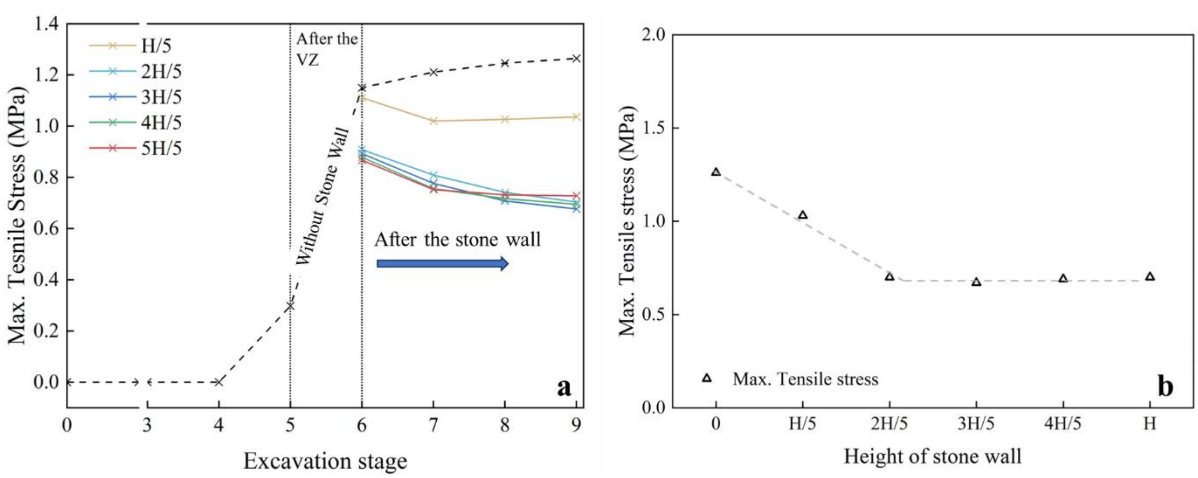

Fig.5.18: Tensile stress variations by stone wall height (a) during excavation progress, (b) at final excavation stage.

Considering the restraining mechanism of the stone wall presented in Section 4.4.1, "press effect" on the PZ discontinuity increases when the height of the stone wall exceeds VZ, resulting in decrease of shear failure zone along the discontinuity. Although it can further inhibit shear failure with an increase in the height of the stone wall, the change in effect becomes smaller because the discontinuity at the lower part is no longer sliding.

5.4.3.3 Effect of the stone wall construction timing

Fig. 5.19 shows the variations in the maximum tensile stress in triangular zone when the stone wall is constructed after the 6th and 7th excavation stages. Two different heights of the stone wall, H/5 and 2H/5 were evaluated. Both results show earlier construction is more effectively for restraining slip deformation because stone wall can significantly reduce the maximum tensile stress.

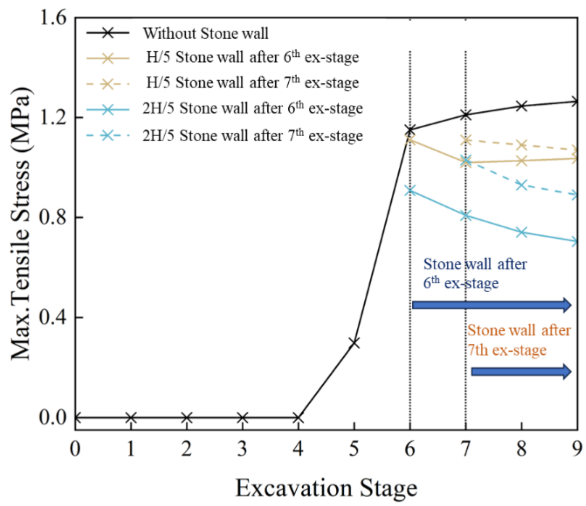

Fig.5. 19: Tensile stress variations by stone wall construction stages.

5.5 Concluding remarks

In this Chapter, we generally investigated several considerations on effects of weak rock zone and stone wall by simplifying the geometry of the rock slope and weak rock zone. The effects of dip direction of weak rock zones and connectivity, thickness of cover rock and triangular zone were examined. The effects of stone wall heights, widths and construction timing were also studied for general recommendations. Specific conclusions can be drawn, as follows:

1. For a rock slope having a single weak rock zone, the excavation causes no slip movements. This is independent of the dip direction of a weak rock zone.

2. The deformation behavior depends on the connectivity of the weak rock zones if two weak rock zones are distributed in the rock slope. No sliding can be seen if an inclined weak rock zone is not in connection with a vertical weak rock zone. In contrast, slip movement along the inclined weak rock zone can be observed when both weak rock zones are connected.

3. Above slip movement in the case of weak rock zone connection is influenced by the thickness of cover rock. The magnitude of slip displacement decreases with increase of the thickness. Furthermore, critical thickness of the cover rock was found. No apparent sliding of the cover rock can be seen if cover rock thickness is greater than the critical value.

4. Stone wall width has little impact on restraining slip deformation, while both construction timing and height of stone wall affect slip deformation. Earlier and higher construction significantly enhance the slip deformation control. However, a critical value was found in stone wall height. No sliding can be seen at the critical height or more.

6. Conclusions and recommendations

6.1 Conclusions

This research investigated the long-term rock slope deformation observed at Mt. Buko through field measurements and numerical analysis. First, the relationship between geological conditions, excavation progress, and deformation characteristics was clarified by analyzing the measurement data and mining history. The main cause of the observed deformation was identified as the distribution pattern of weak rock zones and ongoing mining activities.

To explore this further, 2D numerical models of Mt. Buko were developed to assess the effects of weak rock zones and interpret the causes of long-term deformation.

Afterward, the study evaluated the effectiveness and optimal dimensions of the stone wall countermeasure at Mt. Buko, discussing the influence of stone wall parameters including its height and width. The mechanism of stone wall for restraining in slip deformation was also clarified.

The study further demonstrated considerations on several effects of weak rock zone and stone wall by simplifying the geometry of the rock slope and weak rock zones. The effects of dip direction of weak rock zones and their connectivity were examined followed by examination of effects of the thickness of cover rock. The research also explored the impacts of the width, height and construction timing of the stone wall for a general recommendation of stone wall design. The key findings and contributions in each chapter are summarized as follows:

Chapter 1 reviewed the background, and the objectives of research were described. Previous studies related to the effects of excavation and geological structures on rock slope deformation, causes and analysis of mining-induced deformation of rock slope, and countermeasures for restraining rock slope deformation. Previous research on analysis of rock slope deformation of Mt. Buko were also reviewed for clarifying the meaning of this study.

Chapter 2 aimed at revealing the overall characteristics of Mt. Buko. The mining history, long-term deformation, and geological conditions were explained. Two major weak rock zones were identified, with notable differences in connectivity between the west and east sides at the quarry. A weak rock zone parallel to the slope surface (PZ) connects with a vertical weak rock zone (VZ) at greater depths in the west side. In contrast, the east side shows less development of PZ, with no evidence of connection to VZ. Displacement behavior also differed between east and westsides: as excavation passed the vertical weak rock zone, little variation in displacement was observed in the east side, while significant displacement was seen in the west side. It increased rapidly when the excavation reached VZ, but gradually stabilized as excavation area became far away from VZ. These observations suggest that slope deformation is affected by the combined effects of excavation activities and the distribution of weak rock zones.

Chapter 3 aimed at identifying the main cause of the long-term deformation observed at Mt. Buko for assessment of rock slope stability. 2D numerical models for east and west sides were developed for estimation of mining-induced deformation of the rock slope. Elements for PZ and VZ were incorporated to the model and the boundaries between weak rock zones and the rock mass were modeled as discontinuities. Most notably, the analysis of stress change in the foot of the rock slope led to the proposal of a slip deformation mechanism. This mechanism suggests that excavation-induced reduction in normal stress leads to progressive failure along the discontinuities on the PZ in the west section. As the excavation level passes the VZ level, resistance to slip deformation of the cover rock decreases. Therefore, the VZ is compressed followed by bending of the foot part of the rock slope. Slip deformation finally stabilizes as the excavation progresses, when the driving force and the resisting force is in equilibrium state. The long-term deformation observed at Mt. Buko aligns well with this proposed slip mechanism. Quantitative discrepancies between simulation and field observations are partially attributed to parameter selection including Young's modulus of VZ and limestone. The rock slope at Mt. Buko is considered stable as long as the rock mass in the triangular zone stays in elastic.

Chapter 4 focused on evaluating the effectiveness of the stone walls at Mt. Buko by numerical simulation, highlighting its role in restraining slip deformation. The simulation results show that the current stone wall, constructed to a height of 1,000 m (below the VZ level), significantly restrains slip deformation. Increasing the height to 1,050 m (above the VZ level) further enhances this restraining effect. The weight of the stone wall is effective to restrain the slip deformation. The stone wall not only increased the bending stiffness of triangular zone but also provides a "press effect," which stops shear failure along the PZ discontinuities by increasing normal stress. Although increasing the stone wall height extends the range of this press effect, further increases beyond 1,050 m have no additional impact, as immovable zones are sufficiently formed along the discontinuity.

Chapter 5 further investigated several effects of weak rock zones, cover rock, and stone wall on rock slope deformation by simplifying the geometry of rock slope and weak rock zones. No slip deformation was found in models with single weak rock zone regardless of its dip direction. The cover rock can slip along the PZ only when two weak rock zones are connected. The slip displacement decreases with thickness of cover rock until reaches the critical value. The width of stone walls has little impact on restraining slip deformation, while earlier construction of stone walls significantly enhances deformation control. The presence of a critical height of the stone wall was found. Effects of stone wall is not changed if height of stone wall is increased over the critical height.

6.2 Recommendations

Given the unexplained results and significant limitations of the current models, we propose the following recommendations for future studies:

1. Investigating the theoretical basis for the optimal values for cover rock thickness and stone wall dimensions is necessary. It would also be valuable to explore how these critical values change with factors such as rock slope angles.

2. The weak rock zone and discontinuity models should be further developed, as the current simulations are simple and fail to fully reflect observations in the PZ discontinuities at Mt. Buko. Incorporating the weakening effects of water on discontinuities and creep behavior could better represent real deformation processes in weak rock zones.

3. Evaluating the effects of pore water pressure and three-dimensional factors, which were not considered in this study, is crucial Consideration of these factors would be worth exploring whether the triangular zone remains the weakest area of the rock slope.

References

Abdellah, W. R., Hirohama, C., Sainoki, A., Towfeek, A. R., & Ali, M. A. M. (2022). Estimating the Optimal Overall Slope Angle of Open-Pit Mines with Probabilistic Analysis. Applied Sciences, 12(9), 4746.

Ahmad, N. A., Mohammad Zaki, M., & Ayob, A. (2016). Slope remediation method using rock buttress in Malaysia: a review. International Journal of Applied Engineering Research, 11(16), 8920-8923.

Akin, M. (2013). Slope Stability Problems and Back Analysis in Heavily Jointed Rock Mass: A Case Study from Manisa, Turkey. Rock Mechanics and Rock Engineering, 46(2), 359-371.

Altuntov, F. K., & Erkayaoğlu, M. (2021). A New Approach to Optimize Ultimate Geometry of Open Pit Mines with Variable Overall Slope Angles. Natural Resources Research, 30(6), 4047-4062.

Amagu, C. A., Zhang, C., Kodama, J.-i., Shioya, K., Yamaguchi, T., Sainoki, A., . . . Sharifzadeh, M. (2021). Displacement Measurements and Numerical Analysis of Long-Term Rock Slope Deformation at Higashi-Shikagoe Limestone Quarry, Japan. Advances in Civil Engineering, 2021, 1316402.

Amagu, C. A., Zhang, C., Sainoki, A., Sugimoto, K., Shimada, H., Dzimunya, N., . . . Kodama, J.-i. (2024). Analysis of Excavation-Induced Effect of a Rock Slope Using 2-Dimensional Back Analysis Method: A Case Study for Clay-Bearing Interbedded Rock Slope. Geotechnical and Geological Engineering, 42(7), 6315-6337.

Amini, M., & Ardestani, A. (2019). Stability analysis of the north-eastern slope of Daralou copper open pit mine against a secondary toppling failure. Engineering Geology, 249, 89-101.

An, B., Wang, C., Liu, C., & Li, P. (2023). A multi-source remote sensing satellite view of the February 22nd Xinjing landslide in the mining area of Alxa left Banner, China. Landslides.

Aoyama, H., Yano, K., Kondo, M., Ozawa, N., & Nakatani, T. (2018). Monitoring of a Rock Slope Using Crack Displacement Measurements in an Observation Drift at the Une Mine. Journal of MMIJ, 134(11), 179-187.

Assefa, S., Graziani, A., & Lembo-Fazio, A. (2017). A slope movement in a complex rock formation: Deformation measurements and DEM modelling. Engineering Geology, 219, 74-91.

Ataei M, Bodaghabadi S (2008) Comprehensive analysis of slope stability and determination of stable slopes in the Chador-Malu iron ore mine using numerical and limit equilibrium methods, J China University Mining and Technology. 18:488-493

Ayalew L, Yamagishi H, Ugawa N (2004) Landslide susceptibility mapping using GIS-based weighted linear combination, the case in Tsugawa area of Agano River, Niigata Prefecture, Japan. Landslides 1:73-81.

Azarfar, B., Ahmadvand, S., Sattarvand, J., & Abbasi, B. (2019). Stability Analysis of Rock Structure in Large Slopes and Open-Pit Mine: Numerical and Experimental Fault Modeling. Rock Mechanics and Rock Engineering, 52(12), 4889-4905.

Ballou, J. (2002). Soil and rock slope stabilization using fiber-reinforced shotcrete in Northern California. Shotcrete Magazine, Summer 2002, 12-17.

Ballou, J. (2003). Steep slope stabilization with fiber-reinforced shotcrete. Shotcrete Magazine, Fall 2003, 18-22.

Bandis, S. C., Lumsden, A. C., & Barton, N. R. (1983). Fundamentals of rock joint deformation. International Journal of Rock Mechanics and Mining Sciences & Geomechanics Abstracts, 20(6), 249-268.

Barla G (2016) Application of numerical methods in tunnelling and underground excavations: Recent trends. Rock Mechnics and Rock Engineering: from the past to the future-Ulusay et al. (Eds), Taylor and Francis Group, London, ISBN 978-1-138-03265-1.

Basahel, H., & Mitri, H. S. (2017). Application of rock mass classification systems to rock slope stability assessment: A case study. Journal of Rock Mechanics and Geotechnical Engineering, 9, 993-1009.

Bishop AW (1955) The use of the slip circle in stability analysis of slopes, Geotechnique, 5(1):7-17.

Bommer JJ, Rodrı’guez CE (2002) Earthquake-induced landslides in Central America, Eng. Geol. 63:189-220.

Cai F, Ugai K (2004) Numerical analysis of rainfall effects on slope stability, Int. J. Geomech. 4(2): 69-78.

Cambio, D., Hicks, D. D., Moffitt, K., Yetisir, M., & Carvalho, J. L. (2019). Back-Analysis of the Bingham Canyon South Wall: A Quasi-static Complex Slope Movement Mechanism. Rock Mechanics and Rock Engineering, 52(12), 4953-4977.

Carvalho, J. (2004). Estimation of rock mass modulus. Personal communication.

Chen, Y. (2014). Experimental study and stress analysis of rock bolt anchorage performance. Journal of Rock Mechanics and Geotechnical Engineering, 6(5), 428-437.

Chia-Cheng Fan, Yung-Show Fang, Numerical solution of active earth pressures on rigid retaining walls built near rock faces, Computers and Geotechnics,Volume 37, Issues 7–8,2010,Pages 1023-1029.

Cominelli, S., Giuriani, E., & Marini, A. (2016). Mechanisms governing the compressive strength of unconfined and confined rubble stone masonry. Materials and Structures, 50(1), 10.

Contreras, L., Hormazabal, E., Ledezma, R., & Arellano, M. (2019). Geotechnical risk analysis for the closure alternatives of the Chuquicamata open pit. Mining Geotechnical Risk, 373-388.

Cundall, P. A. and Strack, O. D. L. (1979), A discrete numerical model for granular assemblies, Geotechnique 29:47-65

Dahal RK, Hasegawa S, Masuda T, Yamanaka M (2006) Roadside Slope Failures in Nepal during Torrential Rainfall and their Mitigation, Disaster Mitigation of Debris Flows, Slope Failures and Landslides 503–514.

Day, J. J., Diederichs, M. S., & Hutchinson, D. J. (2017). New direct shear testing protocols and analyses for fractures and healed intrablock rockmass discontinuities. Engineering Geology, 229, 53-72.

Dou, H.-q., Huang, S.-y., Wang, H., & Jian, W.-b. (2022). Repeated failure of a high cutting slope induced by excavation and rainfall: a case study in Fujian, Southeast China. Bulletin of Engineering Geology and the Environment, 81(6), 227.

Duncan, J. M. Soil Slope Stability Analysis" in Landslides: Investigiation and Mitigation, Ed. A. K. Turner and R. L. Schuster. Transportation Research Board. Washington, DC 247:337-371

Eang, K. E., Igarashi, T., Kondo, M., Nakatani, T., Tabelin, C. B., & Fujinaga, R. (2018). Groundwater monitoring of an open-pit limestone quarry: Water-rock interaction and mixing estimation within the rock layers by geochemical and statistical analyses. International Journal of Mining Science and Technology, 28(6), 849-857.

Eberhardt E (2003) Rock Slope Stability Analysis—Utilization of Advanced Numerical Techniques; Earth and Ocean Sciences at UBC Report; University of British Columbia (UBC): Vancouver, BC, Canada, 2003.

Eberhardt E, Stead D, Coggan JS (2004) Numerical analysis of initiation and progressive failure in natural rock slopes-the 1991 Randa rockslide, Int J Rock Mech Min Sci 41: 69-87.

El Kateb, H., Zhang, H., Zhang, P., & Mosandl, R. (2013). Soil erosion and surface runoff on different vegetation covers and slope gradients: A field experiment in Southern Shaanxi Province, China. Catena, 105, 1-10.

El-Hassanin, A., Labib, T., & Gaber, E. (1993). Effect of vegetation cover and land slope on runoff and soil losses from the watersheds of Burundi. Agriculture, ecosystems & environment, 43(3-4), 301-308.

Erguler, Z. A., & Ulusay, R. (2009). Water-induced variations in mechanical properties of clay-bearing rocks. International Journal of Rock Mechanics and Mining Sciences, 46(2), 355-370.

Flores-Gonzalez, G., & Catalan, A. (2018). A transition from a large open pit into a novel “macroblock variant” block caving geometry at Chuquicamata mine, Codelco Chile. Journal of Rock Mechanics and Geotechnical Engineering, 11.

Gang, M., Nonaka, S., Utashiro, K., Kodama, J.-i., Nakamura, D., Fujii, Y., . . . Wang, S. (2024). Impacts of frost heave susceptibility and temperature-changing conditions on freeze-thaw deterioration of welded tuffs. Cold Regions Science and Technology, 225, 104270.

Gao W, Dai S, Xiao T, He T (2017) Failure process of rock slopes with cracks based on the fracture mechanics. Eng. Geol., 231, 190–199.

Gao, X. (2024). Development laws of geological hazards along urban highway in Southwest China and countermeasures for prevention and control. Geohazard Mechanics, 2(1), 13-20.

Glastonbury, J., & Fell, R. (2000). Report on the analysis of" rapid" natural rock slope failures: University of New South Wales, School of Civil and Environmental Engineering.

Griffiths DV, Lane PA (1999) Slope stability analysis by finite elements, Geotechnique 49(3): 387-403.

Gu, R., & Ozbay, U. (2014). Distinct element analysis of unstable shear failure of rock discontinuities in underground mining conditions. International Journal of Rock Mechanics and Mining Sciences, 68, 44-54.

Gu. (2009). Guidelines for Open Pit Slope Design.

He MC, Feng JL, Sun XM (2008) Stability evaluation and optimal excavated design of rock slope at Antaibao open pit coal mine, China, Int J Rock Mech Min Sci 45:289-302.

Hendry, A. W. (1998). Structural masonry: Bloomsbury Publishing.

Hicks, M. A., & Li, Y. (2018). Influence of length effect on embankment slope reliability in 3D. International Journal for Numerical and Analytical Methods in Geomechanics, 42(7), 891-915.

Hocking, G. (1976). A method for distinguishing between single and double plane sliding of tetrahedral wedges. International Journal of Rock Mechanics and Mining Science, 13(Analytic).

Hoek, E. and Bray, J. W. (1981), Rock Slope Engineering. 3rd ed. London: The Institution of Mining and Metallurgy, Maney Publishing

Hoek, E., & Diederichs, M. S. (2006). Empirical estimation of rock mass modulus. International Journal of Rock Mechanics and Mining Sciences, 43(2), 203-215.

Hustrulid WA, McCarter MK, Van Zyl DJA (2000) Slope Stability in Surface Mining; Society for Mining, Metallurgy, and Exploration: Littleton, CO, USA, pp. 81-88.

Ingold, T. S. (2013). Geotextiles and geomembranes handbook: Elsevier.

Ishikawa T, Tokoro T, Seiichi M (2015) Geohazard at volcanic soil slope in cold regions and its influencing factors, Jpn Geotech Soc Spec 1:1-20.

Itasca. UDEC, Version 7.0; Theory and Background; Itasca Consulting Group Inc.: Minneapolis, MN, USA, 2021.

Jiang, Y., Yamashita, Y., Sawada, M., Li, B., & Etou, Y. (2008). Evaluation of Progressive Failure Mechanism in Jointed Rock Slopes by applying Extended Distinct Element Method. Journal of MMIJ, 124, 771-776.

Jing L (2003) A review of techniques, advances and outstanding issues in numerical modeling for rock mechanics and rock engineering, International Journal of Rock Mechanics and Mining Sciences, 40:283-353.

Jing L, Hudson JA (2002) Numerical methods in rock mechanics, International Journal of Rock Mechanics and Mining Sciences, vol. 39, pp. 409–27.

Kaczmarek, Ł. D., & Popielski, P. (2019). Selected components of geological structures and numerical modelling of slope stability. Open Geosciences, 11(1), 208-218.

Kainthola, A., Verma, D., Gupte, S.S. and Singh, T. N. (2011), A Coal Mine Dump Stability Analysis —A Case Study, Int.Jour. Geomaterial 1:2011

Kaneko, K., Noguchi, Y., Soda, K., & Hazuku, M. (1996). Stability Assesment of Rock Slope by Displacement Measurement. Journal of MMIJ, 112, 915-920.

Kang, J., Wan, D., Sheng, Q., Fu, X., Pang, X., Xia, L., & Li, D. (2022). Risk assessment and support design optimization of a high slope in an open pit mine using the jointed finite element method and discontinuous deformation analysis. Bulletin of Engineering Geology and the Environment, 81(6), 254.

Keefer DV (2000) Statistical analysis of an earthquake-induced landslide distribution-the 1989 Loma Prieta, California event, Eng. Geol 58:231-249.

Kodama, J., Miyamoto, T., Kawasaki, S., Fujii, Y., Kaneko, K., & Hagan, P. (2013). Estimation of regional stress state and Young's modulus by back analysis of mining-induced deformation. International Journal of Rock Mechanics and Mining Sciences, 63, 1-11.

Kodama, J., Nishiyama, E., & Kaneko, K. (2009). Measurement and interpretation of long-term deformation of a rock slope at the Ikura limestone quarry, Japan. International Journal of Rock Mechanics and Mining Sciences, 46(1), 148-158.

Kodama, J.-i., Mitsui, Y., Hara, S., Fukuda, D., Fujii, Y., Sainoki, A., & Karakus, M. (2019). Time-dependence of mechanical behavior of Shikotsu welded tuff at sub-zero temperatures. Cold Regions Science and Technology, 168, 102868.

Koerner, R., Hsuan, Y., & Koerner, G. (2017). Lifetime predictions of exposed geotextiles and geomembranes. Geosynthetics International, 24(2), 198-212.

Kolapo P, Oniyide GO, Said KO, Lawal AI, Onifade M, Munemo P (2022) An Overview of Slope Failure in Mining Operations. Mining, 2, 350–384.

Kondo, M., Aoyama, H., Ozawa, N., & Yano, K. (2018). Countermeasures Against Rainfalls: Towards Stabilizing the Slope at the Une Mine. Journal of MMIJ, 134(11), 198-207.

Kondo, M., Ozawa, N., Aoyama, H., & Yano, K. (2018). Relationship between the Groundwater Fluctuation and Deformation Behavior of Rock Slope at Mt. Buko. Journal of MMIJ, 134(11), 188-197.

Kulhawy, F. H., & Mayne, P. W. (1990). Manual on estimating soil properties for foundation design.

Kuraoka, S., Monma, K., & Shuzui, H. (2000). Numerical Analysis of Jointed Rock Slope in Practice. Journal of the Japan Society of Engineering Geology, 41(1), 24-33.

Lee, C.-Y., & Wang, I.-T. (2011). Analysis of highway slope failure by an application of the stereographic projection. International Journal of Geological and Environmental Engineering, 5(3), 122-129.

Lee, D.-H., Yang, Y.-E., & Lin, H.-M. (2007). Assessing slope protection methods for weak rock slopes in Southwestern Taiwan. Engineering Geology, 91(2-4), 100-116.

Lemaire, E., Mreyen, A.-S., Dufresne, A., & Havenith, H.-B. (2020). Analysis of the Influence of Structural Geology on the Massive Seismic Slope Failure Potential Supported by Numerical Modelling. Geosciences, 10(8), 323.

Li, Y., Yu, L., Song, W., & Yang, T. (2019). Three-Dimensional Analysis of Complex Rock Slope Stability Affected by Fault and Weak Layer Based on FESRM. Advances in Civil Engineering, 2019, 6380815.

Liu, N., Yang, Y., Li, N., Liang, S., Liu, H., & Li, C. (2024). The stability issue of fractured rock mass slope under the influences of freeze–thaw cycle. Scientific Reports, 14(1), 5674.

Liu, Y., Wang, X., & Gao, J. (2019). Stability Analysis and Reinforcement Treatment of Open Pit Slope. IOP Conference Series: Earth and Environmental Science, 283(1), 012009.

Lu L, Wang ZJ, Huang XY, Zheng B, Arai K (2014) Dynamic and static combination analysis method of slope stability analysis during earthquake. Math Probl Eng 2014a;

Lu L, Wang ZJ, Song ML, Arai K (2015) Stability analysis of slopes with ground water during earthquakes, Eng Geol 193:288-296.

López-Vinielles, J., Ezquerro, P., Fernández-Merodo, J. A., Béjar-Pizarro, M., Monserrat, O., Barra, A., . . . Herrera, G. (2020). Remote analysis of an open-pit slope failure: Las Cruces case study, Spain. Landslides, 17(9), 2173-2188.

Ma, H.-S., & Lee, S.-J. (2018). Analysis of Slope Stability of Masonry Retaining Walls in Quarry. Journal of Korean Society of Forest Science, 107(4), 385–392.

Ma, N., Ma, H., & Feng, W. (2015). Interaction between countermeasure works and landsliding mass: a case study. Paper presented at the The 10th Asian Regional Conference of IAEG.

MacLaughlin, M., Sitar, N., Doolin, D., & Abbot, T. (2001). Investigation of slope-stability kinematics using discontinuous deformation analysis. International Journal of Rock Mechanics and Mining Sciences, 38(5), 753-762.

Majdi, A., Bashari, A., & Beiki, M. (2011). Estimation of Rock Mass Deformation Modulus Based on GSI System. 12th ISRM Congress.

Malmgren, L., & Nordlund, E. (2008). Interaction of shotcrete with rock and rock bolts—a numerical study. International Journal of Rock Mechanics and Mining Sciences, 45(4), 538-553.

Marinos, P., & Hoek, E. (2000). Gsi: A Geologically Friendly Tool For Rock Mass Strength Estimation ISRM International Symposium.

Matsuda H, Shimizu N, Yoshitomi I, Kawahata K, Chiba T, Tonsyo M (2003) Accuracy of displacement monitoring of Large slope by using GPS. MMIJ 119:389-395.

Milani, G., Lourenço, P. B., & Tralli, A. (2006). Homogenised limit analysis of masonry walls, Part I: Failure surfaces. Computers & Structures, 84(3), 166-180.

Mohammad, A., Haluk, A., Akbar, G., Ebrahim, A., Jafar, R. and Reza, D. (2021), Discontinuous rock slope stability analysis by limit equilibrium approaches – a review 12:1918-1941

Moriya, R., Fukuda, D., Kodama, J.-i., & Fujii, Y. (2016). Effect of buttress on reduction of rock slope sliding along geological boundary. Paper presented at the 3rd International Symposium on Mine Safety Science and Engineering.

Najib, Fukuda, D., Kodama, J.-I., & Fujii, Y. (2015). The Deformation Modes of Rock Slopes due to Excavation in Mountain-Type Mines. MATERIALS TRANSACTIONS, 56(8), 1159-1168.

Nakamura N, Tsukayama Y, Hirata A, Kaneko K (2003) Displacement measurement of rock slope with cover rock and its interpretation. MMIJ 119: 547-552.

Nakatani, T., Fujimaki, K., Hirasawa, Y., Akiyama, F., Miyayumi, T., & Tanaka, K. (2018). Monitoring of the Surface Displacements of the Final Slope at Mt.Buko. Journal of MMIJ, 134(11), 170-178.

Nie, L., Li, Z. C., Zhang, M., & Xu, L. N. (2015). Deformation characteristics and mechanism of the landslide in West Open-Pit Mine, Fushun, China. Arabian Journal of Geosciences, 8(7), 4457-4468.

Noguchi Y, Okada Y (1999) Monitoring of rock slopes in the Ikura limestone quarry Limestone. MMIJ 297:28-35.

Obara Y, Nakamura N, Kang SS, Kaneko K (2000) Measurement of local stress and estimation of regional stress associated with stability assessment of an open-pit rock slope. Int J Rock Mech Min Sci 37:1211-1221.

Ogawa, S., Kumazawa, K., Makino, H., & Ozawa, N. (2024). Influence of Fracture Zone on Final Slope Displace-ment : Insights from Long-Term Monitoring in the Une Mine. Journal of MMIJ, 140(6), 86-93.

Ohtsuka S, Matsuo M (1995) Rigid plastic dynamic deformation analysis of structures, Proceedings of 1st International Conference on Earthquake vol. 2. Geotechnical Engineering, Tokyo, Japan, 1147-1152.

Orense RP (2012) Soil liquefaction and slope failures during the 2011 Tohoku, Japan Earthquake. 2012 NZSEE Annual Technical Conference and AGM, New Zealand, Paper ID 007: 1-8.

Ortigao, J. A. R., & Sayao, A. (2004). Handbook of Slope Stabilisation: Springer.

Ou, C.-Y., Teng, F.-C., Seed, R. B., & Wang, I.-W. (2008). Using buttress walls to reduce excavation-induced movements. Proceedings of the Institution of Civil Engineers - Geotechnical Engineering, 161(4), 209-222.

Ozawa, N. (2018). Analyzing the Impacts of Rainfall on Rock Slope Behavior in Une Mine and Evaluating the Effec-Tiveness of Countermeasure Methods. Journal of MMIJ, 134(11), 208-221.

Paul Schlotfeldt, Davide Elmo, Brad Panton, Overhanging rock slope by design: An integrated approach using rock mass strength characterisation, large-scale numerical modelling and limit equilibrium methods, Journal of Rock Mechanics and Geotechnical Engineering, Volume 10, Issue 1,2018, Pages 72-90, ISSN 1674-7755

Peacock, D. C. P., & Xing, Z. (1994). Field examples and numerical modelling of oversteps and bends along normal faults in cross-section. Tectonophysics, 234(1), 147-167.

Ponte, M., Penna, A., & Bento, R. (2023). In-plane cyclic tests of strengthened rubble stone masonry. Materials and Structures, 56(2), 41.

Rajendra Kumar, P., Muthukkumaran, K., & Sharma, C. (2024). Reviewing Slope Stability Integration in Disaster Management and Land Use Planning. In C. Sharma, A. K. Shukla, S. Pathak, & V. P. Singh (Eds.), Sustainable Development and Geospatial Technology: Volume 2: Applications and Future Directions (pp. 139-151). Cham: Springer Nature Switzerland.

Read JR, Stacey PF (2009) Guidelines for Open Pit Slope Design, CSIRO Publishing, Collingwood, Australia.

Rose, N. D., & Hungr, O. (2007). Forecasting potential rock slope failure in open pit mines using the inverse-velocity method. International Journal of Rock Mechanics and Mining Sciences, 44(2), 308-320.

Sarma, S. K. (1979). Stability analysis of embankments and slopes. Journal of the Geotechnical Engineering Division, 105(12), 1511-1524.

Sharifzadeh M, Fahimifar A, Esaki T (2002) Classification and modelling of water effect on mechanical behaviour of intact rock and rock joint. In: Proceedings of the Fourth International Summer Symposium, Kyoto, Japan, pp 263-266.

Sharifzadeh M, Javadi M (2017) Groundwater and underground excavations: From theory to practice. In Rock Mechanics and Engineering: Analysis, Modeling and Design 3: 300-329.

Shimizu N, Koyama S, Ono H, Miyashita K, Kondo H, Mizuta Y (1997) Field experiments and data processing for continuous measurement by GPS displacement monitoring system. MMIJ113: 549-54.

Sonmez, H., Gokceoglu, C., & Ulusay, R. (2004). Indirect determination of the modulus of deformation of rock masses based on the GSI system. International Journal of Rock Mechanics and Mining Sciences, 41(5), 849-857.

Stead D, Eberhardt E, Coggan JS (2006) Developments in the characterization of complex rock slope deformation and failure using numerical modeling techniques, Eng Geol 83: 217-235.

Stead, D., & Wolter, A. (2015). A critical review of rock slope failure mechanisms: The importance of structural geology. Journal of Structural Geology, 74, 1-23.

Sugawara K (2000) Next-generation measuring technology for risk management of rock slopes in open-pit limestone quarries. MMIJ 307:43-62.

Sugiyama T, Okata K, Muraishi H, Noguchi T, Samizo M (1995) Statistical rainfall risk estimating method for a deep collapse of a cut slope. Soils Found 35(4):37- 48.

Sundaravel, V., Deviprasad, B. S. G., Saseendran, R., & Dodagoudar, G. R. (2023). Stability and Serviceability Assessment of Reinforced Earth Retaining Structures: A State-of-the-Art and Way Forward. International Journal of Geosynthetics and Ground Engineering, 9(3), 30.

Tang, H., Yong, R., & Ez Eldin, M. (2017). Stability analysis of stratified rock slopes with spatially variable strength parameters: the case of Qianjiangping landslide. Bulletin of Engineering Geology and the Environment, 76, 839-853.

Ukritchon, B., Chea, S., & Keawsawasvong, S. (2017). Optimal design of Reinforced Concrete Cantilever Retaining Walls considering the requirement of slope stability. KSCE Journal of Civil Engineering, 21(7), 2673-2682.

Ulusay, R., Yoleri, M., & Doyuran, V. (1993). Application of a rock buttress in the design of slopes of a strip coal mine adjacent to a highway. Canadian Geotechnical Journal, 30(3), 391-408.

Van Santvoort, G. P. (1994). Geotextiles and geomembranes in civil engineering: CRC Press.

Vick, L. M., Böhme, M., Rouyet, L., Bergh, S. G., Corner, G. D., & Lauknes, T. R. (2020). Structurally controlled rock slope deformation in northern Norway. Landslides, 17(8), 1745-1776.

Wang, L.-y., Chen, W.-z., Tan, X.-y., Tan, X.-j., Yuan, J.-q., & Liu, Q. (2019). Evaluation of mountain slope stability considering the impact of geological interfaces using discrete fractures model. Journal of Mountain Science, 16(9), 2184-2202.

Wang, Y., Smith, J. V., & Nazem, M. (2021). Optimisation of a Slope-Stabilisation System Combining Gabion-Faced Geogrid-Reinforced Retaining Wall with Embedded Piles. KSCE Journal of Civil Engineering, 25(12), 4535-4551.

Weigang, S., Tao, Z., Feng, D., Mingjing, J., and Gordon, G. D. Z. (2019), DEM analyses of rock block shape effect on the response of rockfall impact against a soil buffering layer, Engineering Geology 249:60-70

Widijanto, E., Wattimena, R. K., Kramadibrata, S., & Rai, M. A. (2017). Geometry effects on Slope Stability at Grasberg Mine Through the Transsition from Open Pit to Underground Block Cave Mining. Electron. J. Geotech. Eng, 22, 1733-1745.

Xie, J., Yang, G. L., Qin, Y. G., & Xu, X. T. (2020). Deformation Failure Mechanism and Motion Laws of Near-horizontal Thick-layer with Thin-layer Columnar Dangerous Rock Mass in the Chishui Red Bed Area. IOP Conference Series: Earth and Environmental Science, 570(2), 022045.

Yamaguchi U, Shimotani T (1986) A Case Study of Slope Failure in a Limestone Quarry. Int J Rock Mech Min Sci Geomech Abstracts 23: 95-104.

Yamaguchi, U. (2018). Cooperative Mining of Limestone at Mt. Buko and the Task Group for Research on Rock Slope in Chichibu Area (Chichibu Zanken). Journal of MMIJ, 134(6), 67-73.

Yamaguchi, U. (2018). Rock Slope Monitoring, over 20 years long. Journal of MMIJ, 134(11), 159-160.

Yamatomi, J., Sugiyama, T., Mikami, K., Wakisaka, T., & Yamaguchi, U. (2018). Limestone Mining and Slope Management at Mt. Buko. Journal of MMIJ, 134, 161-169.

Yang, X., Jiang, A., & Zheng, S. (2021). Analysis of the effect of freeze-thaw cycles and creep characteristics on slope stability. Arabian Journal of Geosciences, 14(11), 1033.

Yeh HF, Wang JG, Shen KL, Lee CH (2015) Rainfall characteristics for anisotropic conductivity of unsaturated soil slopes, Environmental Earth Sciences, 73: 8669–8681.

Yoon, W., Jeong, U., & Kim, J. (2002). Kinematic analysis for sliding failure of multi-faced rock slopes. Engineering Geology, 67(1-2), 51-61.

Yuannian, W. and Fulvio, T. (2011), Discrete Element Modeling of Rock Fragmentation upon Imapct in Rock Fall Analysis, Rock Mechanics and Rock Engineering 44:23-35

Zhang, C., Amagu, C. A., Kodama, J., Sainoki, A., Ogawa, S., Umeda, C., . . . Fukuda, D. (2021). Numerical analysis of impact of fault and weak rock formation on mining-induced deformation of rock slope. IOP Conference Series: Earth and Environmental Science, 861(3), 032087.

Zhang, C., Clement, A. A., Kodama, J.-i., Sainoki, A., Fujii, Y., Fukuda, D., & Wang, S. (2024). Effect of the Connectivity of Weak Rock Zones on the Mining-Induced Deformation of Rock Slopes in an Open-Pit Mine. Sustainability, 16(14).

Zhang, K. (2020). Failure Mechanism and Stability Analysis of Rock Slope, New Insight and Methods.

Zhang, Q. B., & Zhao, J. (2014). A Review of Dynamic Experimental Techniques and Mechanical Behaviour of Rock Materials. Rock Mechanics and Rock Engineering, 47(4), 1411-1478.

Zhang, X., Tang, X., Li, T., Ji, Y., & Zhang, X. (2024, 7-12 July 2024). Multi-Temporal Monitoring and Analysis for Alxa Left Banner Open-Pit Mining Area Collapse Based on Lutan-1 SAR Satellites. Paper presented at the IGARSS 2024 - 2024 IEEE International Geoscience and Remote Sensing Symposium.

Zhao, Z., Guo, T., Ning, Z., Dou, Z., Dai, F., & Yang, Q. (2018). Numerical Modeling of Stability of Fractured Reservoir Bank Slopes Subjected to Water–Rock Interactions. Rock Mechanics and Rock Engineering, 51(8), 2517-2531.

Zheng, Y., Chen, C., Liu, T., Song, D., & Meng, F. (2019). Stability analysis of anti-dip bedding rock slopes locally reinforced by rock bolts. Engineering Geology, 251, 228-240.

Zhou, K., Xu, H., Yang, C., Xiong, X., & Gao, F. (2023). Numerical Simulation of Underground Mining-Induced Fault-Influenced Rock Movement and Its Application. Sustainability, 15(6), 5197.

Zhu, J. B., Deng, X. F., Zhao, X. B., & Zhao, J. (2013). A Numerical Study on Wave Transmission Across Multiple Intersecting Joint Sets in Rock Masses with UDEC. Rock Mechanics and Rock Engineering, 46(6), 1429-1442.

Zhu, L., He, S., Jian, J., Zhou, J., & Liu, B. (2021). Geological structure and failure mechanism of an excavation-induced rockslide on the Tibetan Plateau, China. Bulletin of Engineering Geology and the Environment, 80(2), 1019-1033.

de Buhan, P., & de Felice, G. (1997). A homogenization approach to the ultimate strength of brick masonry. Journal of the Mechanics and Physics of Solids, 45(7), 1085-1104.

onmez, H., Gokceoglu, C., & Ulusay, R. (2004). Indirect determination of the modulus of deformation of rock masses based on the GSI system. International Journal of Rock Mechanics and Mining Sciences, 41(5), 849-857.